THE UNIVERSITY OF CHICAGO

MANIPULATING ELECTROMAGNETIC FIELDS IN COLLOIDAL METAL NANOPARTICLE SYSTEMS

A DISSERTATION SUMBITTED TO
THE FACULTY OF THE DIVISION OF THE PHYSICAL SCIENCES
IN CANDIDACY FOR THE DEGREE OF
DOCTOR OF PHILOSOPHY

DEPARTMENT OF CHEMISTRY

BY

NOLAN MILLER SHEPHERD

CHICAGO, ILLINOIS

MARCH 2019

TABLE OF CONTENTS

LIST OF FIGURES

LIST OF TABLES

ACKNOWLEDGMENTS

To say that I undertook the writing of this dissertation and by extension the whole of my doctoral degree simply by my own efforts would be a gross misrepresentation of reality. I am more than convinced if that were the case, I would have never even made it past the first year, let alone through the six that it took to reach this point. I owe my success here to a multitude of people - mentors, coworkers, friends, and family.

First of all, none of this work was possible without Prof. Norbert Scherer, my Ph.D. adviser and mentor in research. Through the innumerable discussions on anything from the minute details of how to design and run experiments to crafting the overall story of a project, Norbert offered his expertise in physical chemistry to forward my education, and it proved invaluable in advancing my projects. His creativity in how to approach scientific problems is incredible and I appreciate all the effort he puts in to leading his research group.

My undergraduate research adviser, Prof. Warren Beck, deserves mention here as well, giving me my first taste in how physical chemistry research is done. Any alignment of optical systems in my dissertation work started with building laser systems in his lab, and any new analysis workflow I had to design began with the projects he handed me to complete. He also encouraged me to apply to graduate school at the University of Chicago and work under Dr. Scherer to continue my education, so I attribute at least some of the direction of my career to his advice.

The members of my first-year teaching assistant office in Kent helped me keep my sanity throughout the years our cohort was at the university even after we split up into our respective research groups. Thanks to all of you for sharing in the frustrations of the coursework and dealing with out first quarters of teaching, and for all the nights on the North Side when we needed to get out of Hyde Park. Valentine, thank you for proving it's a small world and sharing in all things Michigan State, and for keeping us distracted when we needed

the break from thinking about grad school. Erica, I appreciated how often you opened up your apartment for hanging out and the delicious baked goods. Jeremy, your Superbowl parties and homebrews were top notch. Jacob, thanks for trading all those Tom Collins for having Ed Fitz no matter where you showed up. Paul, you were a great roommate and fellow experimentalist, reminding me that it was possible to graduate without going computational. And also, thanks for keeping us healthy with the tradition of the post-run porter.

I also owe reaching this point in my academic career to all of my fellow graduate students and the postdoctoral fellows in the Scherer research group over the years. Many of the life lessons I'd learned over this period of my life I can trace back to Raman, who was willing to share the wisdom he'd gained through the difficulties in earning his degree. That fine balance between giving your time and energy to your research projects and the undergraduates you're teaching, and retaining enough sanity to go on another day was hard-fought knowledge, and Raman was constant reminder that it was possible. Pat, also going through the program ahead of me, was an inspiration in managing to graduate despite numerous failed and slow experiments. Commiserating over those frustrations and and juggling teaching assignments on top of it all brought a sense of camaraderie to the lab. Zijie's impressive work ethic and ability to crank out publications were an inspiration to us all, and my optical trapping expertise is due in large part to him. The 'real' chemistry in this dissertation came mostly from working with Ying in the wet lab, and her sense of humor kept us from getting too depressive in the subbasement. My thanks goes to Uttam for spearheading a number of the projects that developed into the research presented in this dissertation. I was glad for Yuval's willingness to assist with lab work and discussing data analysis - his patience with the stressed-out grad student was much appreciated. Delphine too, she offered help when I needed it but was too stubborn or tired to ask. Itay may have argued every point of every presentation he heard, but he ensured we had sound and robust logic in the conclusions of our projects. Sharing a single setup for multiple experiments that were under development

must've been a trying experience, but Tiansong was never cross about doing so, and was even willing to include me in his manuscripts. The simulations I present in my work would not have been possible without all of the discussions I had with Nishant nor the coding help I had from John. Xiaolei's work on imaging techniques was instrumental in developing the the experimental methods of my projects. Curtis was a great help with discussing statistical analysis, determining error bars, and begrudgingly, cross-correlations. Matt's board game nights and baked goods were consistent reminders of the finer things in life. Emmanuel, I apologize if I had been short with you - you were learning how to get your projects off the ground while I was busy trying to leave the program, I could've been more understanding, given how difficult I found the beginning of my degree. Nonetheless, thank you for taking over the projects that I started and being a sounding board for finishing my experiments. Thank you Hannah for taking over updating the group's website and for making sure the group met outside of the lab to have a semblance of a social life. Finally, thanks to all of research group for sitting through the rougher talks I gave during our Friday meetings, dealing with having to work in the dark while I ran experiments, and being the kind of coworkers I'd hope to have for the rest of my career.

None of this dissertation would have been possible without the Materials Research Center (MRSEC) here at the university and the members of its staff. Justin's knowledge of all of the equipment in our lab is nothing short of incredible; I would've never been able to find anything without his assistance. Furthermore, the home-built Ti:Sapphire pulsed laser in our lab was kept running almost entirely due to his efforts - I know it wasn't your responsibility, but I appreciate the sheer number of hours you put in to maintain this integral piece of equipment. And Qiti, thank you for all the time you invested into training me on the shared equipment.

Thank you again, Prof. Engel and Prof. Guyot-Sionnest for serving on my defense committee and for all of your suggestions to ensure this dissertation was the best representation

of all of the work I had completed for my degree.

Outside the University, I have to recognize the support I received from my family despite my best efforts to hermit myself away from them in Chicago. Mom and Dad, I cannot thank you enough for everything you put into raising me and instilling in me a strong work ethic. When I needed to escape from grad school for even just a day, you were there to welcome me back home, and understood when all wanted to do while home was sitting around and doing nothing. Thank you for encouraging me when I needed it, and loving me when it was difficult. To my brothers, Chet, Alex, and Paul, thanks for keeping in touch despite being spread out across the country and picking up right where we left off when we did manage to all be in the same state. Paul and Amanda, my wife's parents, were more than gracious enough to accept me as if I belonged in their family for years longer than I knew them, and I'm grateful for their support and taking us in for many a vacation.

While it took more than all her patience to stay by my side for the duration of my degree, my wife Alex put in more than her fair share keeping me sane and working despite my best efforts to give up. From not seeing the best in me scant months into our relationship during candidacy, through committing to spend life together when only knowing me as a grad student, to pushing me to continue when I was certain I'd never graduate, you've been the companion that I've always needed. It'd be impossible for me to thank you enough for the inspiration, love, and support you've provided over these years. I love you all the way to this degree and back, and on to wherever we end up next.

ABSTRACT

Colloidal metal nanoparticles are renowned for their ability to strongly scatter and absorb light due to size- and environment-dependent plasmon modes. Active areas of research focus on using both single and collections of nanoparticles to control the shape of electromagnetic fields on the nanoscale. The excitation of plasmon modes in the nanoparticles confines the energy from incident fields to sub-wavelength scales with distributions controlled by the morphology of the particles, and multiple particles arranged in the near-field can extend the excitation into a collective mode. The excitation of plasmon modes can create enhancements of the field intensity, which have been leveraged for enhancing radiative rates of light-emitting particles and molecules and increasing molecular sensing signals. However, many of these applications rely on electric field enhancements in the near field and using static nanoparticle arrangements. We present extensions to this paradigm, first by exploring the excitation of collective plasmon modes in optically-patterned linear nanoparticle arrays with separations on the order of the wavelength of light, demonstrating new mechanisms for coupling beyond the well-known near-field interactions. The collective excitation over the intermediate-scale arrays is also shown to redirect the scattered light perpendicular to the expected forward scattering. Next, we demonstrate that self-arranged optically bound linear arrays act as optical cavities for co-trapped single-photon emitters, modifying the local density of electromagnetic states in the vicinty of the nanoparticle system. Finally, we probe optically 'dark' modes in a core-satellite nanostructure by exciting magnetic responses separately from electric modes with structured excitation light.

CHAPTER 1

INTRODUCTION

1.1 Optical Properties of Metals and Plasmons

The primary differentiating factor between metals and molecular compounds is the presence of free electrons in a conduction band that spans the material. The mobility of the free electrons leads to material properties such as high electrical conductivity, malleability, and optical reflectivity[1]. In particular, these conduction band electrons respond to an applied external electromagnetic field by producing a charge on the surface of the metal that creates a field in the opposing direction of the applied field and therefore nullifying it in the bulk of the metal[2]. For the case of incident electromagtic waves, the oscillating external field sets up a collective oscillation of the conduction band electrons. At low enough frequencies, this oscillation is capable of 'keeping up' with the external field, retaining the cancellation of the field in the interior of the metal and causing the electromagnetic wave to be reflected. However, at higher frequencies the restoring force that the metal nuclei provide to the displaced free electron cloud is insufficient to shift the cloud in response to the field, and the field from the incident wave is partially trasmitted through the material. The transition point between these two response regimes is known as the plasma frequency, and it coincides to the frequency at which the free electrons would oscillate after being displaced from their natural positions in the metal by a temporary perturbation such as a static electric field briefly applied and removed[3]. The quanta of the oscillations are known as plasmons[4, 5]. Plasma frequencies for most metals are in the ultraviolet region of the electromagnetic spectrum, a fact which gives rise to their strong reflectivity of visible light.

While the optical properties of everyday metallic objects are readily described by the plasma frequency of the material, the interactions between electromagnetic waves and the conduction electrons become more complex when surface effects are considered or the metal

particles approach the wavelength of the incident light. Solutions to Maxwell's equations[2, 6], the set of equations that describe the behavior of electromagnetic fields, along the interface between a metal surface and a non-conducting material reveals that the interface supports an excitation of electromagnetic waves known as a surface plasmons[4, 5]. Surface plasmons differentiate themselves from the bulk plasmons of a metal in that they are dependent on the index of refraction of the dielectric material in contact with the metal's surface. Furthermore, surface plasmons have a longer wave vector $\boldsymbol{k}$ than light of an equivalent frequency, making the excitation of surface plasmons impossible under the ordinary circumstances of light incident on a flat metal surface. Coupling light into the surface wave requires matching of the wave vectors between the incident light and the plasmon mode, made possible by creating an evanescent wave by using a prism on or near the surface and directing the light in at a glancing angle, or by using roughened surfaces where the localized scattering of electromagnetic modes within the metal can provide a wave vector matching condition[4].

When the size of a metallic object approaches the wavelength of light, the available electromagnetic modes for surface plasmons become confined and the resonances are dependent not only on the surrounding medium but also the geometry of the object[5]. The confined resonances are known as localized surface plasmon resonances, referred to as plasmon resonances for the purposes of this dissertation. Similar to the fact that light can be coupled into surface plasmons by roughness in the surface, localized surface plasmon resonances can be excited just by incident light of the proper wavelength. The small size of the nanoparticles relaxes the selection of a wavevector that is exemplified by the energy-momentum dispersion relation for extended metallic systems. For silver and gold nanoparticles on the order of tens to a few hundreds of nanometers in diameter, the plasmon resonances correspond to wavelengths in the visible region of the electromagnetic spectrum, producing strong light absorption and scattering characteristics. In fact, well before the cause of the optical properties of noble metal nanoparticles were known or even before the nanoparticles themselves were ever observed

they were used to create striking color patterns in stained glass; medieval stained glasses were given brilliant red hues by the formation of gold nanoparticles and bright yellows by silver nanoparticles**??**.

The full description of how metallic nanoparticles absorb and scatter light requires solving Maxwell's equations for the particles' distinct geometry and surroundings. These solutions readily exist where approximations can be made such as Rayleigh scattering when the particle is much smaller than the wavelength of light ($d \ll \lambda$)[7] and ray optics when the particle is much larger than the wavelength of light ($d \gg \lambda$)[5]. When the paricle is nearly the same scale as the wavelength of light ($d \approx \lambda$) no such simplfying approximations can be made, however, the case of an isolated perfect dielectric sphere with an incident plane wave was solved analytically by Gustav Mie in 1908[8]. With proper modeling of the dielectric function of the material of the sphere, Mie's calculations can be extended to determine the absorption and scattering cross sections of spherical metallic nanoparticles[7]. The general trend from Mie calculations of metallic spheres in water is that there exist plasmon resonances at visible wavelengths for particles with diameters 50-200 nm that redshift with increasing particle diameter, and that the radiated field transforms from having electronic dipole-like characteristics to quadrupole-like with increasing size[7]. While this was further extended with analytic solutions to elliptical particles by Gans in 1912[9], the majority of systems considered in this dissertation are comprised of spherical particles and can be described by Mie's solution.

1.2 Source-Particle Interactions in the Far-Field

One of the inherent assumptions in the analytic solutions to Maxwell's equations discussed previously is that the incident light takes the form of a plane wave; the polarization is linear and constant over the entire area of illumination, the wave vector does not have any spatial dependence, and the intensity does not vary. In the limit where the light source is far from

the nanoparticle system, any directional dependence of the source will be negligible over the cross section and the assumption is valid. While Rayleigh scattering is valid under a similar set of assumptions, nanoparticles with a diameter on the order of the wavelength of light exhibit an important quantitative difference in the directional distribution of the scattered waves. Smaller particles and molecular scatterers respond to the incident wave as effectively a point-dipole source, and the distribution of the scattered intensity takes the form $I \propto (1 - \cos^2 \theta)$, where θ is the deviation angle from the direction of the incident wave[10]. The scattering is equivalent in the forward (along the same vector as the incident wave) and the reverse direction. With Mie scattering from nanoparticles, the sum of spherical waves from the solutions to Maxwell's equations produces some dipole-like character, but the total scattering intensity is stronger in the forward direction that the reverse[7].

The picture of scattering from plasmonic nanoparticles is further complicated when multiple particles are introduced into the system. Placed within wavelength-scale proximity ($\Delta x \approx \lambda$) to each other, a linear array of metallic nanoparticles has a scattering peak related to the number of particles and the spacing between them (Δx)[11, 12], not just on particle diameter and geometry. The array-dependent resonance is formed by a collective excitation of the plasmon modes in the metallic nanoparticles and has been observed for more complex geometries such as square 2D lattices[13, 14]. It is known that one major contribution to the interactions that lead to the collective excitation comes from dipole-like Mie scattering mode[15]. Chapter 3 of this dissertation explores the dependence of the dipole-like interaction on the polarization of the incident plane wave in colloidal plasmonic nanoparticle systems and how the collective excitation influences the direction-dependent intensity distribution of the scattered light.

The majority of the scattering interactions in nanoparticle and molecular systems is studied in terms of the electric field and electric field enhancements, as the interaction between magnetic dipole modes and an applied electromagnetic field is generally orders of

magnitude weaker than for the electric dipole modes[16], save for a few ionic systems such as rare earth or Lanthanide ions, *e.g.* Eb^{3+} [17]. As such, plasmon modes with magnetic dipole-like character are optically "dark" modes, being difficult to probe with a conventional light source. However, according to the Maxwell-Faraday law of induction, the field of an oscillating magnetic dipole is associated with an alternating, circulating electric field or current[2], and it is possible for electromagnetic waves with polarization dependent on position in their spatial profile, known as vector beams, to have a circulating electric field[18, 19]. Manipulation of plane waves by a diffractive optical element or a nematic liquid crystal can produce vector beams[20], a technique used in Chapter 5 of this dissertation to excite an optically-active magnetic mode in a plasmonic nanoparticle system.

1.3 Source-Particle Interactions in the Intermediate-Field

Once the source brought into close proximity to the nanoparticle system, where the separation between the constituent particles is on the order of the wavelength of the source ($\Delta x \approx \lambda$), the assumption that the scattered light does not influence the source no longer holds. In particular, if the source is the spontaneous emission from an atomic or molecular excited electronic state, the rate of emission is dependent on the surrounding environment. Weisskopf and Wigner theorized that the emission rate for an emitter in free space Γ_0 is dependent on the energy difference between the initial and final electronic states $\hbar\omega_0$, and the matrix element coupling the states μ_{12}, $\Gamma_0 = \frac{{\omega_0}^3 {\mu_{12}}^2}{3\pi\epsilon_0\hbar c^3}$ [21, 22]. When the emitter is no longer in free space, *i.e.* it is allowed to interact with surrounding matter, the rate of the transition from the excited state to the ground state becomes dependent on the number of available radiating electromagnetic states in the environment. The density of these states, $\rho(\omega_0)$, can be derived from an extension of Maxwell's equations with consideration of the quantized nature of light, known as quantum electrodynamics[23]. For an electromagnetic wave to propagate through space, there must exist a photon state with the proper energy and wave vector. The number

of electromagnetic states per unit energy at a particular point in space and for a particular wave vector is known as the local density of states (LDOS). In vacuum, the density of states $\rho(\omega_0)$ is solely dependent on the photon energy, growing as the square of the frequency of light[22].

The way a material influences the LDOS can be described in terms of the spatially-dependent index of refraction of the system. Interfaces between two materials with a large index of refraction disparity reflect incident electromagnetic waves. A wave propagating between two such interfaces aligned parallel to each other and incident normal to their surfaces will interfere with itself upon reflection and if the wavelength is an integral multiple of the spacing between the surfaces the interference will be constructive. Geometries designed to produce constructive interference in a similar manner to this are known as optical cavities and increase the density of states for the electromagnetic modes that exhibit constructive interference in the interior of the cavity. Purcell predicted that the rate of nuclear magnetic transitions could be increased by placing the the atom inside a properly-designed cavity[24]. Generalizing to spontaneous emission in a cavity, the ratio of the emission rate inside the cavity (Γ) to that in vacuum, $F_P = \Gamma/\Gamma_0$, is known as the Purcell Factor[22, 23]. Following the derivation of the free space spontaneous emission rate, the emission rate, Γ, in the cavity is proportional to the LDOS; formally by $\Gamma = \frac{2\pi {\mu_{12}}^2 {E_0}^2}{\hbar^2}\rho(\omega_0)$. The Purcell Factor is also equivalently proportional to the ratio of the quality factor Q of the cavity, a measure of how the cavity dampens the oscillations of the mode, to the mode volume V, the volume to which the cavity confines the supported electromagnetic mode; $F_P = \frac{3Q\lambda^3}{4\pi^2 V}$ [22].

Research on photonic crystal arrays[25] attempts to create dielectric material geometries in which the Purcell effect causes multiple order-of-magnitude enhancements[26, 27] or reductions[28] in the decay rates of embedded emitters. The simplest case of a photonic crystal array is a material that consists of parallel sheets of dielectric materials that alternate back and forth between two different indexes of refraction. The periodic nature of the

structure lends itself to electromagnetic modes that propagate along the direction of repetition (perpendicular to the surfaces of the sheets) with wavelengths that match the characteristic distance between the alternating layers, while modes whose wave vectors lie off-axis to the structure or have a wavelength mis-matched with the characterisitic unit structure dissipate due to destructive interference[25]. An embedded emitter will experience an enhancement to its radiative rate if the frequency and direction of the emission is commensurate with the design wavelength and direction of the photonic crystal, and as such has been observed experimentally in lithographically-prepared lattices[29].

Chapter 4 of this dissertation presents a method for creating an effective optical cavity using a self-assembled optical matter system.

1.4 Source-Particle Interactions in the Near-Field

As the separation between an emitter and a plasmonic nanoparticle is reduced well below the wavelength of the emitted light ($\Delta x \ll \lambda$), the system enters a regime where the excited state emitter can couple strongly to the plasmon resonance, producing large enhancements in the in the radiative rate[30], or creating a spectrally narrow transparency in the scattering peak of the plasmon resonance[31]. Considerations of the nature of the source need not be limited to the decay of a discrete excited electronic state - the scattered light from a plasmonic nanoparticle can radiate in the direction of and interact with another particle in the system; interactions with secondary scattering enable optical binding as discussed in Section 1.5. In the near-field, coupling between the electromagnetic fields radiated by the individual particle modes that enables collective plasmon modes is enhanced by stronger coupling and the optical response approaches that of a single structure with a similar geometry[32, 33]. The system presented in Chapter 5 leverages the near-field coupling between single-particle plasmon modes to create a structure that allows for a circulation of electron density, resulting in the optical magnetic mode described in Section 1.2.

1.5 Optical Trapping and Optical Matter

As discussed in Sections 1.2 and 1.3, the optical properties of collections of colloidal metal nanoparticles are dependent on their arrangement. Therefore, the ability to readily manipulate the positions of the particles is of utmost importance to the research in this dissertation. One of the advantages of working with colloidal particles is that they can be manipulated by using focused coherent light, a phenomena known as optical trapping[34, 35]. First observed with micron-scale dielectric particles[34], trapping results from a balance of forces as the photons from the focused laser beam impart momentum to the particle by scattering and refraction. The scattering of light from the interface between the surrounding medium and the dielectric particle drives the particle in the direction of the propagation of the focused laser, known as the scattering force. Refraction of the light as it passes through the particle alters the direction of the incident light and therefore the momentum of the photons; by conservation of momentum, the particle enounters a force directed towards the center of the laser focus, known as the gradient force.

While it was originally assumed that optical trapping did not apply to reflective substances such as metallic nanoparticles, the balance of optical forces acting on the particles was demonstrated as an interaction with the particle's plasmon mode[36, 37]. The degree to which the incident electromagnetic field induces a temporary dipole moment in a material is known as the polarizability, and the induced dipole moment experiences a force proportional to the dot product of the electric field and the dipole. Due to the screening of the external electric field from the interior of a metal by the displacement of the conduction band electrons, the polarizability of metallic nanoparticles is negative when the frequency of the driving field is lower than the plasmon resonance of the particle and turns postive when the frequency is higher than the plasmon resonance. Integrating the Maxwell stress tensor of the surface of a particle with this induced dipole moment reveals a force acting on the particle dependent

on the intensity gradient of the incident field. When the wavelength of the laser is longer (to the red of) the plasmon resonance, this force is directed towards the laser's focal point, providing an attractive force to oppose the repulsive force from radiation pressure. With a tight enough focus, this gradient force balances the strong scattering force and the metallic particle becomes trapped in the beam.

When multiple metallic particles are present in the electromagnetic field from the laser used for trapping, scattering from once particle interferes with the incident field, creating locations of enhanced field intensity dependent on the polarization and wavelength of the incident field. As the optical trapping gradient force is increased where the field is enhanced, a second particle in one of these locations will experience an effective potential energy well. Thus two particles can arrange themselves in the field according to mutual interactions between the incident light and the scattering from the other particle, a phenomenon known as optical binding[38, 39]. This readily leads to linear arrays of metallic nanoparticles aligned in a direction perpendicular to the polarization of the indicent field[40]. More complex geometries are available by structuring of the intensity and phase profile of the incident beam. In Chapters 3 and 4 the arrangements of metallic nanoparticles are achieved by imposing a spatially-dependent phase delay on the incident beam at the optical conjugate plane to the focus of the lens used in those experiments. The electric field at the focus of a lens is related to the electric field of the beam by a Fourier transform relationship, and thus the spatial profile of the phase of the incident beam at the conjugate plane leads to modification of the spatial profile of both the intensity and phase of the beam at the focus.

The interparticle interactions and thermal fluctuations in systems of optically trapped and bound nanoparticles in solution bear similarities to the motions of molecules in condensed matter, and as such was termed "Optical Matter" by Burns in 1990[39]. The large scattering cross section of metallic nanoparticles not only makes the study of the interactions simpler by only requiring optical microscopy as opposed to electron or atomic force microscopy to

resolve the structures, but also enhances the optical forces generated by the scattered light, extending their range such that multi-body interactions can be observed

1.6 Structure of this Dissertation

Beginning in Chapter 2 with a description of the experimental optical setups, samples, and analysis methods used, this dissertation presents three regimes of shaping electromagnetic fields with colloidal metal nanoparticles. Chapter 3 examines the collective plasmon resonances of linear arrays of silver nanoparticles under incoherent and coherent plane wave excitation as well as the directional dependence of the scattering resonances. Next, creation of similar linear arrays in an optical matter system and the influence of their collective resonances on single-photon emitters in the optical matter system is described in Chapter 4. Finally, Chapter 5 discusses the use of nanoparticles in near-field proximity to create a structure with a collective resonance that is a magnetic mode at optical frequencies under vector beam illumination.

CHAPTER 2

EXPERIMENTAL AND SIMULATION METHODS

2.1 Optical Setup for Array Deposition

For the creation of static arrays fixed on a substrate (Chapter 3), the optical setup depicted in Figure 2.1, similar to the one used in [40], was used to manipulate the position of the silver nanoparticles with ∼100 nm precistion [41] [42] before deposition on the glass surface. The output of a home-built Ti:Sapphire continuous-wave laser, pumped by a Spectra-Physics Millenia Vs 5.0 W laser, was passed through a half-wave plate (HWP) followed by a polarizer (P1) oriented parallel to the optical table, such that the power of the trapping beam could be controlled by the rotation of the half-wave plate. The first mirror (M1) directed the beam onto the spatial light modulator (SLM, Hammamatsu X10468-02), which imparted a spatially-dependent phase delay onto the wavefront. The beam then passed through a pair of lenses (L1, f=750 mm and L2, f=500 mm) which reduced the beam size and collimated it at a diameter of ∼8 mm, equal to the back aperture of the microscope's objective lens. The next two mirrors (M2 and M3), raised the beam to the height of the rear port of the microscope body (Olympus IX-71). Just before the rear port of the microscope, a dichroic beamsplitter (DBS) directs the beam into the microscope while allowing for a ∼400 nm excitation beam to be aligned co-linear to the trapping beam (described below). A dichroic beamsplitter (Semrock T470lpxr) reflected the trapping beam into the microscope objective (Olympus UPlanSApo NA 1.2, 60x water immersion) that focused it onto the sample.

For the samples where the quantum dots were drop-cast on the surface and the AgNP arrays were deposited around them, the quantum dots were excited by frequency doubling the output from a home-built cavity-dumped mode-locked Ti:Sapphire oscillator, based on the designs of Spence *et al.*[43] and Liau *et al.*[44]. Figure 2.2 shows both an image and a schematic of the system. The oscillator was pumped by a Spectra-Physics Millennia Xs laser

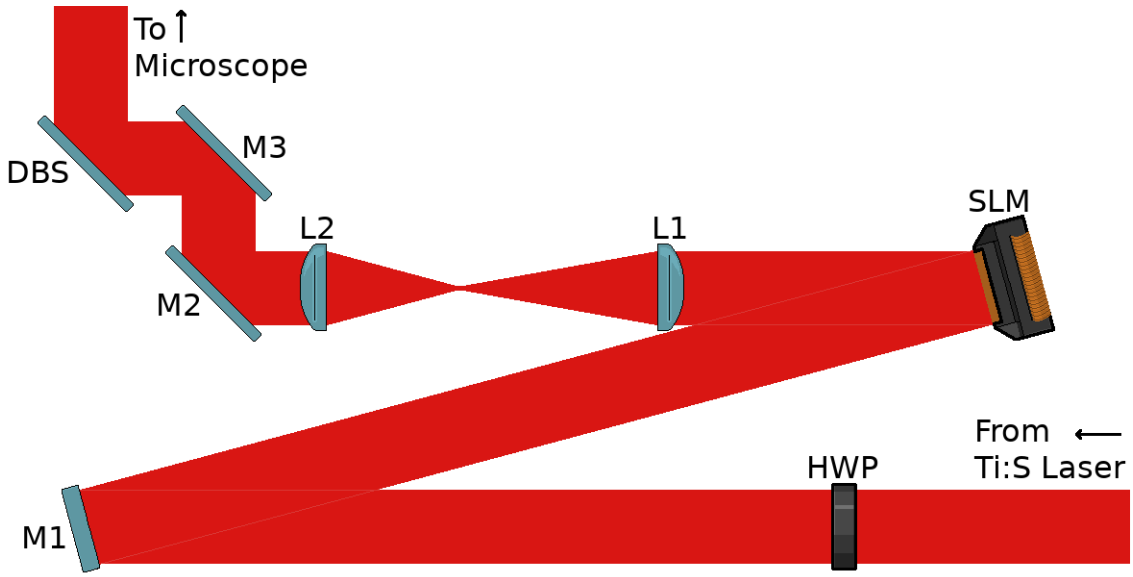

Figure 2.1: Schematic of the optical setup for shaping the trapping beam. HWP: Half-wave plate; M1: Mirror; SLM: Spatial light modulator; L1: lens, f=750 mm; L2: lens, f=500 mm; M2, M3: Mirror; DBS: Dichroic beamsplitter.

operating at 4.0 W output power, creating pulses in the cavity at a rate of 90.1 MHz once mode-locked. To couple the beam out of the cavity, RF pulses synchronized to the repetition rate of the oscillator were directed into a Bragg cell that deflected every 64th pulse away from the end mirror (M7 in Figure 2.2b), creating a pulsed output running at 1.41 MHz and a power of 38 mW. Figure 2.3 shows the spectrum of the output and an second-harmonic autocorrelation signal from the output pulses.

The ∼780-840 nm pulses were frequency-doubled by a beta-barium borate (BBO) crystal and aligned to be co-linear with the trapping beam in order to excite the quantum dot fluorescence to locate them. A pair of lenses acted as a beam telescope to expand the beam and control the divergence such that the focal spot covered an area ∼2-3 μm in diameter on the surface of the sample.

The sample was illuminated by incoherent white light through a bright-field condenser and the scattering was collected by the same objective used to focus the trapping beam onto the

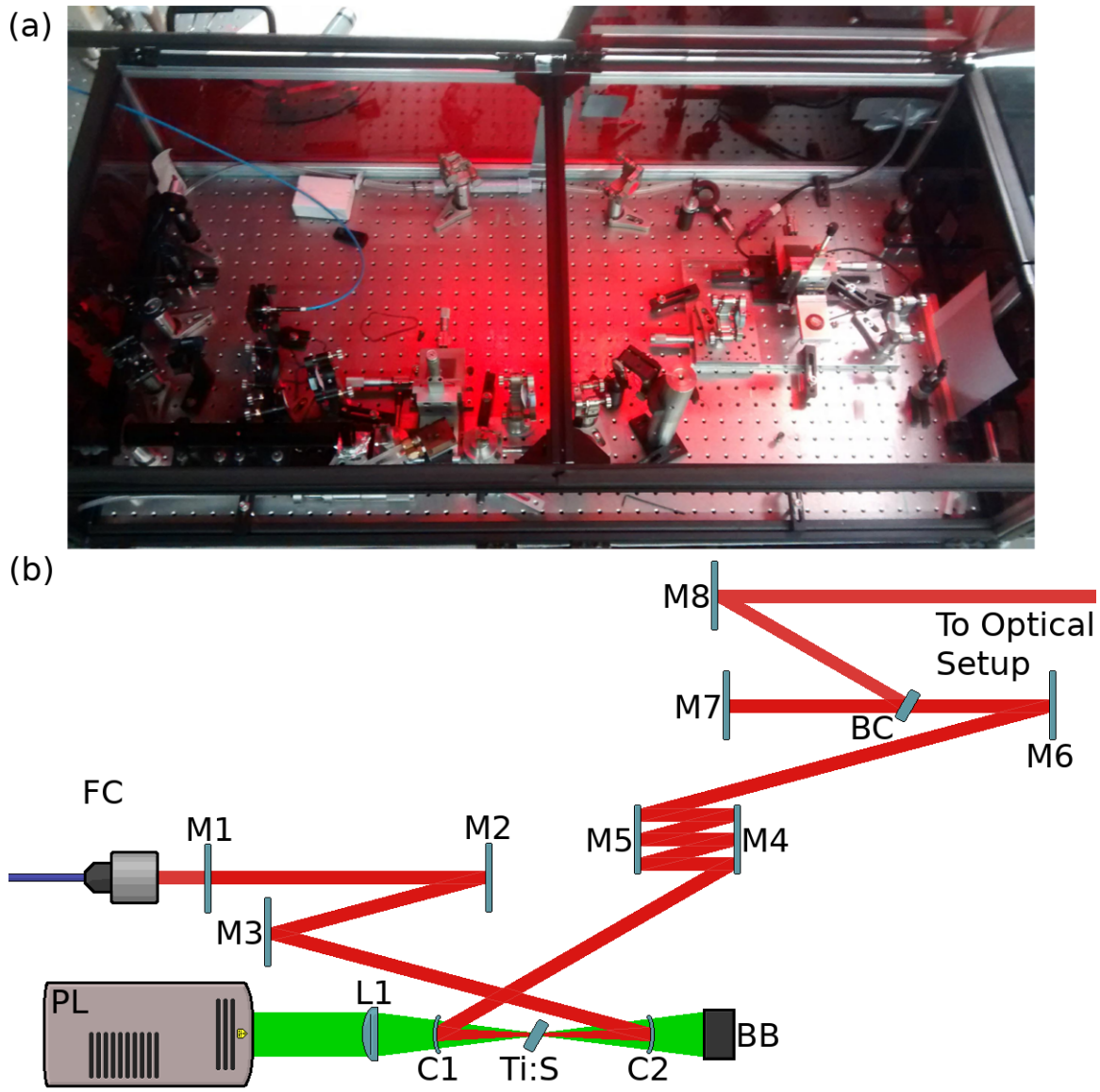

Figure 2.2: (a) Image of the mode-locked Ti:Sapphire oscillator cavity. (b) Schematic of the mode-locked Ti:Sapphire oscillator cavity. PL: Pump laser; L1: Lens; C1, C2: Curved dichroic mirrors; BB: Beam blocker; Ti:S: Ti:Sapphire crystal; M1: End mirror, 1% transmission; FC: Fiber coupler for monitoring cavity pulses; M2-M5: Dispersion-compensating mirrors; M6: Mirror; BC: Bragg cell; M7: End mirror; M8: Mirror.

sample. The remaining scattering from the trapping beam was removed by a short-pass filter with a cutoff at a wavelength of 635 nm. The dark-field scattering image of the nanoparticles was magnified by an additional factor of 1.5x before being collected by a sCMOS array

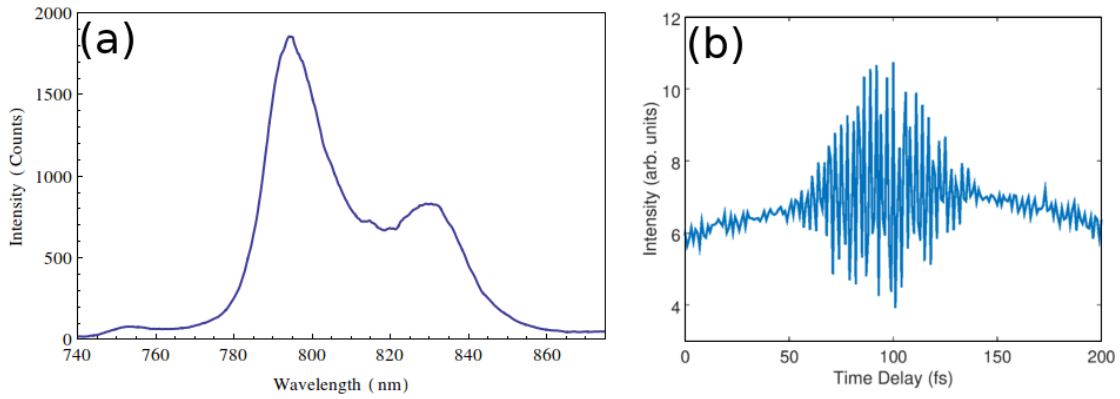

Figure 2.3: (a) Spectrum of the pulses output from the home-built cavity-dumped Ti:Sapphire oscillator before frequency doubling. (b) Time autocorrelation of the laser pulses measured by second harmonic generation.

detector (Andor Neo) attached to the eyepiece of the microscope.

In order to measure the fluorescence decay rate from the quantum dots, the emission excited by the frequency-doubled pulsed laser was collected by the same objective used to focus both the excitation and trapping beams onto the sample, and is directed out the side port of the microscope. Excess scattered light from these beams is removed from the measurement by a pair of bandpass filters (Chroma HQ580/13). A pair of lenses (f=100 mm and f=200 mm) in a 4f relay system created an image of the quantum dot fluorescence at the position of a 50 μm diameter multimode optical fiber. The focal lengths of these lenses were chosen such that the diffraction-limited spot size from the fluorescence is magnified to match the aperture of the fiber; the 96x magnification of the microscope increases the spot size to $\sim$45 μm, which is magnified by the ratio of the microscope's tube lens (f=180 mm) to the final lens the relay (f=200 mm) to $\sim$50 μm.

The optical fiber was attached to an avalanche photodiode (APD, Perkin-Elmer SPCM-AQR-15-FC) and the photon counting signal was routed to a time-correlated single-photon counting (TCSPC) card (Becker-Hickl SPC-150).

2.2 Optical Setup for Dark-field Spectroscopy and Fluorescence Measurements from Fixed AgNP Lattices

The 1D Ag synthetic photonic lattices in Chapter 3 were imaged and spectrally characterized by dark-field microscopy with a high numerical-aperture dark-field condenser (Olympus, U-DCW, NA = 1.2 - 1.4) and a 60X water immersion objective (NA $\leq$ 1.2, Olympus UPLSAPO). Both incoherent (tungsten-halogen) and coherent fiber laser-continuum (Fianium, WL-SC400-4) white light sources were used for dark-field spectral measurements over the 400-950 nm wavelength range. The images of the 1D lattices were recorded using a sCMOS camera (Andor, Neo). The dark-field scattering spectra were recorded by an EMCCD array detector (Andor, Newton) connected to a 303 mm Czerny-Turner imaging spectrometer (Andor, Shamrock 303i) coupled to the side port of the microscope via a home-built achromatic 4f relay system.

The quantum dot samples were illuminated by the coherent white light source passed through an optical filter to have a center wavelength of 445 nm and a bandpass of 30 nm. The collected fluorescence was focused by a home-built 4f relay system onto a 50 μm optical fiber coupled to an a avalanche photodiode (Perkin-Elmer, SPCM-AQR-15-FC). The fluorescence decays were obtained using a time-correlated single-photon counting card (Becker-Hickl, SCP-150), synchronized to the RF signal from the coherent light source. The fluorescence for the conjugate images was collected with a 100x oil immersion objective (NA $\leq$ 1.4, Olympus, UPLSAPO) and measured by an EMCCD (Andor, iXon).

2.3 Optical Setup for Cotrapping

The cotrapping experiments described in Chapter 4 were completed using a second optical setup with a design similar to the one used to deposit the fixed arrays but with a few key differences. A home-built Ti:Sapphire continuous-wave laser, pumped by a Spectra-Physics Millenia Vs 5.0 W laser, was directed onto a pair of beam stabilization mirrors (Optics in

Motion Analog Fast Steering Mirror), each followed by a glass window aligned at a 45-degree angle to the beam such that a small (∼1%) portion of the laser power was directed onto two separate quadrant photodiodes. The output from each photodiode was sent to an electronic controller for solenoids in the mounts of each stabilization mirror, forming a negative feedback loop between the orientation of each mirror and the relative intensity of the beam in each quadrant of the photodiodes. Any deviation in the beam due to temperature or humidity fluctuations in the room was therefore corrected by automated adjustment of the stabilization mirrors keeping the relative intensity in each quadrant of their respective photodiodes equal.

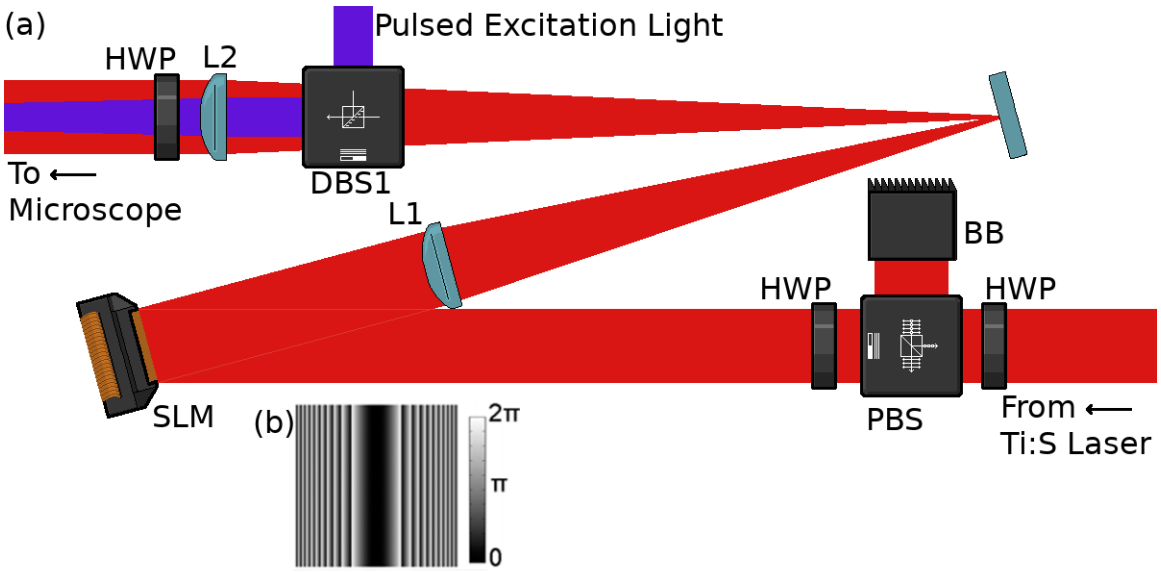

Figure 2.4: (a) Schematic of the optical setup for shaping the trapping beam. HWP: half-wave plate; PBS: polarizing beamsplitter; BB: beam blocker; SLM: spatial light modulator; L1: lens, f=750 mm; DBS1: dichroic beamsplitter, 650 nm long pass; L2: lens, f=1000 mm. (b) Phase mask used to create the linear intensity profile at the focal point of the trapping beam. The grayscale represents the voltage values used at each pixel on the SLM to impart a phase delay at that point on the beam, where black is no phase delay and white is a 2π delay.

Continuing from this point, the setup is shown in Figure 2.4; the beam was aligned through a half-wave plate (HWP) followed immediately by a polarizing beamsplitter cube (PBS). The rotation of the first HWP allowed for rotation of beam's polarization state away from horizontal to the optical table, effectively controlling the relative power sent to the

transmission and reflection paths from the beamsplitter cube. While this was designed to create a second optical trap that could be made colinear with the first, the second beam was blocked (BB) and the rotation of the HWP was used as a fine control over the power of the trap. Since the polarization state transmitted by PBS was parallel to the table and the spatial light modulator in this setup was optimized to produce the maximum phase modulation for light polarized perpendicular to the table, a second half-wave plate was added immediately following the beamsplitter to rotate the polarization to perpendicular to the table. The spatial light modulator (SLM, BNS/Meadowlark HSPDM512-785) reflected the trapping beam through the first of a pair of lenses (L1, f=75 mm) followed by a mirror that directed the beam through a dichroic beamsplitter (DBS1, Thorlabs DMLP650R). A third half-wave plate set the desired linear polarization for the trapping beam to either the x- or the y-axis in the lab frame for the sample. The second lens (L2, f=100 mm) re-collimated the beam once it had expanded to the point that it filled the rear aperture of the microscope objective (9.7 mm in diameter). Two mirrors in a periscope configuration raised the trapping beam to the height of and directed it into the rear port of the microscope (Nikon eclipse Ti-E).

In order to excite the quantum dots in the samples used, the output of a pulsed supercontinuum fiber laser (Fianium WL400-4-PP) operating at 10 MHz was coupled into a computer-controlled variable interference filter (Fianium SuperChrome) set to pass a 30 nm wavelength band centered at 445 nm. Further rejection of out-of-band light was accomplished by a pair of bandpass filters (Chroma HQ445/30) as the interference filter alone was determined to not reduce the leftover ∼580 nm light from the supercontinuum laser enough to not be observable in the fluorescence decay measurements. A series of mirrors directed the excitation beam into the dichroic mirror DBS1 shown in Figure 2.4 such that it was colinear with the trapping beam. Both beams were directed into the microscope objective (Nikon Plan Apo IR NA 1.27 60x water immersion) by a dichroic beamsplitter (Chroma T470lpxr)

located in the turret of the microsope.

Samples were illuminated from above by a 470 nm blue LED (Thorlabs M470L3) focused onto the sample by a dark-field condenser. Both the scattering from the dark-field illumnation and the quantum dot fluorescence were collected by the same objective used to focus the trapping and excitation beams onto the sample. The trapping beam was blocked just below the microscope turret by a notch filter (Semrock StopLine NF03-785E-25) and a shortpass filter (Semrock BrightLine FF02-694/SP-25). An neutral density filter in the body of the microscope split the collected light between the ports of the microscope, with 20% going to the eyepiece for imaging and 80% to the side port for photon counting measurements.

The light directed towards the eyepiece was re-directed to a C-mount port to which a dual-channel imaging system was attached (Optical Insights DualView). The DualView was designed to split an image according to either wavelength or polarization depending on the installed beamsplitter and align the split image side-by-side on an array detector. For the experiments conducted in this dissertation, a dichroic beamsplitter with a cutoff wavelength of 560 nm was installed to split the quantum dot fluorescence into one channel and the combined dark-field scattering and scattering of the excitation beam from the silver nanoparticles into the other. The two-channel image was collected by a sCMOS array detector (Andor Neo).

The light coupled out the side port of the microscope was collimated by a 20 mm focal length lens and the scattered excitation beam and dark-field scattering were filtered out by a bandpass filter (Chroma HQ580/13) centered at the fluorescence wavelength of the quantum dots used in the experiment. The collimated quantum dot fluorescence was collected by and focused onto the aperture of a 50 μm diameter multimode optical fiber (Ocean Optics P50-2-UV-VIS) by a fiber collimator (Thorlabs F260FC-A). The output of the optical fiber was connected to avalanche photodiode (APD, Perkin-Elmer SPCM-AQR-15-FC) and the photon counting signal was routed to a time-correlated single-photon counting (TCSPC) card (Becker-Hickl SPC-150).

2.3.1 Determining Trapping Beam Polarization at the Sample Position

The polarization state of the trapping beam at the position of the sample was measured by removing the sample cell and the microscope objective and placing a polarizer with a known direction at the position of the sample on the microscope stage. The power of the trapping beam was measured by placing a power meter (¡xx¿) directly after the polarizer in the direction of the beam propagation. The polarizer was then rotated by a known angle, creating an intensity function as a function of polarizer angle. The half-wave plate directly before the microscope was then rotated to produce the maximum difference between the lowest and highest intensity of the trapping beam measured at the sample position as the polarizer is rotated and so that the maximum intensity was observed when the polarizer was aligned along the y-direction of the microscope's translation stage.

2.3.2 Spatial Registration of Dual-Channel Imaging

Figure 2.5: Scattering image of the trapping beam taken by the dual-channel imaging system used to register the two channels against each other. The region of the image between the two 130x50 pixel windows used for the registration has been cropped out. The scale bar is 2000 nm.

In order to obtain the position of the QD relative to the AgNP array, an image of the trapping laser was taken after removing the notch and short pass filters from the optical setup and reducing the power of the trapping beam below the saturation threshold of the sCMOS detector. This allowed for structure of the trapping beam to be visible in both channels of the of the imaging setup, creating a reference image for registering the two channels against each other. A 130x50 pixel window that includes the optical trap was taken from both the

far left and far right side of the reference image, shown in Figure 2.5, and the windows were registered against each other by determining the pixel shift that produces the maximum cross-correlation between these two images. The same windows were applied to the videos of the QDs cotrapped in the AgNP arrays, and the positions of the particles were determined by particle tracking with the MosaicSuite software package for ImageJ[45]. The pixel shift from the trapping laser registration was subtracted from the pixel positions of the QD as an offset.

2.3.3 Time Registration of Imaging and Photon Counting

To determine the time offset between the beginning of the dual-wavelength-channel imaging and the fluorescence emission photon counting for each associated video, at the beginning of each video and after starting both instruments' data collection, the excitation beam was blocked and unblocked twice in rapid succession to create a marker signal in both meaurements. This marker was evident as a brief dimming in the scattering image collected from the AgNPs and as a dip in the time trace of the photon counts from the quantum dot. The signal was characterized in the scattering images by calculating the average pixel intensity over a rectangular region of the image encompassing the entirety of the focal area for the scattering and trapping beams,

$$I_{\text{scat}}(f) = \frac{\sum_{y=y_1}^{y=y_2} \sum_{x=x_1}^{x=x_2} I_{\text{pixel}}(f, x, y)}{(x_2 - x_1)(y_2 - y_1)} \tag{2.1}$$

where f is the frame number of the video, $x_1,\ x_2$ and $y_1,\ y_2$ are the limits of the rectangular region in the x- and y- directions, respectively, and $I_{\text{pixel}}(f, x, y)$ is the value of a single pixel at postion (x, y) and at frame f.

As the TCSPC measurement had a maximum count rate of the repetition rate of the laser used for excitation, 10 MHz, and the video was recorded at a frame rate of 36.7 Hz, the photon counts had to be downsampled to the frame rate of the video. Each photon count from the TCSPC meaurement was tagged according to two different timescales - the 'macro time' M, tracking the number of laser pulses since the beginning of the measurement,

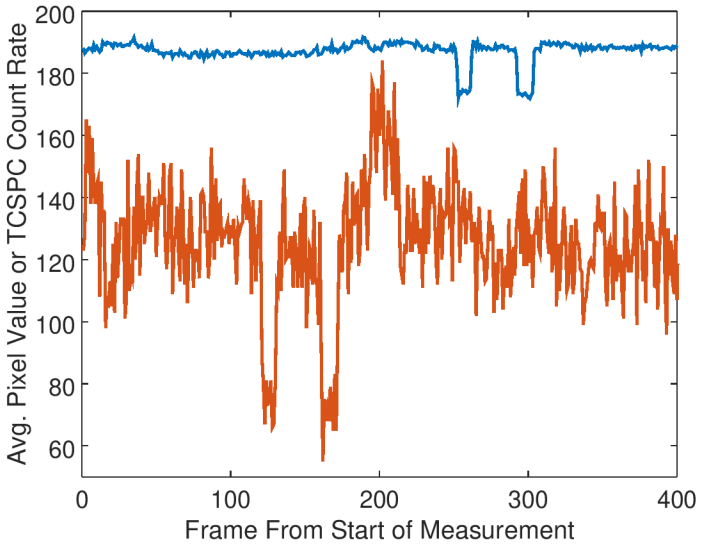

Figure 2.6: Pixel value averaged over the 130x50 pixel window containing the dark-field scattering from the AgNP array (blue) compared to the number of photon counts per video frame from the TCSPC measurement from the same video (orange) for the first 400 frames from the start of each respective measurement.

and the 'micro time' m, an integer in the range 0-4095 that marked how long after the RF trigger signal from the laser reached the TCSPC instrument the trigger from the APD for a fluorescence photon arrived. Thus, the lab time for a particular photon event was given by $t_P = (M + \frac{m}{4096})/10$ MHz. The photon events were then placed in bins with a width equal to the frame rate of the imaging measurement according to their lab time tag, *i.e.* the number of photons N_1 with $0 \leq t_P < 1/36.7$ Hz was the value of the photon count time trace for the first frame, $I_{\text{fluor}}(f = 1) = N_1$, the number of photons N_2 with $1/36.7$ Hz $\leq t_P < 2 \times 1/36.7$ Hz was $I_{\text{fluor}}(f = 2) = N_2$, etc. Figure 2.6 shows the first 500 frames of photon count time trace compared to the first 400 frames scattering intensity time trace; the modulation of the excitation beam is evident in both signals.

The binning of the TCSPC data was repeated with sub-frame offsets in order to provide resolution below the integer frame level; a series of $I_{\text{fluor}}(f; f_\tau)$ time traces were created where f_τ is the sub-frame offset such that $I_{\text{fluor}}(f = n; f_\tau) = N$ is the number of photons N with

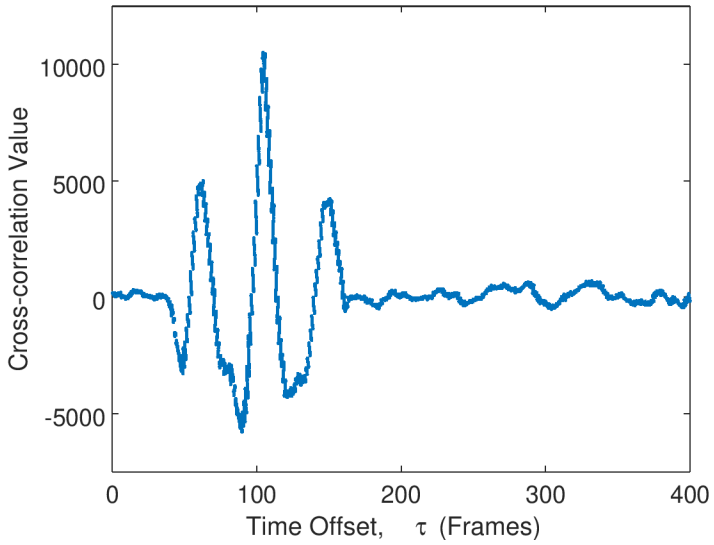

Figure 2.7: Cross-correlation function $A(\tau; f_\tau)$ of TCSPC time trace against the scattering image time trace for a single video as a function of both the integer frame offset τ and the sub-frame offset f_τ.

$((n-1)+0.01f_\tau) \times 1/36.7$ Hz $\leq t_P < (n+0.01f_\tau)/36.7$ Hz, resulting in a resolution of 0.01 video frames. The lab time offset in video frames τ between the two signals was determined by the cross-correlation of the region of I_{fluor} containing the modulation of the excitation beam against a corresponding region of I_{scat},

$$A(\tau; f_\tau) = \frac{\sum_{f=f_1}^{f=f_2} \left[I_{\text{fluor}}(f; f_\tau) - \mu_{\text{fluor}}(f_1, f_2)\right] \times \left[I_{\text{scat}}(f+\tau) - \mu_{\text{scat}}(f_1+\tau, f_2+\tau)\right]}{f_2 - f_1} \tag{2.2}$$

where $\mu_{\text{fluor}}(f_1, f_2)$ and $\mu_{\text{scat}}(f_1+\tau, f_2+\tau)$ are the means of their respective time traces over the selected frame region $f_1 \leq f \leq f_2$ for the TCSPC data and $f_1+\tau \leq f \leq f_2+\tau$ for the scattering image. An example of this cross-correlation function for a single scattering video and its associated TCSPC data is shown in Figure 2.7. The first peak in $A(\tau; f_\tau)$ is the offset at which the second of the two dips in the TCSPC time trace due to the modulation of the excitation beam is matched to the first of the two dips in the scattering image time trace, and the third peak is the offset at which first dip in the TCSPC trace is co-incident with

the second from the scattering trace. The maximum of $A(\tau; f_\tau)$, which occurs at the central peak, is the offset at which the both of the dips from the two time traces are matched and therefore represents the lab time offset in terms of video frames between the two data sets.

2.4 Optical Setup for Vector Beam Spectroscopy

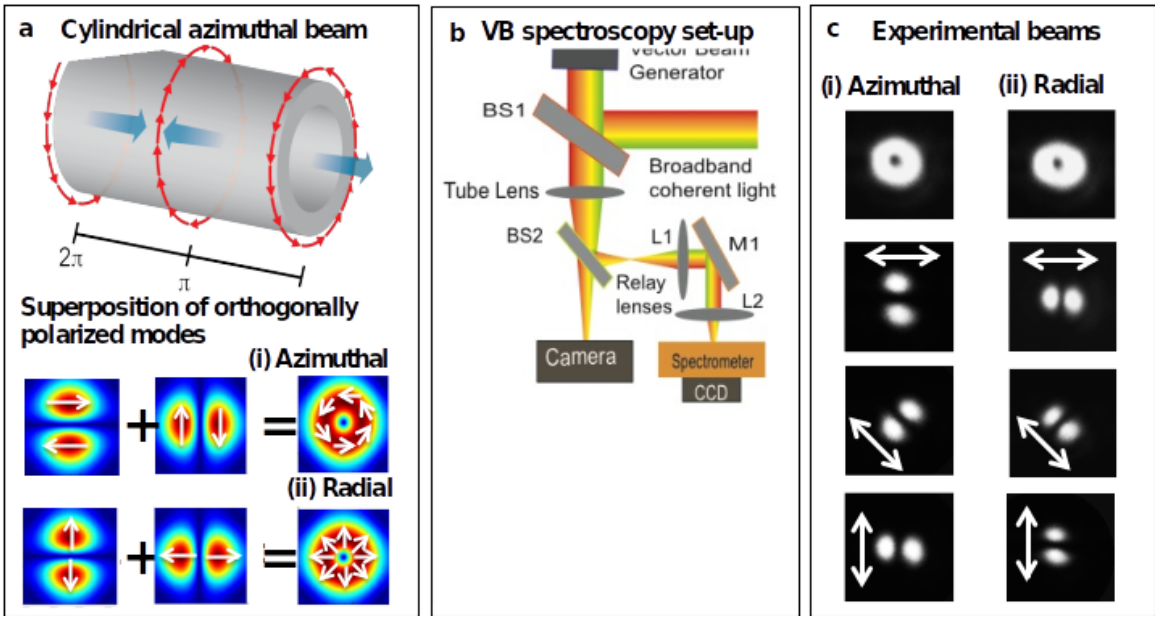

Figure 2.8: (a) Schematic representation of CVBs with right- and left-handed azimuthal polarization; and the superposition of orthogonally polarized HG_{01} and HG_{10} modes forming azimuthal and radial CVBs. (b) Schematic of the CVB spectroscopy and microscopy set-up. BS, partially reflecting or movable Beam Splitter; L, Lenses; M, Mirror. (c) Experimental generation of broadband CVBs with azimuthal and radial polarization and their linear components as determined by inserting a linear polarization analyzer in front of the detector, and measuring the beam in the forward direction.

For the experiments presented in Chapter 5, we use a liquid-crystal (LC) based polarization converter (from ARCoptix) that uses twisted nematic liquid crystals sandwiched between one uniform and one circularly rubbed alignment layer to generate azimuthally and radially polarized CVBs[46]. The polarization-guiding effect in this LC based device is valid for $\pi d\Delta n/\chi \gg \lambda$, where Δn is the birefringence of the LC, d is the cell thickness, χ is the

twist angle of the LC, and λ is the wavelength of the incident light[46]. For high $d\Delta n$, the polarization reorientation effect is valid over a broad wavelength range – hence, the polarization converter can be utilized to produce broadband CVBs, provided that the wavelength-dependent phase difference of the retarder used to eliminate the phase difference in two halves of the LC device is accounted for. A schematic of the vector beam spectroscopy and microscopy set-up is shown in Figure 2.8. We use a spatially (but not temporally) coherent (broadband) white light continuum (400-2700 nm) source (Fianium WL400-4-PP) for our spectroscopic measurements. The white light continuum is coupled to an inverted optical microscope (Olympus IX-81) equipped with a 100x oil immersion objective with numerical aperture NA = 1.4 (Olympus SAPO). The vector beam generator was placed just before the microscope objective. The beam quality was monitored in the forward direction using an objective and tubelens. The back-scattered images of the sample plane were recorded by a sCMOS array detector (Andor Neo) connected to the trinoc eye-piece of the microscope and spectra acquired by an EM-CCD (Andor Newton) connected to an imaging spectrometer coupled to the side port of the microscope via a home-built achromatic $4f$ relay system.

Figure 2.8 shows the images of the broadband azimuthally and radially polarized beams that were generated experimentally, and detected in transmission. The spatial orthogonality of the polarizations associated with the azimuthal and radial beams were detected by inserting a linear polarizer in front of the array detector at different angles as shown in Figure 2.8.

2.4.1 Multipole Expansion Analysis of Vector Beam Scattering Spectra

In order to compare the experimental scattering spectra from the core-satellite nano-clusters to the FDTD simulated results in Chapter 5, the experimental spectra were modeled as a sum of Gaussian curves with the functional form

$$f(\lambda) = \sum_{i}^{n} a_i e^{-\frac{(x-x_i)^2}{2\sigma_i^2}} \tag{2.3}$$

by using nonlinear least-squares fitting after smoothing by Tikhonov regularization. However, when compared to the simulated multipole expansion spectra, it becomes clear that the various multipoles are not well described by these individual peaks. This is in sharp contrast to spectra of metallic spheres calculated by Mie theory, where each peak can be assigned to a certain electric multipolar mode; the multipole expansions of the nano-cluster scattering have numerous peaks each and overlap with each other, as shown in Figure 5.4.

For a better comparison, the multipole expansion modes from the simulation were considered as a set of 'basis functions'. Expanding the experimental spectra in terms of overlap integrals with the multipoles as a basis highlights the character of the vector beam scattering from the nano-clusters. The smoothed experimental spectra were normalized according to the integral over the wavelength window of the original measurement,

$$\bar{f}(\lambda = \frac{f(\lambda)}{N_e},\ N_e = \int_{\lambda=500\text{nm}}^{\lambda=1000\text{nm}} f(\lambda)d\lambda \tag{2.4}$$

Each of the multipole expansion spectra from the FDTD simulated results were also normalized, but by the integral over the full simulated spectra:

$$\bar{s}_i(\lambda) = \frac{s_i(\lambda)}{N_s},\ i = eD, mD, eQ, mQ, ...,\ N_s = \int_{\lambda=500\text{nm}}^{\lambda=1000\text{nm}} [\sum_i s_i(\lambda)]d\lambda \tag{2.5}$$

The overlap between the experimental spectra and each of the multipole expansions was then calculated by the integral

$$O_i = \int_{\lambda=500\text{nm}}^{\lambda=1000\text{nm}} \bar{f}(\lambda)\bar{s}_i(\lambda)d\lambda \tag{2.6}$$

For the example of the scattering of the linearly polarized beam from the 165 nm nanocluster, the spectra had the highest overlap coefficient (O_i) with the electric and magnetic expansions of the simulated spectra (see Figure 2.9).

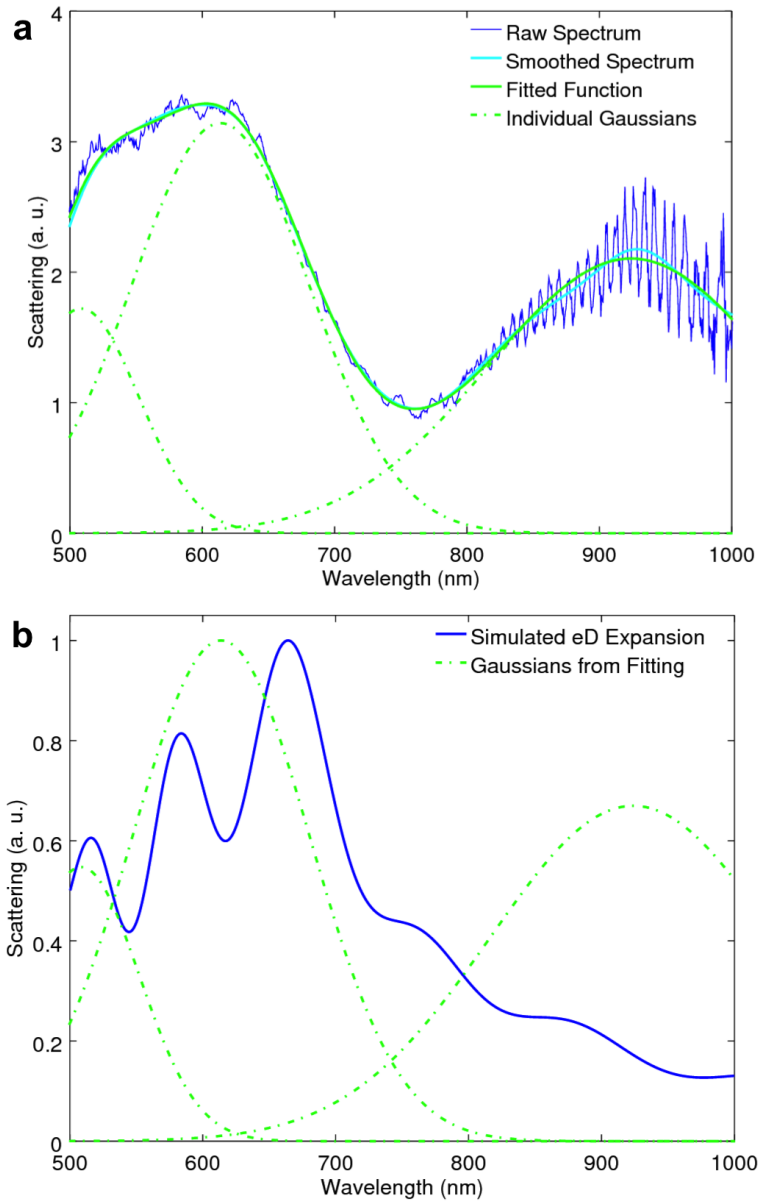

Figure 2.9: (a) Experimental scattering spectrum of linear beam of 165 nm core-satellite nano-cluster with fit to sum of Gaussians function. The dashed green lines show the individual Gaussian curves that are summed together to form the function for the fitting. (b) Comparison of the individual Gaussian curves from the fit to the experimental linear scattering spectrum to the electric dipole expansion of the simulated linear scattering spectrum.

2.5 Procedure for Creating Sample Cells

Two 150 μm thick 22x22 mm square coverslips (Fisher Scientific No. 1.5 12-541B) separated by a reusable 130 μm thick silicone spacer creating a chamber that held a volume of

approximately 8 μL comprised the sample cell. The space was cut from a larger silicone sheet (Bioflexus SH-20001-010) to a 22x22 mm square and a hole in the center was made using a hole punch. The top coverslip of the sample cell was cleaned by plasma etching for 4 minutes, which created a slight negative charge on the surface. This charging of the surface electrostatically repels the silver nanoparticles (nanoComposix NanoXact AGPN150, 150 nm diameter, polyvinylpyrrolidone-capped), reducing the frequency of spontaneous deposition while not significantly reducing the ability to deposit the arrays by the radiation pressure of the trapping laser. Prior to the creating of the sample cell, this top coverslip was sparsely coated in quantum dots by drop-casting 10 μL of a 26.8 pM aqueous solution, diluted 200:1 from a 5.36 nM stock solution (Oceannanotech QBA580-04), which was allowed to dry for 24 hours in a vacuum dessicator.

A solution of 150 nm diameter silver nanoparticles was prepared by diluting the stock 2 mM solution 200 times to a final concentration of 10 μM with 18 MΩ de-ionized water. Once the coverslip carrying the drop-cast quantum dots had completely dried and was removed from the dessicator, the dilute solution of silver nanoparticles was placed in a sonicator (Cole-Palmer 8890) for up to 5 minutes to re-disperse the nanoparticles that may have sedimented on the bottom of the container during storage and to break up aggregates. During the sonication, the silicone spacer was carefully lowered onto the coverslip holding the quantum dots with a pair of tweezers such that the hole in the spacer was centered on the coverslip and the square edges of both the spacer and the coverslip were aligned. The silver nanoparticles were removed from the sonicator and a 7-10 μL aliquot of the solution was placed onto the coverslip in the hole of the spacer. The cell was completed by taking a second coverslip and lowering it by holding one side in a gloved hand by the corners and bringing the opposite side down to an edge of the coverslip with the spacer already on top of it. Once this edge was secured against the spacer, the opposite edge was lowered to lie flat against the spacer to reduce the probability of creating an air bubble inside the sample cell. The completed

sample cell was inverted before being secured to a sample holder by two small metal tabs held in place by thumbscrews.

A similar procedure was repeated for the samples used in the cotrapping experiments. As the objective lens for the second trapping setup had a shorter working distance and the sample holder for the microscope stage was designed for rectangular sample cells, the bottom coverslip of the sample cell was replaced with a 100 μm thick 30x22 mm recangular coverslip (Fisher Scientific No 1.0 12-545A) and the spacer was replaced with a 130 μL thick disposable spacer with an interior volume of $\sim$17 μL with adhesive coating on both sides. The 150 μm thickness of the top coverslip was retained but the size was increased to 30x22 mm (Fisher Scientific No 1.5 12-544A) to match the bottom coverslip. The plasma etching time for the top coverslip was reduced to 1 minute since the sample is used immediately after creation as drop-casting quantum dots and drying to adhere them to the surface was no longer necessary. After the top coverslip was cleaned, the protective layer on one side of the adhesive spacer was removed and placed by hand onto the coverslip before being smoothed down with the back side of a curved pair of tweezers to ensure that the spacer lay flat on the surface. The second protective layer was then removed, exposing the other adhesive side of the spacer. 3.0 μL of a 100 μM 100 nm diameter PVP-coated silver nanoparticle solution diluted 20 times from a 2 mM stock (nanoComposix NanoXact AGPN100) was placed on the surface in the hole in the spacer along with 2.6 μL of a 40 pM quantum dot solution diluted 200 times from a 8 μM stock (Oceannanotech, QSH580). To reach the full volume encompassed by the spacer, 7.5 μL of 18 MΩ de-ionized water was added to the mixed quantum dot-silver nanoparticle solution on the top coverslip and another 7.5 μL was placed in the center of the bottom coverslip. The bottom coverslip was placed onto the top one edge at a time in the same manner as before, starting with one of the shorter edges. Since the charging caused by cleaning the top coverslip causes the solutions to spread out and wet the surface, the droplet on the bottom coverslip ensures that the solution is in contact with both surfaces as the

second coverslip was lowered, reducing the probability that an air bubble was introduced into the sample cell. The completed sample cell was inverted before being secured to the sample holder by small tabs of masking tape placed on the shorter edges of the coverslips and smoothing them down until they adhered to the sample holder.

2.6 Procedure for Depositing Nanoparticle Arrays

Following a similar procedure to [41] and [42], the deposition of silver nanoparticle arrays started with the marking of a 100 μm by 100 μm area on the top coverslip at the corners with a few nanoparticles for locating the arrays in later fluorescence lifetime measurements. Radiation pressure on the silver nanoparticles from the trapping beam overcomes the electrostatic repulsion between the nanoparticles and the substrate, fixing the nanoparticle on the surface at the trapping position. The positions of quantum dots inside this area were determined by turning off the bright-field illumination and scanning the excitation beam over the surface and observing the collected fluorescence in the array detector. Once the position of a quantum dot with no other dots in the immediate area ($\sim$3 μm radius) is determined, the excitation beam is blocked and the focal spot of the trapping beam is positioned over the dot. From here, the trapping beam is set to the designed location of each nanoparticle in the array and unblocked for a long enough duration to deposit the nanoparticle before moving on to the next location. The process was repeated for all of the isolated quantum dots found inside the designated region, creating an average of one to two dozen arrays per region.

2.7 Measuring Lifetimes from TCSPC Fluorescence Decay Curves

In order to obtain lifetimes from the fluorescence decay curves measured by TCSPC, the curves were fit to a two-exponential function convolved with the instrument response function (IRF) for the measurement setup. For all the experiments described in this dissertation, the IRF was measured from attenuating the excitation light source by a neutral density

filter, scattering the beam off of a sample cell containing no nanoparticles, and removing the bandpass filters that would block the excitation light from the standard measurement configuration. Figure 2.10 shows both an example of a fluorescence decay curve from a quantum dot in a deposited array using the setup described in Section 2.2 and the IRF determined for this configuration.

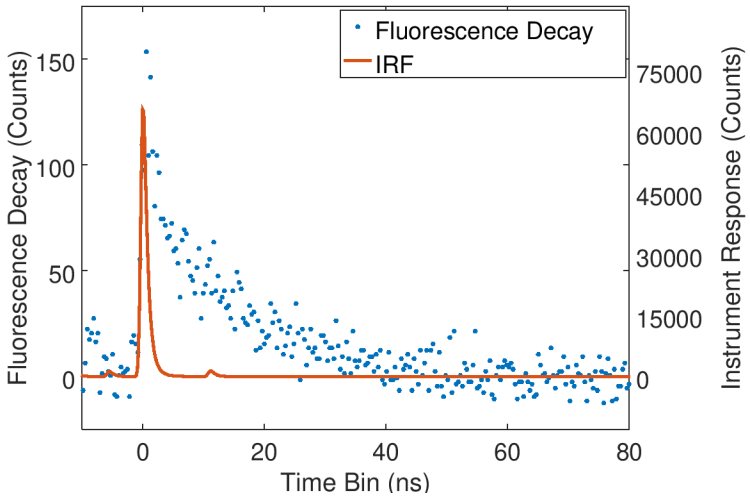

Figure 2.10: Fluorescence decay curve for a quantum dot in a deposited array structure (blue points) and instrument response function (orange curve) for the measurement setup described in Section 2.10.

Before fitting, the baseline of the fluorescence decay curves were set to zero by subtracting the background counts from the TCSPC data set, defined as the mean of the counts in the data set before the IRF's peak ($t < 0$ ns). A two-exponential function was chosen for the fitting as the CdSe/ZnS core-shell quantum dots used in the experiments should have two decay components evident in within the repetition rate of the excitation beam used [47],

$$g(t; a, k_1, b, k_2) = \mathrm{IRF}(t) * (ae^{k_1 t} + be^{k_2 t}) \tag{2.7}$$

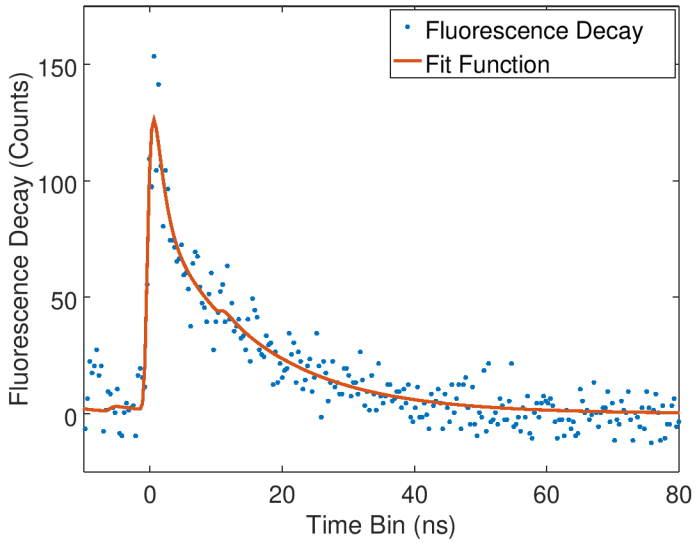

Figure 2.11: Fluorescence decay curve for a quantum dot in a deposited array structure (blue points) and fit of the two-exponential model convolved with the IRF (orange curve).

	a	$-\frac{1}{k_1}$ (ns)	b	$-\frac{1}{k_2}$ (ns)
Initial	92.09	14.00	61.39	1.00
Final	74.81	14.55	59.73	1.1867

Table 2.1: Initial parameters estimated for the example fluorescence decay curve in Figure 2.10 to fit eq. (2.7) to the data, and final parameters determined by NLLS optimization to minimize the sum of squared residuals between the fit and the measured curve. The time components are reported as lifetimes for clarity, while the fitting was performed with the corresponding decay rates.

where k_1 and k_2 are the decay rates of the exponential components, corresponding to lifetimes $\tau_1 = -\frac{1}{k_1}$ and $\tau_2 = -\frac{1}{k_2}$, with amplitudes a and b, respectively. The values of the parameters a, k_1, b, and k_2 were determined by nonlinear least squares (NLLS) fitting. The initial value of the parameter for the slower of the time components was estimated by the amount of time between the maximum of fluorescence decay curve and the point where it had decayed to $1/e$ of its initial value, $\sim$14 ns for the curve shown in Figure 2.10, and given an amplitude a of $\sim$60% of the maximum of the fluorescence decay curve. The faster of the time components was given an initial value of approximately the minimum resolvable rate for the

detection system, defined by twice the full-width at half the maximum (FWHM) of the IRF, or ∼1 ns, and the amplituded was set at ∼40% of the maximum of the fluorescence decay curve. If, after the NLLS optimization of the parameters, the residuals of the fluorescence decay curve were biased away from zero within five time constants (from the longer of the fit lifetimes), the fitting was re-run after adjusting the initial parameters until the guess function visually approximated the fluorescence decay curve. Figure 2.11 shows the fit function for the fluorescence decay curve shown in Figure 2.11 and Table 2.1 shows the values of the guess parameters and the fit parameters determined from the NLLS optimization.

2.8 Finite-Difference Time Domain (FDTD) Simulations

Finite-Difference Time Domain (FDTD) simulations were conducted using the software packages MEEP[48] and Lumerical FDTD Solutions 8.18. The dieletric function of the silver nanoparticles (AgNPs) used in MEEP was a two-term Drude-Lorentz model fit to the the dielectric function measured by Johnson and Christy[49] of the form

$$\varepsilon(\omega, \boldsymbol{r}) = (1 + \frac{i\sigma_D(\boldsymbol{r})}{\omega}) \left[\varepsilon_{\text{inf}}(\boldsymbol{r}) + \sum_n \frac{\sigma_n(\boldsymbol{r})\omega_n^2}{\omega_n^2 - \omega^2 - i\omega\gamma_n} \right] \tag{2.8}$$

where σ_D is the electric conductivity, $\sigma_n(\boldsymbol{r})$ is the position-dependent strength of the nth term, $f_n = \omega_n/2\pi$ is the resonance frequency of the term, and $\gamma_n/2\pi$ is the damping of the term. The values of these terms used for silver in our simulations are shown in Table 2.2. The dielectric function used in Lumerical FDTD Solutions came from the materials library included in the software.

n	$\sigma_n(\boldsymbol{r})$	$f_n = \omega_n/2\pi$	$\gamma_n/2\pi$
1	5.38081×10^{41}	1×10^{-20}	0.0100112
2	1.99513	4.07823	0.443329

Table 2.2: Parameters determined for the Drude-Lorentz model fit to the Johnson and Christy dielectric function of silver to be used in FDTD simulations. The value of ε_{inf} in eq. (2.8) used was 1.0001. All values are given in the units used by the MEEP simulations.

2.8.1 FDTD Simulations of 1D AgNP Lattices for Dark-field Spectroscopy

For the simulations discussed in Chapter 3, the 1D lattices of AgNPs were placed on glass substrates were illuminated by a linearly polarized plane wave with λ = 400-950 nm with the polarization direction along x- (parallel polarization) and z-directions (perpendicular polarization). A non-uniform mesh with maximum grid size of 1 nm was used to calculate the spectra. The background index for the surrounding medium was set to that of water (n = 1.33). For the far field scattering patterns of point-dipole sources, the source and the lattices were placed in a uniform medium (n = 1.5) with a grid size of 2 nm. The calculated fields were propagated to a surface 1.8 mm from the source to match the focal distance of the objective, limited by an angle commensurate with the numerical aperture of the lens (NA = 1.4).

2.8.2 FDTD Simulations of a Point-Dipole Source in 1D AgNP Lattices

For the simulations discussed in Chapter 4, the source was a point-dipole located at the center of the simulation domain with a center wavelength in vacuum of λ = 580 nm and a bandwidth covering the visible region, $\lambda \approx$ 400-900 nm. The background dielectric was set to have an index of refraction equivalent to that of water (n = 1.33). The grid was set to a resolution of 2 nm. The local density of states was calculated as the power radiated by the dipole into the simulation domain at the location of the source, calculated in MEEP as

$$\text{LDOS}_l(\boldsymbol{r},\omega) = -\frac{2}{\pi}\varepsilon(\boldsymbol{r})\frac{\text{Re}\left[\hat{E}_l(\boldsymbol{r},\omega)\hat{p}(\omega)^*\right]}{|\hat{p}(\omega)|^2} \tag{2.9}$$

where $\boldsymbol{r}$ is the position where the LDOS is calculated, $\hat{E}_l(\boldsymbol{r}, \omega)$ is the frequency-domain representation of the time-averaged electric field in the polarization direction l of the dipole source calculated from the simulation at the position $\boldsymbol{r}$, and $\hat{p}(\omega)$ is the time-averaged power radiated into the simulation domain in the frequency-domain representation.

2.8.3 FDTD Simulations of Near-field AgNP Chains and Core-Satellite Nanostructures

For the simulations of chains of AgNPs discussed in Chapter 5, 2-4 nanoparticles with a diameter of 40 nm were illuminated with a plane-wave source with a wavlength range λ = 600-1000 nm. Only longitudial surface plasmon resonance was calculated by setting the excitation polarization along the axis of the chains. A nonuniform mesh was used with a grid size of 1.0-0.4 nm in order to have sufficient resolution for the sub-nanometer gaps between the particles in the near-field.

The core-satellite nanostructures were illuminated with sources having a wavelength range of λ = 500-1000 nm and the monitor for calculating the scattering spectra was a spherical shell placed around the structure, as opposed to the rectangular box typically used in FDTD simulations. The azimuthal and radial beam sources were created by determining the current densities that give rise to electric fields with azimuthal and radial polarization as solutions to Maxwell's equations.

2.9 Generalized Mie Theory (GMT) Simulations

The electrodynamic interactions of the AgNP arrays in Chapter 4 are computed with the GMT method [50, 51] using the software package MiePy, a GMT code developed by John Parker (not yet published). In this method, the incident and scattered fields are expanded into the vector spherical harmonic (VSH) wave functions around each particle to match the surface boundary conditions. The incident source field on particle j is expanded into the

regular VSH's $\boldsymbol{N}_{mn}^{(1)}$ (electric) and $\boldsymbol{M}_{mn}^{(1)}$ (magnetic),

$$\boldsymbol{E}_{\text{inc}}^{j} = -\sum_{n=1}^{L_{\max}} \sum_{m=-n}^{n} iE_{mn} \left[p_{mn}^{(j\to j)} \boldsymbol{N}_{mn}^{(1)} + q_{mn}^{(j\to j)} \boldsymbol{M}_{mn}^{(1)} \right] \tag{2.10}$$

where $L_{\max}$ is the maximum number of multipole orders to expand in, E_{mn} is a normalization constant, and $p_{mn}^{(j\to j)}$ and $q_{mn}^{(j\to j)}$ are the expansion coefficients of the incident source at particle j. The scattered field of particle j is similarly expanded into the scattering VSH's $\boldsymbol{N}_{mn}^{(3)}$ and $\boldsymbol{M}_{mn}^{(3)}$,

$$\boldsymbol{E}_{\text{scat}}^{j} = \sum_{n=1}^{L_{\max}} \sum_{m=-n}^{n} iE_{mn} \left[a_n^j p_{mn}^j \boldsymbol{N}_{mn}^{(3)} + b_n^j q_{mn}^j \boldsymbol{M}_{mn}^{(3)} \right] \tag{2.11}$$

where a_n^j and b_n^j are the ordinary Mie coefficients [7] of particle j and p_{mn}^j and q_{mn}^j are the expansion coefficients of the light incident on particle j.

The expansion coefficients p_{mn}^j and q_{mn}^j are solved for in a system of $2NL_{\max}(L_{\max}+2)$ interaction equations

$$\begin{aligned} p_{mn}^j &= p_{mn}^{(j\to j)} - \sum_{l\neq j}^{(1,N)} \sum_{v=1}^{L_{\max}} \sum_{u=-v}^{v} A_{mn}^{uv}(l\to j) a_v^l p_{uv}^l + B_{mn}^{uv}(l\to j) b_v^l q_{uv}^l \\ q_{mn}^j &= q_{mn}^{(j\to j)} - \sum_{l\neq j}^{(1,N)} \sum_{v=1}^{L_{\max}} \sum_{u=-v}^{v} B_{mn}^{uv}(l\to j) a_v^l p_{uv}^l + A_{mn}^{uv}(l\to j) b_v^l q_{uv}^l \end{aligned} \tag{2.12}$$

where $A_{mn}^{uv}(l\to j)$ and $B_{mn}^{uv}(l\to j)$ are the VSH translation coefficients from particle l to particle j.

An electric point dipole excitation with a fixed polarization is used to model the quantum dot source. The decomposition of this excitation into VSH functions is straightforward since the fields produced by an electric dipole are guaranteed to be a linear combination of the $\boldsymbol{N}_{1m}^{(3)}$ functions. Assuming the quatum dot is at position $\boldsymbol{r}_{\text{dot}}$, the decomposition of the excitation fields at particle position $\boldsymbol{r}_j$ is given by a linear combination of the VSH translation

coefficients from $\boldsymbol{r}_{\text{dot}}$ to particle j

$$\begin{aligned} p_{mn}^{(j\to j)} &= \delta_{n1} \sum_{u=-1}^{1} w_u A_{u1}^{m1}(\boldsymbol{r}_{\text{dot}} \to j) \\ q_{mn}^{(j\to j)} &= \delta_{n1} \sum_{u=-1}^{1} w_u B_{u1}^{m1}(\boldsymbol{r}_{\text{dot}} \to j) \end{aligned} \tag{2.13}$$

where δ_{n1} is the Kronecker delta function and w_u are polarization dependent weight factors. Given a dipole orientation $\boldsymbol{s} = (s_x, s_y, s_z)$ with magnitude $|\boldsymbol{s}|$, the weight factors are $w_{-1} = (is_x - s_y)/2$, $w_0 = -is_z$, and $w_1 = (-is_x - s_y)/2$. Given the positions of the nanoparticles and the quantum dot source, eq. (2.12) can then be solved for the expansion coefficients.

The local density of states is computed using the same equation as used in the FDTD method. [52] Since GMT is a frequency-domain method, the frequency dependent dipole term can readily be set to unity, $\hat{p}(\omega) = 1$, and the LDOS equation simplifies to

$$\text{LDOS}_l(\boldsymbol{r}_{\text{dot}}, \omega) = -\frac{2}{\pi}\varepsilon(\boldsymbol{r}_{\text{dot}})\text{Re}\left[E_l(\boldsymbol{r}_{\text{dot}}, \omega)\right] \tag{2.14}$$

LDOS enhancement is obtained by normalizing the LDOS with the NP array by the LDOS without the NP array.

CHAPTER 3

MESO-SCALE DIPOLAR INTERACTIONS IN PHOTONICALLY SYNTHESIZED METAL NANOPARTICLE LATTICES

Reproduced in part with permission from: Uttam Manna, Nolan M. Shepherd, Zijie Yan, Ying Bao, Justin E. Jureller, and Norbert F. Scherer. Meso-scale dipolar interaction in photonically synthesized metal nanoparticle lattices. Manuscript in preparation.

3.1 Introduction

Plasmonic excitations in nanoparticles provide a means for manipulating light-matter interactions beyond the diffraction limit. This property is being developed into applications such as miniaturized optical[53] and electronic[54, 55] devices, surface enhanced Raman scattering (SERS) and localized surface plasmon resonance (LSPR) based chemical and biological sensing[56, 57], and medical diagnostics and therapeutics[58, 59]. Moreover, assembly of metal nanoparticles in arrays has emerged as a promising platform for tunable electrical, optical, and sensor applications[54, 56, 57, 60, 61].

Both templated and template-free assembly methods have been used extensively to create well-defined one dimensional (1D)[62], 2D and 3D[63, 64] nanoparticle array architectures. The range of materials and structures that could be created would expand if other driving forces, such as interactions between gradients of external fields and nanomaterial interactions could be harnessed[65, 66, 67, 68, 69, 70]. One new approach, photonic synthesis[71, 72, 73, 74, 40, 75], allows creating defined spatial configuration of nanoparticles, including creation of ordered lattices of nanoparticles.

When light is incident on polarizable particles, the incident field and light scattered from the particles interfere, leading to spatial gradients and new optical forces on the particles. This

interaction, termed optical binding[71], emerges from the expansion of dipolar interactions on the scales of the wavelength of light. The optical binding interaction can be used as a driving force to control small objects on meso-scales with nanoscale precision to *photonically synthesize* defined configurations of metal nanoparticles[72, 73, 74, 40, 75].

In 'optical binding', interparticle forces produced by light scattering and interference between multiple particles leads to defined spatial configurations of particles[71, 72, 73]. Optical binding interactions occur on intermediate scales (where particle separation, Δx is approximately equal to wavelength of the incident light, λ) between the near-field ($\Delta x \ll \lambda$) and far-field ($\Delta x \gg \lambda$) limits. The optical binding interactions can be significant when the particles are typically separated by distances that are integral multiples of the wavelength of the incident light in the host medium. Here, Δx denotes the center-to-center separation between the particles.

Recently, our group demonstrated that the optical binding of Ag nanoparticles enables controlled formation of 1D and 2D nanoparticle arrays or synthetic photonic lattices[73] as well as hybrid assemblies of Ag nanoparticles and semiconductor quantum dots in solution[40]. Subsequently, these 1D and 2D synthetic photonic lattices, defined by optical binding and minimally shaped trapping beams, can be deposited onto glass substrates by *optical printing* performed by controlling the electrostatic interactions of the surface functionalized nanoparticles and substrates[76]. These 1D and 2D lattices are characterized by wave-vectors on the μm^{-1} scale.

For nanoparticle arrays with interparticle separations exceeding the near-field limit, the intermediate scale and far-field interactions are mediated by the scattered dipolar fields. In these regimes, the scattered dipolar fields interfere to form collective radiation[15, 13, 77]. Hence, it should be possible to tune the plasmonic properties of arrays of noble metal nanoparticles by exploiting dipolar interactions at the intermediate-scale regime by controlling the separation between the particles forming the array as well as create other photonic

architectures from nanophotonic constituents[78].

Tuning the plasmonic properties of metal nanoparticles presents the opportunity to create nanoscale optical devices by placing an emitter in the array. Quantum dots placed in near-field proximity to plasmonic nanoparticles are known to gain an enhancement to their radiative rate when the resonance of the nanoparticles is close to wavelength of the quantum dots' fluorescence[79, 80, 81], but this coupling drops quickly as the distance between the dot and the particle increases[80]. However, the fluorescence of quantum dots couples to their surroundings via the transition dipole moment between the excited and ground states; this should extend the interaction to the intermediate scale if the quantum dot is placed in a structure designed to couple with scattered dipolar fields. It is expected then that the collective resonance of a 1D lattice structure can couple to this transition dipole and exhibit an effect on the fluorescence lifetime of quantum dots placed in the structure.

We report the results of scattering spectroscopy measurements conducted on 1D synthetic photonic lattices of Ag nanoparticles (diameter, $d \approx 150$ - 200 nm) formed by combining optical trapping and optical binding on substrates, an approach we have termed optical printing[76]. In combination with electrodynamic simulations, we demonstrate that for 1D lattices consisting of only a few (two to six) Ag nanoparticles, the dipolar fields of the individual Ag nanoparticles electrodynamically couple in the intermediate-scale regime. For particle separation smaller than the plasmon resonance of the individual particles ($\Delta x < \lambda_{res}$), the dipolar fields are found to add up in-phase (*i.e.*, constructively interfere) resulting in a red-shift of the collective plasmon resonance of the 1D lattice. By contrast, for $\Delta x > \lambda_{res}$, the dipolar fields are out-of-phase resulting in a blue-shift of the collective plasmon resonance of the 1D lattice. We find that the magnitude of the spectral shift for the intermediate-scale coupling in these 1D lattices is comparable to that for near-field coupling. Moreover, we also find that the spatial coherence properties of the incident light used to measure the spectroscopic response of the 1D array is a critical aspect of the intermediate scale coupling.

In addition, we demonstrate the use of 1D lattice structures to enhance the radiative rate of cadmium selenide/zinc sulfide core-shell quantum dots and shape the far field radiation pattern of the emitted fluorescence.

3.2 Results and Discussion

The 1D synthetic photonic lattices of Ag nanoparticles we study were created by optical printing[76] using the optical tweezers apparatus illustrated in Figure 3.1a. The optics used to shape the trapping beam are depicted in Figure 2.1, and a detailed description is also given in References [75, 76]. The 1D lattices were allowed to form in solution using a line trap and subsequently the whole lattice was deposited on the glass substrate. Note that the separation between the individual particles occurs at integral multiples of the trapping laser wavelength in the host medium, which is ∼600 nm in our case (*i.e.* 800 nm vacuum wavelength / n, where $n = 1.33$ for water). For spectral measurements of the 1D lattices with interparticle separations greater than the optical binding length-scale, the particles were trapped individually and subsequently deposited in the desired locations by moving the piezoelectric stage holding the sample cell[76, 82]. In this way, many different 1D lattices were created with different numbers of particles and separations between the particles.

Figure 3.1a and c show the laboratory-frame geometry corresponding to the dark-field spectral measurement for incident light polarized parallel and perpendicular to the lattice-axis. The axis of the 1D photonic lattice is along the x-direction. Owing to the dark-field nature of the experimental geometry, the major components of the incident wave-vector lie within the xy sample plane. In this configuration, the incident white light was masked with a slit in the aperture plane so that only the y-component of the wave-vector is allowed to be incident on the sample. The scattered light from the 1D lattice was collected along the negative z-direction for all the angles corresponding to the NA (≈ 1.2) of the 60x immersion objective. The spectral measurements were performed with the polarization of the incident white light

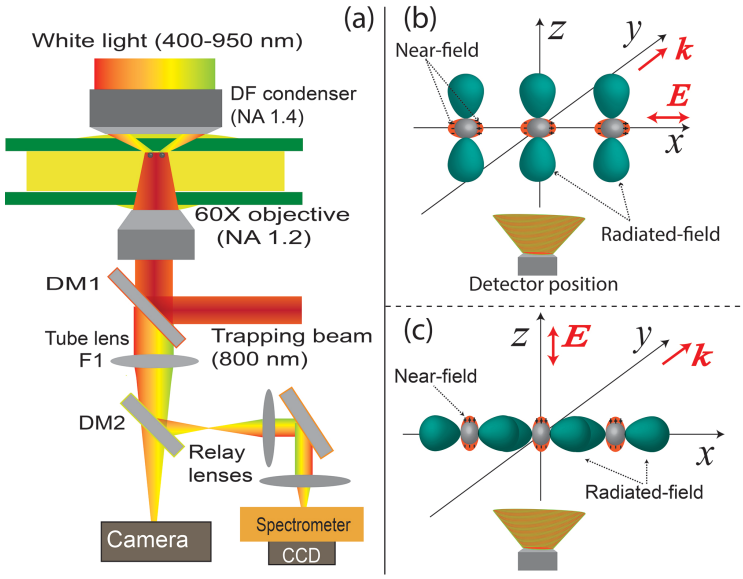

Figure 3.1: (a) The optical tweezers set-up used to optically trap, bind and print Ag nanoparticles to create 1D synthetic photonic lattices. DM, NA, DF, F are abbreviations of Dichroic Mirror, Numerical Aperture, Dark-field, and Filter, respectively. (b-c) The laboratory-frame geometry corresponding to the dark-field spectral measurement. The spectral measurements were performed for polarization along the (i) x-direction (termed parallel polarization) (b); and (ii) z-direction (termed perpendicular polarization) (c). (b) and (c) also show the schematic representations of the near-fields (red) and the radiative fields (olive-green) of the nanoparticles for parallel and perpendicular polarizations, respectively.

.

in two directions: (i) along the x-direction (Figure 3.1a, termed parallel polarization); and (ii) along the z-direction (Figure 3.1c, termed perpendicular polarization). Figure 3.1b and c also show the schematic representations of the directions of the near-fields (shown in red) and the radiative fields (shown in olive-green) of the nanoparticles for parallel and perpendicular polarizations, respectively. Finite-difference time-domain (FDTD) electrodynamic simulations were performed to complement the experimental results. The simulation geometry was similar to that of the experiment; the lattice axis and incident wave-vector were aligned along the x-, and y-axes, respectively.

3.2.1 Spectral dependence on interparticle separation

Ag nanoparticles exhibit pronounced Mie resonances[83, 84, 85]; for diameter $d > 100$ nm two broad Mie resonance peaks are visible in the scattering spectra[83]. The longer wavelength peak is due to the dipole excitation (dipolar plasmon resonance), whereas the shorter wavelength peak is a multi-pole excitation. Figure 3.2 a-d and Figure 3.2 e-h show the experimental and simulated scattering spectra of 1D lattices consisting of five Ag nanoparticles (N=5) with $d \approx 160$ nm, respectively as a function of interparticle separation for two different directions of the incident light polarization. The dark-field images of the 1D lattices consisting of five Ag nanoparticles with separations, $\Delta x \approx$570, 690, 750, and 1200 nm are shown in the inset panels of Figure 3.2 a-d, respectively.

As shown in Figure 3.2 a and e, for particle separation at the optical binding distance ($\Delta x \approx 570$ nm in this case), we find that the dipolar peak position is red-shifted for incident light polarized perpendicular to the lattice axis. This is opposite to what is expected for near-field interactions[86, 87, 83], as will be discussed further in Subsection 3.2.7. We also found that for particle separation exceeding the optical binding distance, $\Delta x \approx 690$ nm (Figure 3.2b and f) and 750 nm (Figure 3.2c and g), the dipolar peaks are blue-shifted for polarization perpendicular to the lattice axis. For $\Delta x \approx 1200$ nm, the dipolar peak position is weakly dependent on the incident polarization.

Figure 3.2i shows the calculated dipolar peak positions of the 1D lattice (N=5 and $d = 160$ nm) as a function of separation for both polarizations. As shown in Figure 3.2i, the dipolar peak positions show a strongly non-monotonic behavior as a function of interparticle separation for both polarizations. Figure 3.2j shows the magnitude of the spectral-shift for perpendicular polarization with respect to parallel polarization as a function of separation as deduced from experiments and simulation. Our simulation results are consistent with those from the Schatz group[11, 88].

As shown in Figure 3.2j, our experimental and simulation results suggest that for $\Delta x < \lambda_{res}$,

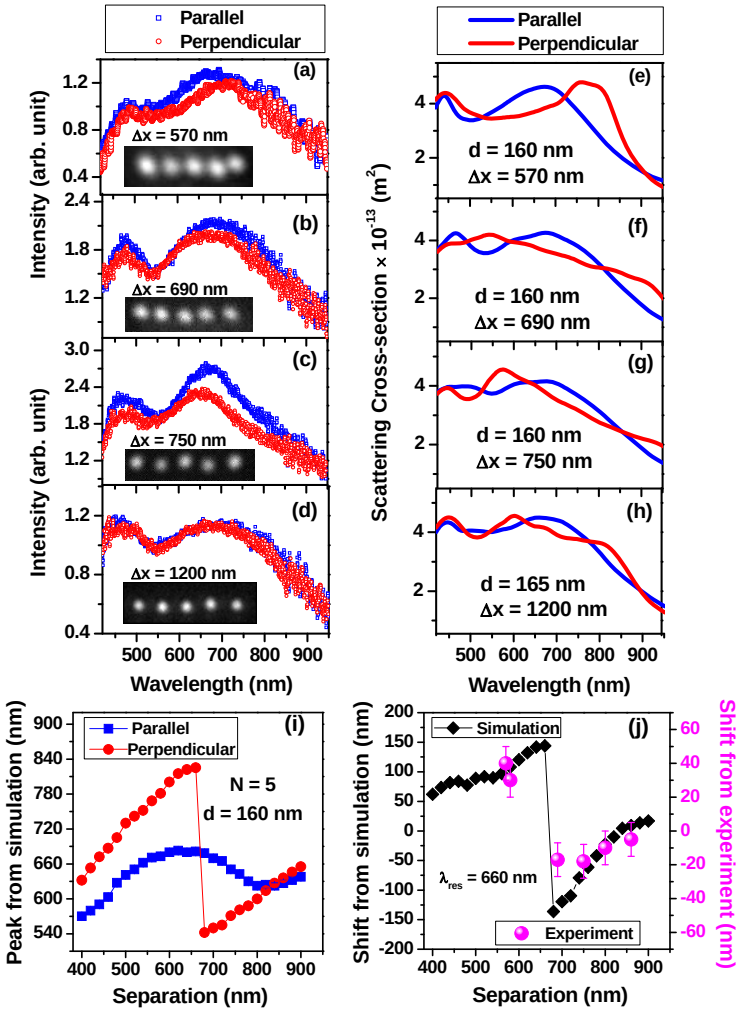

Figure 3.2: Experimental (a-d) and simulated (e-h) scattering spectra for parallel and perpendicular polarizations as a function of interparticle separation. The inset panels in (a-d) show the dark-field scattering image of the 1D lattices measured with separations $\Delta x \approx$570, 690, 750, and 1200 nm, respectively. For $\Delta x \approx 570$ (a and e), the dipolar peak is red-shifted; whereas for $\Delta x \approx 690$ nm (b and f), and 750 nm (c and g), the dipolar peaks are blue-shifted for perpendicular polarization of the incident light (N=5 and $d \approx 160$ nm). (i) shows the calculated dipolar peak positions as a function of interparticle separation for both polarizations. The magnitude of the spectral shifts for perpendicular polarization with respect to parallel polarization are plotted in (j) as deduced from both experiments and simulation as a function of separation ($\Delta x = 400$ to 900 nm for N=5 and $d \approx 160$ nm). Note the different scales for the results from experiment (pink) and simulation (black).

the collective plasmon resonance of the 1D lattice is red-shifted; whereas for $\Delta x > \lambda_{res}$ the collective plasmon resonance of the 1D lattice is blue-shifted. Here, λ_{res} is the dipolar plasmon resonance of an individual nanoparticles, calculated to be 660 nm for Ag nanoparticles with $d = 160$ nm. The dipolar plasmon resonance of the individual particles, λ_{res}, plays an important role in determining the collective dipolar plasmon resonance of the 1D lattice. This is further discussed in Subsection 3.2.3.

The trend of the experimental spectral-shift as a function of interparticle separation agrees well with the calculation. However, the magnitude of the calculated spectral-shift is approximately three to four times greater than that of the experiment. We attribute this discrepancy to the 'short' spatial coherence length of the incoherent incident white light used in these experiments. The role of spatial coherence property of the incident light in our experiments is discussed is detail in Subsection 3.2.4. Also, the experimental scattering intensities for perpendicular polarization of the incident light are found to decrease compared to that of parallel polarization. This is in contrast to the calculation. We attribute this discrepancy to the dark-field nature of our experiment. The influence of experimental conditions on scattering spectra is discussed in detail in Subsection 3.2.4.

3.2.2 Spectral dependence on particle number

Figure 3.3 a-c and Figure 3.3 d-f show the experimental and simulated scattering spectra of 1D lattices, respectively for different number of particles in the array. Specifically, we show results for one, three and six Ag nanoparticles with diameter, $d \approx 180$ to 200 nm for two different directions of the polarization. In this case, the interparticle separation is fixed at the optical binding length scale ($\Delta x \approx 600$ nm). The dark-field images of the 1D lattices consisting of one, three and six particles are shown in the inset panels of Figure 3.3 a-c, respectively.

From our experimental and simulated spectra, we find that for interparticle separation at

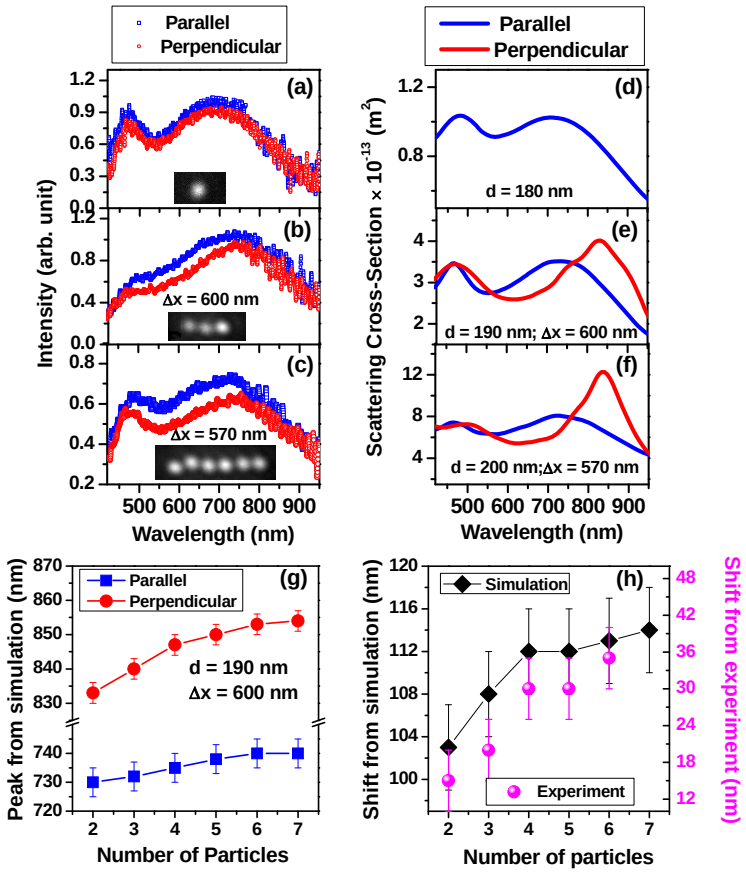

Figure 3.3: Experimental (a-c) and simulated (d-f) scattering spectra for parallel and perpendicular polarizations as a function of number of particles. The inset panels in (a-c) show the dark-field scattering image of the 1D lattices consisting of one, three, and six particles, respectively. The magnitude of the spectral-shift is found to depend on the number of particles forming the lattice. The single particle spectra are presented as a control experiment and simulation. (g) shows the calculated dipolar peak positions as a function of number of particles for both polarizations. The magnitude of the spectral shifts are plotted in (h) as deduced from both experiments and simulation as a function of number of particles (N=1 to 7 with $d \approx 190$ nm and $\Delta x \approx 600$ nm).

the optical binding length-scale ($\Delta x \approx 600$ nm), the magnitude of the red-shift is strongly dependent on the number of particles forming the 1D lattice. Figure 3.3g shows the calculated dipolar peak positions of a 1D lattice as a function of the number of particles (N=1 to 7) with $d = 190$ nm and $\Delta x = 600$ nm for both polarizations. We find that as the number of particles forming the 1D lattice increases, the dipolar peak positions for both polarizations

are increasingly red-shifted; the magnitude of the red-shift is greater for perpendicular polarization. Figure 3.3h shows the magnitude of the red-shift for perpendicular polarization as deduced from experiments and simulation as a function of number of particles forming the lattices. The experimental and simulation results suggest that the magnitude of the red-shift initially increases linearly up to four particles in the lattice and then saturates. Again, the trend of the experimental spectral-shift as a function of number of particles agrees well with the calculation. However, we note the discrepancy in the magnitude of the spectral shift and scattering intensities, which is discussed in Subsection 3.2.4.

3.2.3 Dipolar interactions for intermediate-scale separation

For nanoparticle arrays with interparticle separation at the intermediate-scale ($\Delta x \approx \lambda$), the electrodynamic interactions are mediated by the interference of the scattered dipolar fields concentrated in the equatorial plane of the lattice-axis (schematics shown in Figure 3.1b and c). The interactions of scattered radiative fields in the intermediate-scale and far-field regime were studied theoretically by Meier, Wokaun, and Liao[15] for a 2D square array of Ag nanoparticles. The central result of their study is the determination of an effective depolarization constant, $A_{eff,j}$, that determines the plasmon resonance of the array along an axis j. The depolarization constant, $A_{eff,j}$ can be written as

$$\mathrm{Re}[A_{eff,j}] = A_j^{static} - (q^2/3 + q^4/24 + q^6/864 + \ldots) + \mathrm{Re}[C_j]V/\Delta x^3 \tag{3.1}$$

$$\mathrm{Im}[A_{eff,j}] = \mathrm{Im}[C_j]V/\Delta x^3 \tag{3.2}$$

where $q = k(3V/4\pi)^{1/3}$ and k is the magnitude of the wave-vector[15, 14]. The first and second terms of the real part of $A_{eff,j}$, the static and dynamic depolarization, depend on the particle eccentricity and finite size of the individual particles, respectively. The particle interactions in the array that cause resonance shifts are contained in the term $\mathrm{Re}[C_j]V/\Delta x^3$,

where V is the particle volume, Δx is the lattice constant, and C_j is the dipolar-interaction constant. Note that we are using the same Δx notations in eq. (3.1) and eq. (3.2) as in our results. The imaginary part of $A_{eff,j}$ expresses the damping of the near-field by the collective radiation of the entire particle array.

For $\Delta x \leq \lambda_{res}$, the light fields corresponding to a grating order are evanescent in character. However, the local optical fields in the plane of the array become large due to an almost in-phase addition of the scattered light fields of neighboring particles[15]. This results in strongly negative values of $\mathrm{Re}(C_j)$ leading to a red-shift of the plasmon resonance wavelength[15, 13]. At $\Delta x = \lambda_{res}$ the grating order becomes radiative at a grazing angle. The appearance of a new radiating grating order leads to a sudden increase of the total power radiated by the array with the value of $\mathrm{Im}(C_j) \to -\infty$. For $\Delta x \geq \lambda_{res}$, $\mathrm{Im}(C_j)$ takes on large negative values due to the grating order being close to the grazing angle.

The above discussed meso-scale interactions was found to influence the lifetime and collective plasmon resonance of 2D 'infinite' square array of metal nanoparticles[13, 89]. It was also shown by simulation that significant far-field coupling exists between a pair of Au nanoparticles over distances many times the particle diameter with the coupled particle-plasmon mode alternating between 'superradiant' and 'subradiant' behavior when the particle spacing is varied[90].

To understand the spectral properties of our 1D lattices as a function of polarization, interparticle separation, and number of particles, we adopt the theory of electrodynamic coupling of scattered radiative fields of 2D square arrays[15, 14]. For particle separation at the optical binding length scale, the interparticle separation is smaller than the plasmon resonance of the individual particles (λ_{res} = 660 nm for d = 160 nm; 730 nm for d = 190 nm). Hence, an in-phase addition of the scattered light fields is expected to red-shift the collective plasmon resonance of the 1D lattices (Figure 3.2j). Moreover, for perpendicular polarization, the radiative fields of the individual particles are aligned along the array axis

(Figure 3.1c), which is expected to lead to a significantly larger red-shift compared to that for parallel polarization (Figure 3.2i).

To verify the behavior of the optical fields in the plane of the array as a function of separation, we have simulated the 3D electric field distributions for a 1D lattice consisting of five nanoparticles with $d = 160$ nm for both polarizations as shown in Figure 3.4. For $\Delta x \leq \lambda_{res}$ ($\Delta x = 570$ nm), the scattered fields are found to add up in-phase leading to 'hot spots' between the particles (Figure 3.4b) for perpendicular polarization. Furthermore, as the number of particles forming the 1D lattice increases, the magnitude of the field increases (additively) leading to a larger red-shift of the dipolar peak position for both the polarizations (Figure 3.3h).

For $\Delta x > \lambda_{res}$ (for example, $\Delta x = 750$ nm), we find that the radiative fields for perpendicular polarization are out-of-phase as shown by the electric field distributions of the 1D lattice in Figure 3.4d. This out-of-phase interaction results in a blue-shift of the dipolar peak position for perpendicular polarization compared to that for parallel polarization (Figure 3.2j).

3.2.4 Influence of experimental conditions on scattering spectra

In Subsections 3.2.1 and 3.2.2, we pointed out that even though the trends in the experimental spectral-shifts of the collective plasmon resonances of the 1D lattices as a function of separation and number of particles agree qualitatively with the calculated results, the calculated spectral-shifts are approximately three to four times greater than what we measured. We attribute this discrepancy to the short spatial coherence length of the incoherent white light used in our experiment. To substantiate this, we performed the spectral measurements of the 1D Ag nanoparticle lattices using a fiber laser continuum white light source for two different directions of the polarization.

Figure 3.5a shows the scattering spectra of a 1D lattice (N=3, $\Delta x = 600$ nm and $d \approx 160$

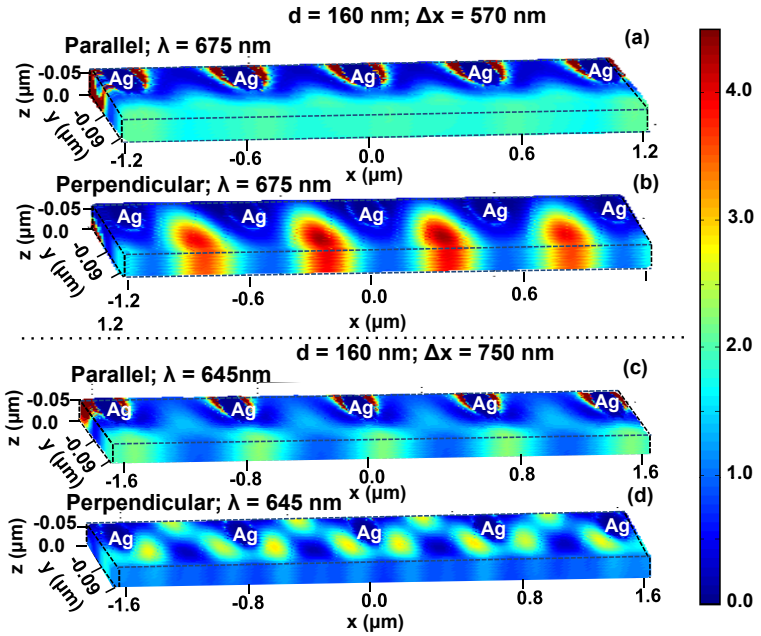

Figure 3.4: The 3D electric field distributions for 1D lattice consisting of five nanoparticles with $d = 160$ nm for $\Delta x = 570$ nm (a and b), and $\Delta x = 750$ nm (c and d) for parallel (a and c) and perpendicular polarization (b and d). The wavelengths ($\lambda = 675$ nm in (a and b) and 645 nm in (c and d)) are chosen to match the peak positions of the collective dipolar plasmon resonance of the relevant arrays for parallel polarization.

nm) obtained using coherent excitation. The results show that the dipolar radiation is only weakly detected for polarization parallel to the lattice axis; whereas the dipolar radiation could not be detected for polarization perpendicular to the lattice axis. Our experimental results using coherent excitation are supported by the FDTD calculation shown in Figure 3.5b. In this calculation, the scattered radiation from a 1D lattices was only collected in a cone along the z-axis corresponding to the NA of the objective. By contrast, the calculations in Figures 3.2 and 3.3 were performed by integrating the scattered light for all solid angles (4π stere radians). This indicates that the light is emitted outside the range of the NA collected in the experiment.

For coherent excitation, the light from a 1D lattice is expected to scatter only at defined angles, in analogy to light diffraction from a grating[77]. For $\Delta x = \lambda_{res}$, the scattered light

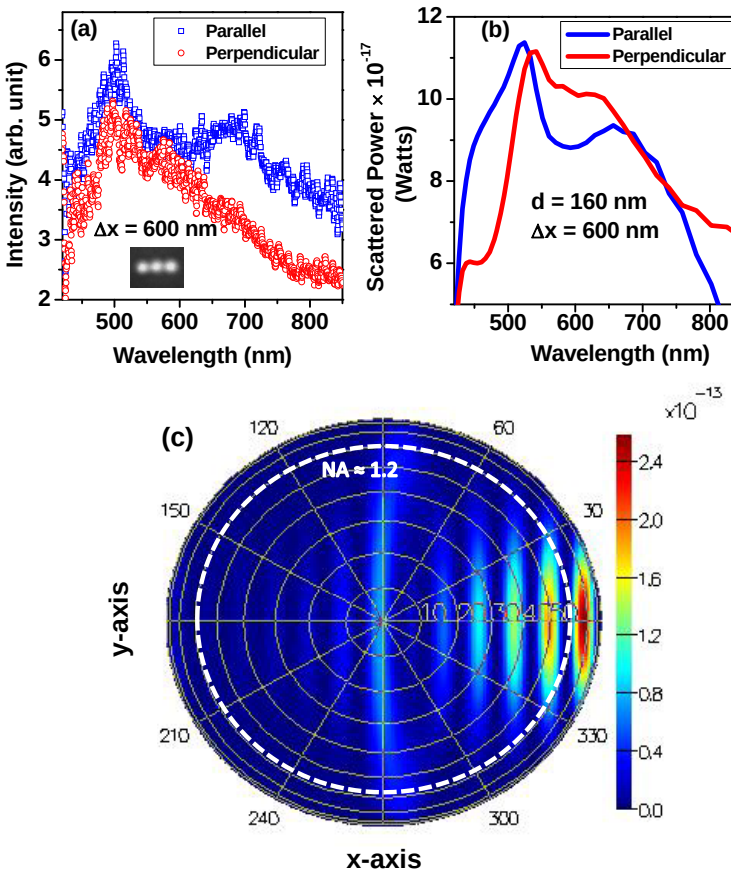

Figure 3.5: (a) Experimental dark-field scattering spectra for a 1D lattice measured using coherent excitation for the separation in the optical binding length-scale. (b) Calculated scattering spectra for the same 1D lattice with the scattered radiation integrated around a cone corresponding to the NA of the objective. (c) shows the angular distribution of the projection of the calculated far-field along z-direction for a 1D lattice (N=5, $\Delta x = 600$ nm and $d = 160$ nm) using coherent excitation with $\lambda = 650$ nm for parallel polarization. Note that the scattered power, P, is defined as $P = \sigma I$, where σ is the cross-section in m^2, and I is the source intensity in Watts/m^2.

corresponding to the first grating order is emitted parallel to the plane of the 1D lattice, *i.e.* in the xy plane. Moreover, in the dark-field configuration, the scattered dipolar radiation along the z-direction is only collected for the specific angular range defined by the NA of the microscope objective (≤ 1.2 for our case). Figure 3.5c shows the angular distribution of the projection of the calculated far-field along the z-direction for a 1D lattice (N=5, $\Delta x = 600$

nm and $d \approx 160$ nm) for coherent excitation with $\lambda = 650$ nm for parallel polarization. The coherent excitation was allowed to be incident on the sample with an angle corresponding to the NA of the dark-field condenser (NA≈1.2) to replicate the experimental condition. As shown in Figure 3.5c, the major component of the far-field projected emission along z-direction is found to lie outside the NA of of the microscope objective for parallel polarization. Therefore, the coherent scattered light is only weakly detected in our experiment.

For perpendicular polarization, the radiative fields of the individual particles are aligned along the lattice axis (schematics shown in Figure 3.1c). As a result, the scattered radiation for perpendicular polarization is expected to be 'more directional' towards the xy plane. Therefore, this coherent scattering could not be detected along the z-direction in the experimental geometry used here when using coherent excitation. Our results suggest that determination of the full extent of the spectral-shifts requires a coherent excitation, and detection in the sample plane. Even though we could not determine the full extent of the spectral-shift under coherent excitation, the disappearance of the dipolar peak in the dark-field experimental geometry implies that the spatial coherence length of the incident light plays a critical role in determining the extent of the electrodynamic coupling in this regime.

For incoherent excitation, the 1D nanoparticle lattices preserve their directional properties to some extent due to the short spatial coherence length of the incoherent light. This is reflected by a decrease in the scattering intensity for polarization perpendicular to the lattice axis as observed experimentally in Figures 3.2 and 3.3 as opposed to disappearance of the of the dipolar peak under coherent excitation.

3.2.5 Influence of 1D lattice structures on quantum dot fluorescence

To test the coupling of quantum dot fluorescence emission to 1D lattices, array structures were fabricated by optically printing 150 nm Ag nanoparticles with a separation of 600 nm. After drying for 1 hour under vacuum, cadmium-selenide zinc-sulfide (CdSe/ZnS) core-shell

quantum dots were drop-cast on the glass substrate at a concentration such that there were no more than 1-2 dots within a few microns of each lattice structure. The diameter of the quantum dots was chosen such that their emission wavelength matched the scattering peak for 150 nm Ag nanoparticles in water. Figure 3.6a shows the measured fluorescence decay of a quantum dot with no associated lattice (distance to nearest Ag nanoparticle greater than 10 µm), exhibiting a biexponential decay. The average over all the isolated quantum dots for the measured lifetimes were $\tau_1 = 4.05 \pm 0.63$ ns for the shorter lifetime and $\tau_2 = 30.16 \pm 1.15$ ns for the longer lifetime. Figure 3.6b and c show the dependence of the two characteristic lifetimes of this decay to the distance between the quantum dot and the nearest Ag nanoparticle compared to the average lifetimes of the 'isolated' quantum dots. We find that both lifetimes decrease as the distance between the quantum dots and the Ag nanoparticles drops, similar to the increased radiative rate exhibited for the near field coupling of quantum dots to plasmonic nanoparticles[81].

In order to isolate the effect of the collective resonance of the lattice structure from the coupling of the quantum dot to a single nanoparticle, a second set of CdSe/ZnS quantum dots were chosen with a fluorescence wavelength to the blue of the scattering peak of a lone 150 nm Ag nanoparticle. These quantum dots were drop cast on the substrate and dried under vacuum before optical printing of the lattices. After being located by fluorescence imaging, lattice structures were printed around each quantum dot to be measured, three nanoparticles on each side in the positive and negative x directions, such that for a 1D lattice of 7 particles, the 4th Ag nanoparticle would be replaced with a quantum dot. The inset to Figure 3.7b shows a dark field image of one of these lattice structures surrounding a quantum dot. These quantum dots also exhibit a biexponential decay, as seen in Figure 3.7a and b. However, unlike the quantum dots matched to the single particle resonance, only the longer of the two lifetimes shows a decrease; τ_2 decreases from 16.92 ± 2.99 ns for isolated quantum dots to 9.23 ± 4.61 ns for those in 1D lattice structures, while τ_1 is measured to be 0.88 ± 0.34 ns

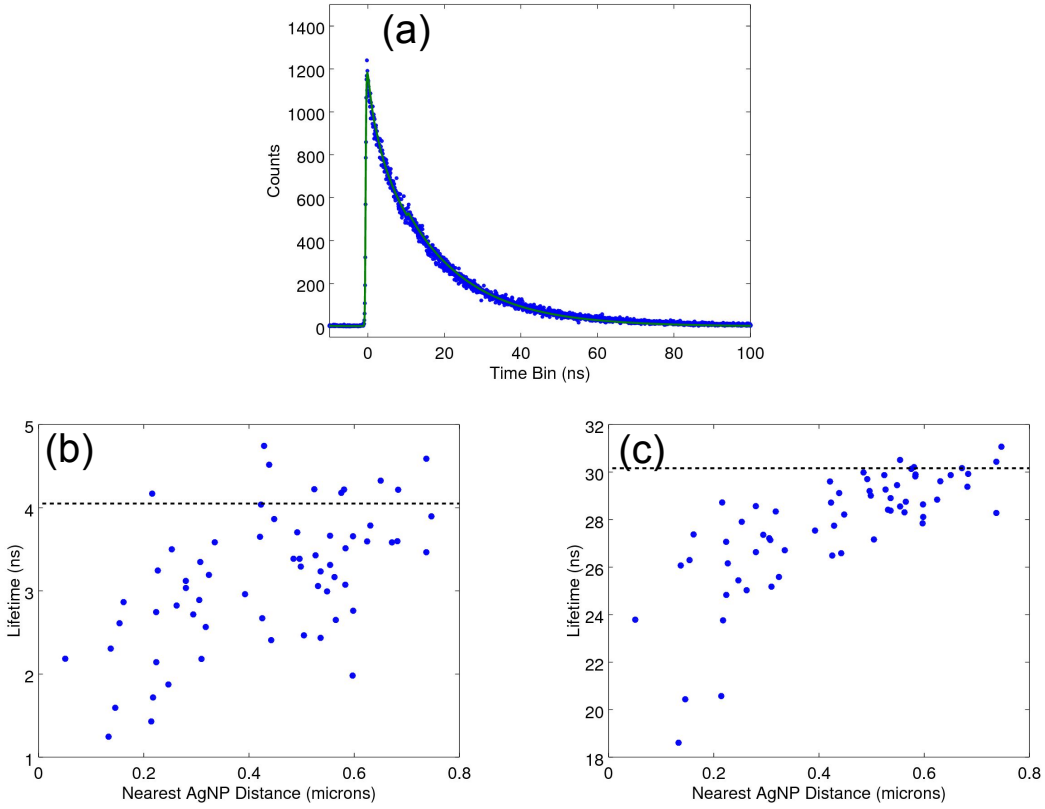

Figure 3.6: (a) Fluorescence decay measured by TCSPC for a single isolated quantum dot deposited on the substrate. The fitted curve is a biexponential decay convolved with the instrument response function for the detection system. (b) Dependence of the shorter lifetime, τ_1, of the quantum dots associated with 1D lattices of 5 Ag nanoparticles on the distance between the quantum dot and its nearest neighbor Ag nanoparticle. The dashed line shows the average τ_1 for isolated quantum dots. (c) Dependence of the longer lifetime, τ_2, of the quantum dots associated with the lattice structures on the distance between the quantum dot and its nearest neighbor Ag nanoparticle. The dashed line shows the average τ_2 for isolated quantum dots.

for the isolated case and 0.85 ± 0.29 ns for the dots once the array was constructed around them. From the distributions of fitted lifetimes τ_2, it was determined that the lifetimes of the isolated dots had a statistically significant difference from those of the dots in arrays at the $p < 0.10$ level. The shorter of the lifetimes, τ_1, did not differ significantly from each

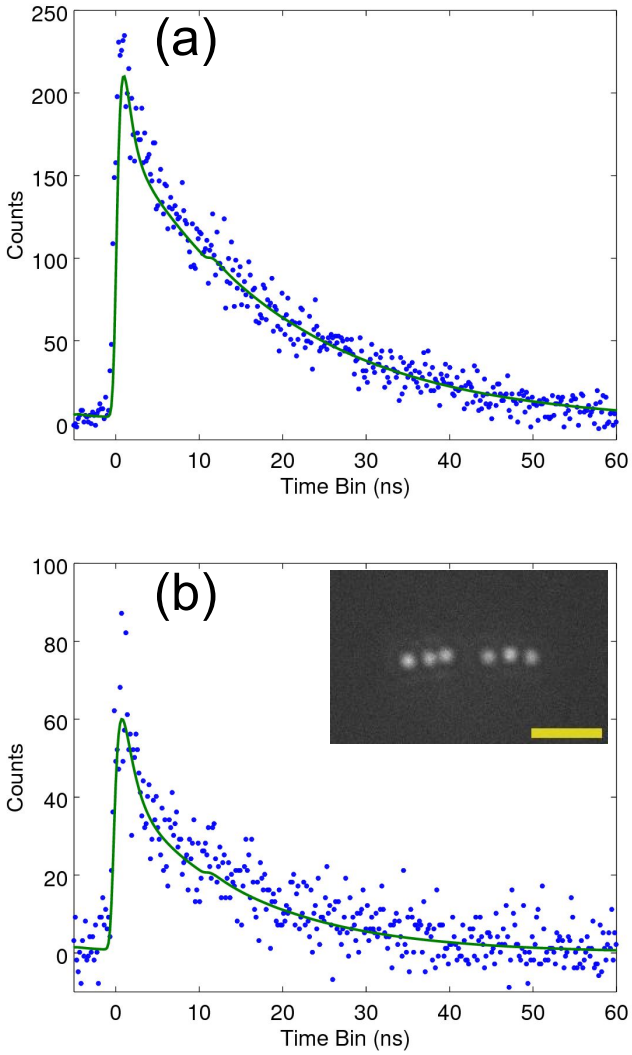

Figure 3.7: (a) Fluorescence decay of a quantum dot from the sample chosen for having an emission wavelength not matching to the LSPR of the 150 nm Ag nanoparticles. The fitted curve is a biexponential decay convolved with the instrument response function of the detection system. (b) Fluorescence decay of a quantum dot located at the center of a 1D lattice structure. (inset) Dark-field image of the 1D lattice structure surrounding the quantum dot in (b). The scale bar is 2 µm.

other. If the fluorescence decay is considered as a sum of two processes that deplete the excited state population of the quantum dot, a faster one corresponding to τ_1, and a slower

one corresponding to τ_2, then the coupling to the 1D lattice can be cast as a third possible process. If this process is slower than τ_2, then measuring the decay of the excited state will show little change in the fastest timescale; if it's only slightly slower than τ_2, this will be observed as an increase in the rate of the process described by τ_2, similar to what we observe here.

3.2.6 Directional dependence of dipole emitters in 1D lattice structures

The light emitted from a spherical quantum dot in a uniform medium is isotropic over all directions due to the transition dipole moment having no directional preference[91]. However, when coupling to a strongly directional structure such as a 1D nanoparticle lattice, this orientational uniformity is broken. Thus, the time-averaged fluorescence of a quantum dot inside a 1D lattice should exhibit a directional dependence related to the lattice's structure. The FDTD calculations in Figure 3.8a and b show the far field radiation pattern emitted from a point-dipole source in a uniform medium aligned along the y (Figure 3.8a) and x (Figure 3.8b) directions as seen at the surface of a hypothetical NA=1.2 objective lens; an average of this radiation distribution over all dipole orientations will give a uniform intensity distribution. When this point-dipole source is placed in a 1D lattice such as the one shown in the inset to Figure 3.7b, the far field radiation pattern takes on a series of structured interference fringes, as seen in Figure 3.8c and d.

We propose that the time-averaged radiation pattern collected from a quantum dot in a 1D lattice is a weighted orientational average over the far-field radiation from interacting and non-interacting transition dipole moments, dependent on the strength of the coupling between the quantum dot and the lattice. To measure the far field radiation pattern of the quantum dots, a relay lens was added to the path of the collected light such that the conjugate plane to the fluorescence image was focused on the surface of an EMCCD. As the conjugate plane and image plane of a lens relay system are related by a Fourier transform ,

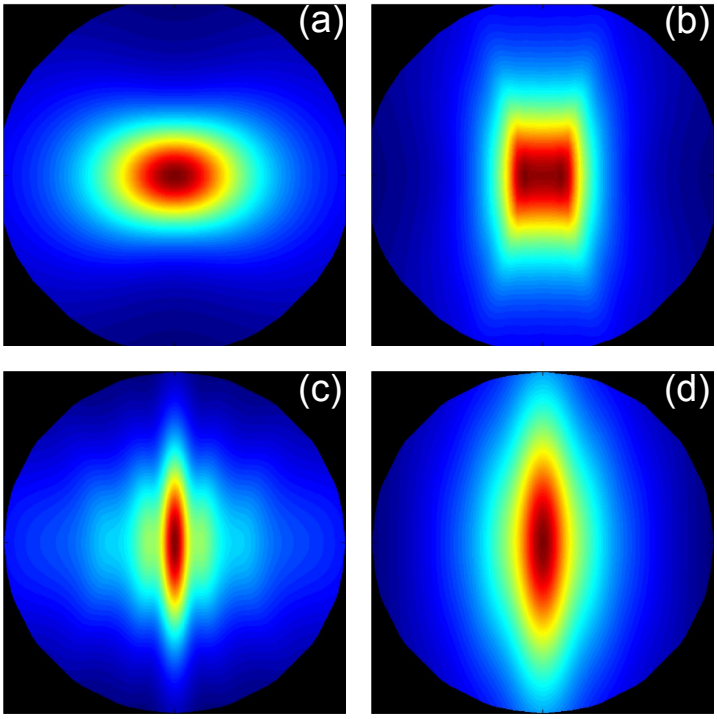

Figure 3.8: (a and b) Simulated far-field radiation patterns from a point-dipole source located at the center of a 5 µm × 1 µm × 1 µm domain, propagated to a surface 100 µm away. The dipole is directed along the y-axis in (a) and the x-axis in (b). The distance and size of the surface on which the intensity was calculated was chosen to match the working distance and NA of the objective used in the experimental conditions. (c and d) Simulated far field radiation patterns from point dipole sources located at the center of a 1D lattice of 150 nm Ag nanoparticles with an interparticle separation of 380 nm. The dipole is directed along the y-axis in (c) and the x-axis in (d).

the fluorescence collected by this system map the angular dependence of the radiation onto the plane of the image. Furthermore, this lens forms a 4f relay system with the tube lens of the microscope, making the collected images a measurement of the light intensity at the surface of the objective, and therefore a direct analogue to the simulations in Figure 3.8. The time-averaged fluorescence conjugate image for an isolated quantum dot is shown in Figure 3.9a, showing uniform intensity over the range of angles within the collected NA. When the quantum dot is placed in a lattice structure such as that in the inset of Figure 3.7b, we

observe the time-averaged fluorescence conjugate image seen in Figure 3.9b.

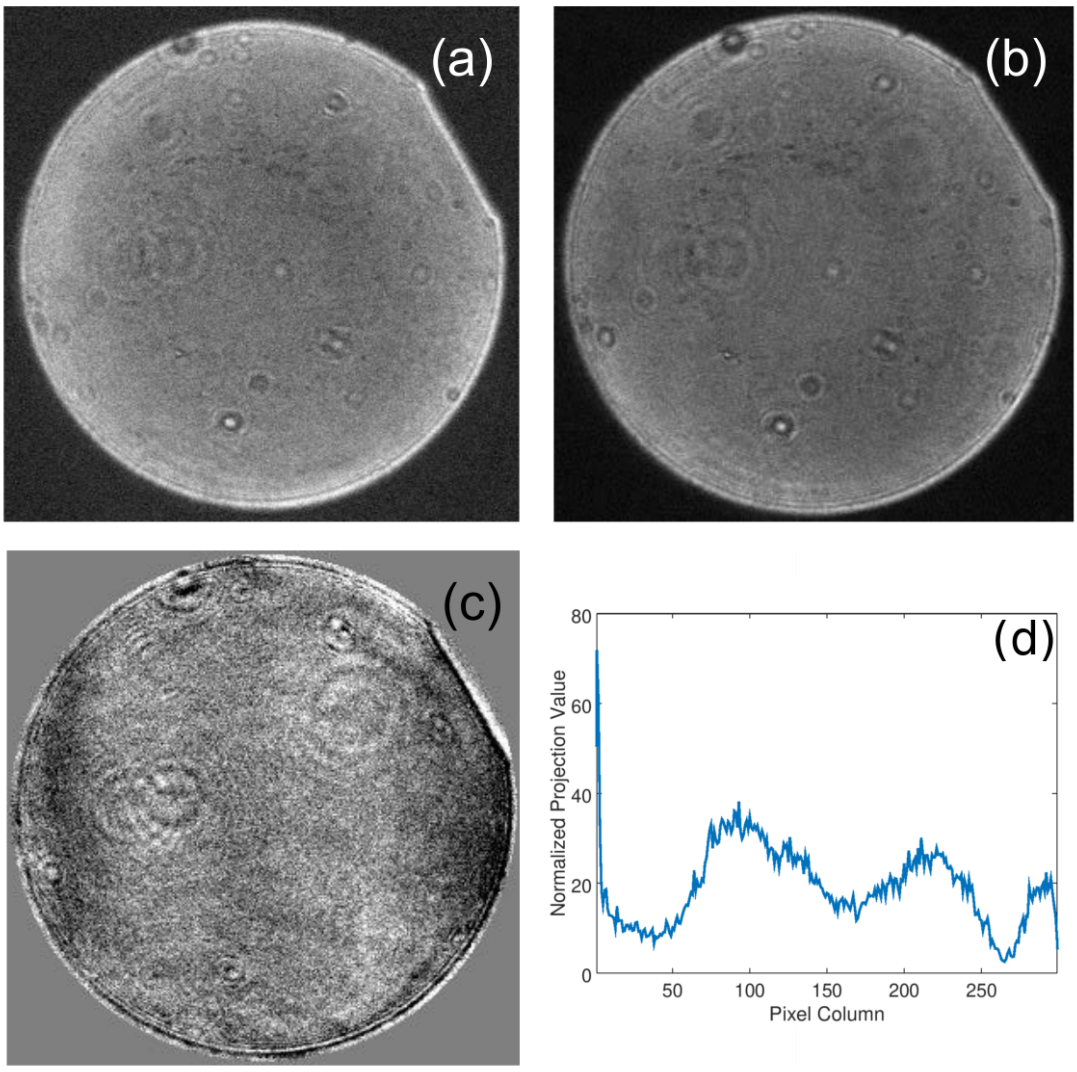

Figure 3.9: (a) Fluorescence conjugate image of an isolated quantum dot. The outer edge of the image corresponds to the maximum NA collected by the objective lens. (b) Fluorescence conjugate image of a quantum dot in a 1D lattice structure. (c) Anisotropic contribution to the fluorescence conjugate image shown in (b). (d) Projection of the image shown in (c) onto the horizontal axis of the image, normalized by the number of pixels within the circle of the measurement along the vertical axis at a particular point.

In order to separate the contributions from the interacting and non-interacting transition dipole moments, the fluorescence image is modeled as a sum of two components: the isotropic

contribution from the time-average of the non-interacting transition dipole moments, and the anisotropic contribution from the interacting transition dipole moments. The isotropic contribution can be measured from the fluorescence conjugate images of the isolated quantum dots as the mean intensity from these images. The anisotropic contribution from each measured quantum dot in a lattice structure is then obtained from treating each image as a linear combination of the isotropic fluorescence taken from the average of the isolated quantum dots and the anisotropic fluorescence from the interaction with the lattice. Figure 3.9c shows the anisotropic component of the fluorescence conjugate image in Figure 3.9b, and the banding pattern is highlighted by a projection of the image onto the horizontal axis, shown in Figure 3.9d. This anisotropic contribution shows an interference pattern similar to that seen in the simulations of Figure 3.8c; we attribute the lack of symmetry in the measured interference pattern to the nonuniformity of the experimental lattice and therefore the differences in the phase of the wavefronts scattered off of the Ag nanoparticles from the uniform geometry used for the FDTD simulations.

3.2.7 Comparison of intermediate-scale and near-field coupling

From our results and discussion, one realizes that the mechanism of dipolar electrodynamic coupling in an 1D array of metal nanoparticles in the intermediate-scale and far-field regimes is completely different from that of the near-field regime[86, 87, 83]. As we noted before, in the near-field regime, the fields of oscillating point dipoles electrodynamically couple to produce a large red-shift of the plasmon resonance for polarization parallel to the array axis[86, 87, 83].

As shown in Figure 3.10, our calculation shows that for a pair of Ag nanoparticles with $d = 160$ nm, the magnitude of the red-shift for $\Delta x = 600$ nm (440 nm between the nanoparticle surfaces) for perpendicular polarization is equivalent to the magnitude of red-shift for $\Delta x = 230$ nm (70 nm between the nanoparticle surfaces) for parallel polarization; the

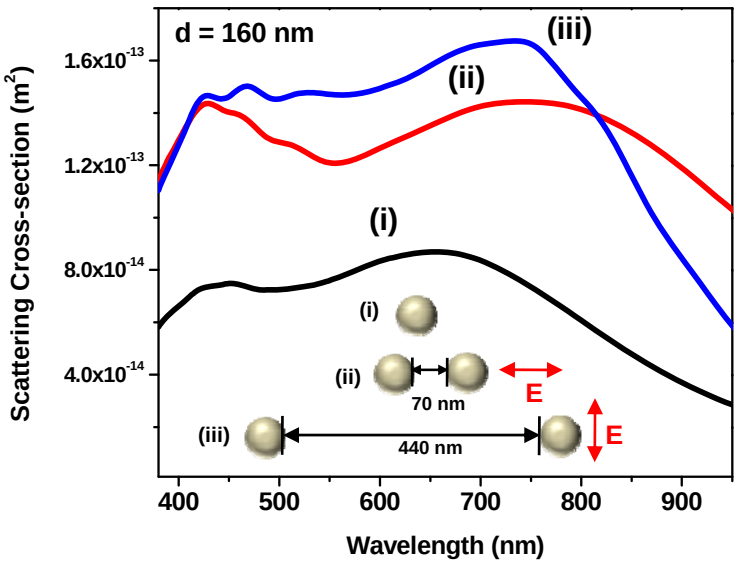

Figure 3.10: For a pair of Ag nanoparticles with $d = 160$ nm, the magnitude of the red-shift for $\Delta x = 600$ nm for perpendicular polarization is equivalent to the magnitude of red-shift for $\Delta x = 230$ nm for parallel polarization.

magnitude of the shift for both cases is ∼100 nm. Hence, for a 1D metal nanoparticle lattice, the magnitude of the spectral shift for the intermediate-scale dipolar coupling is comparable to that of near-field coupling, and thus can be exploited to tune the plasmon resonance of the array for specific applications.

3.3 Conclusions

In conclusion, in combination with dark-field scattering spectroscopy measurements and FDTD simulations, we have shown that for 1D synthetic photonic lattices, consisting of several (N=1 to 6) Ag nanoparticles, the dipolar fields of the individual Ag nanoparticles couple electrodynamically in the intermediate-scale regime. The mechanism of dipolar electrodynamic coupling is mediated by the interference of the scattered dipolar fields. The wavelength of the single particle plasmon resonance and the inter-particle separation play important roles in determining the collective plasmon resonance of the 1D lattice. Our measurements and

simulation show that the magnitude of the spectral shifts in the intermediate-scale coupling in 1D lattices can be compared to that of near-field coupling, and can be exploited to tune the the collective plasmon resonance of the 1D metal nanoparticle lattice. We have further demonstrated that this collective plasmon resonance can be used to enhance the radiative rate of single-photon emitters placed at the center of a 1D lattice. Our results also show that the spatial coherence length of the incident light plays a critical role in determining the extent of the electrodynamic coupling in the intermediate scale regime. On the contrary, this is not an issue in the near-field even when using incoherent light sources.

Our results signify that photonic synthetic lattices can be useful for field-enhanced measurements where tunability of the plasmon resonance is desirable, such as SERS and LSPR based chemical and biological sensing applications[56, 57] as well as create other photonic architectures from nanophotonic constituents[78, 40]. Furthermore, this meso-scale interaction for 2D synthetic photonic lattices can be exploited to produce directional emission through diffractive coupling in the intermediate-scale regime[11, 12] that could potentially lead to applications in quantum optics.

CHAPTER 4
MEASUREMENT AND SIMULATION OF LOCAL DENSITY OF STATES ENHANCEMENT FOR SINGLE-PHOTON EMITTERS IN SELF-ASSEMBLED OPTICAL MATTER

Reproduced in part with permission from: Nolan M. Shepherd, Yuval Yifat, John A. Parker, and Norbert F. Scherer. Measurement and simulation of local density of states enhancement for single-photon emitters in self-assembled optical matter. Manuscript in preparation.

Optical matter provides promising approaches for the manipulation of electromagnetic fields within nanostructures, ordered arrays of plasmonic nanoparticles in solution have been shown to be easily manipulable by the shaping of the incident coherent beam of light[73], with geometries such as regularly-spaced lines[40], rings[92], and close-packed lattices[**?**] follow the general shape of the focused beam that is controlled by phase modulation[73]. Furthermore, arrays of plasmonic nanoparticles are known to have arrangement-dependent collective scattering resonances[11][12]. These properties allow tailoring of optical response of the array based not only on the structure of the constituent nanoparticles but also the field used to create the structure. Previous work has shown that the interference between the incident light and the fields scattered from and within the array provide strong enough field gradients to optically trap nanoparticles with smaller polarizabilities than the relatively low-power incident field would otherwise be capable of trapping without these interferences and enhancements[40].

The electrodynamic interactions of (low-polarizability) semiconductor nanoparticles such as quantum dots with the collective resonances of a regularly-structured array, a system can be created that is analogous to placing single-photon emitters in a photonic crystal lattice[93]. The spatially periodic modulation of the refractive index in a 1D lattice creates a series of

electromagnetic field modes that are either prevented from or allowed to propagate through the lattice based on the wavelength and momentum vector of the mode[25]. Consider an excited-state single-photon emitter placed at the center of such a lattice. The modification of the electromagnetic spectrum of modes is tantamount to altering the local density of states to which the single-photon emitter can couple and therefore alter its coupling to and decay into a radiated field[93]. Since the rate of decay from an excited-state system is directly proportional to the local density of states (LDOS), the modification of the LDOS is manifested in the measured fluorescence decay rate of an emitter placed inside the structure; larger LDOS will result in shorter lifetimes, while a reduced LDOS leads to longer lifetimes when compared to those of the emitter in an isotropic medium.

This modification of the LDOS can be compared to the enhancement of spontaneous emission rates for an excited-state system in a cavity, known as the Purcell effect[24]. The Purcell factor is measured as the ratio of the spontaneous emission rate of the excited-state emitter inside a cavity to the spontaneous emission rate of the same emitter in free space and is proportional to the quality factor of the cavity mode to which the emitter couples and inversely proportional to the mode volume[22]. Photonic crystal lattices achieve small mode volumes by confining light via reflections from the periodic modulation of the refractive index of the lattice and high quality factors by optimising cavity designs for the emission wavelength[93]. In metal nanoparticle systems, coupling of optical fields to nanoparticle plasmon resonances allows for mode confinement below the diffraction limit[22]. Recently, small mode volumes have been realized experimentally for quantum dots coupled to plasmonic nanostructures, achieving strong coupling in the near-field[94].

Periodic nanoparticle structures are readily produced using the interference between the incident light and the scattered light from the plasmonic nanoparticles via optical binding[40, 92]. Furthermore, linear array structures created in this manner are known to co-trap semiconductor nanoparticle quantum dots in the regions between the plasmonic

nanoparticles[40], creating a reconfigurable system for exploring the interaction between single-photon emitters and repetitive array structures.

This chapter presents a direct measurement of the LDOS modification for a single-photon emitter in an optical matter system. In particular, we chose to study radiative enhancements of single-photon emitters in linear array system of optically-bound silver nanoparticles (AgNPs) that exhibit consistent spacing independent of (small variations of) the particle size in the regime where the size-dependent surface plasmon resonance is in the visible spectrum, *i.e.* particle diameters on the order of 50-200 nm, and for their previously demonstrated ability to draw semiconductor nanoparticle quantum dots into the optical trap. As the quantum dots are not as strongly bound as the AgNPs in this array and will diffuse within a region around the AgNPs, it is necessary to correlate any information collected from the quantum dot emission to its instantaneous position with respect to the rest of the array. We find that the emission rate is altered by $\pm 10\%$ from the value of the identical single quantum dots without the AgNPs depending on the emitter's proximity to the nearest AgNP in the array. We corroborated the experimental findings with the electrodynamics simulations that allowed calculated the LDOS for idealized and actual experimental structures.

4.1 Simultaneously Measuring Fluorescence Decay and Particle Configurations

A schematic of the experimental system used to simultaneously measure fluorescence decay rates and image the AgNP-quantum dot array system is shown in Figure 4.1b. The dark-field scattering from the AgNPs and the fluorescence from the quantum dots are separated by wavelength and imaged side-by-side on the same array detector. The positions of all of the nanoparticles are determined by particle tracking and spatial registration via a reference image recombines the separate imaging channels to localize the quantum dot with respect to the AgNPs in the array. The time-correlated single-photon counting (TCSPC) measurement

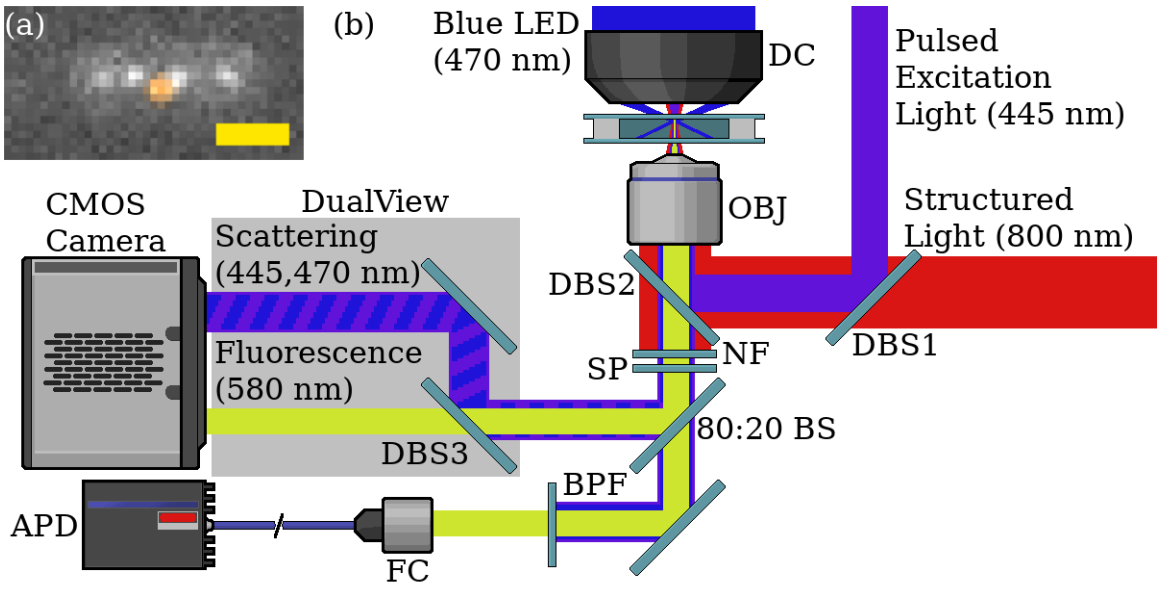

Figure 4.1: (a) Dark-field scattering image of an array of silver nanoparticles in the optical trap, with a false-color spatially-registered overlay of the cotrapped quantum dot's fluorescence. The scale bar is 1000 nm. (b) Schematic of the detection setup for dual-channel imaging and time-correlated single-photon counting. Optical trapping is performed with structured light from a Ti:Sapphire laser that is focused into a sample cell with a water immersion objective. AgNPs are imaged by dark-field microscopy with LED illumination (470 nm), and quantum dot fluorescence is produced by pulsed excitation (445 nm) from a picosecond pulsed fiber-continuum laser. 80% of the collected light is directed to an avalanche photodiode for TCSPC measurements of the quantum dot fluorescence, the remaining 20% of the quantum dot fluorescence and dark-field scattering from the AgNPs are split by wavelength to be imaged side-by-side on the camera. The striped blue and purple beams represent the combined dark-field scattering from the AgNPs used for imaging and backscattering of the excitation from the AgNPs used for time registration to the fluorescence signal. DC: dark-field condenser; OBJ: Nikon 60x water objective; DBS1: dichroic beamsplitter, 532 nm long pass; DBS2: dichroic beamsplitter, 470 nm long pass, partially reflective at 795 nm; DBS3: dichroic beamsplitter, 560 nm long pass; NF: notch filter, 795 nm; SP: 635 nm short pass filter; 80:20 BS: achromatic beamsplitter; BPF: 580 nm bandpass filter, 13 nm bandwidth; FC: fiber collimator; APD: avalanche photodiode. The sample cell consists of a pair of coverslips separated by a 130 μm thick adhesive spacer.

of the quantum dot fluorescence is registered in time to the imaging by a modulation in the excitation beam visible in both measurements as a reference. The registration of the particles' spatial configuration to the TCSPC signal is described in detail in Section 2.3.2.

4.2 Simulating Local Density of States Enhancement

In order to understand how this linear AgNP array system influences the LDOS for a single particle emitter, we performed a series of FDTD simulations on an idealized linear array of 6 AgNPs with a point-dipole source placed at the center, varying the characteristic interparticle distance for this system, shown in Figure 4.2. To highlight the modification of the LDOS at the position of the source due to the presence of the array, we define the ratio $\Lambda(\Delta x, d, \lambda) = LDOS_a/LDOS_0$ as the LDOS enhancement, a function of the AgNP spacings in the array Δx, the position of the source d, and the wavelength of the source λ. Here $LDOS_a$ is the calculated LDOS for the point-dipole source when the AgNP array is present in the simulation domain and $LDOS_0$ is calculated for the source when there are no particles present in the simulation domain. The LDOS enhancement calculated as a function of source wavelength in vacuum in an array with a characteristic spacing of 450 nm is shown in Figure 4.2b; the LDOS for at the source position for the simulation with the AgNPs is divided by the LDOS at the same position with no AgNPs present to obtain the enhancement. Figure 4.2d shows the LDOS enhancement calculated over a series of FDTD simulations where a broad-band point-dipole source is placed in a linear array of AgNPs and the spacing between the particles is varied. As shown in Figure 4.2c, the maximum LDOS enhancement is observed to occur when the source wavelength in the refractive index in the medium surrounding the array, $\lambda^n = \lambda/n$, approximately matches the interparticle spacing, Δx. Considering a point-dipole source emitting at a particular wavelength, we can predict the LDOS enhancement as a function of interparticle spacing, as seen in Figure 4.2c for a source that matches the fluorescence wavelength of the quantum dots used in the experimental sample.

As the LDOS at the position of the emitter in such a system is directly proportional to the spontaneous emission from the excited-state emitter[22], the LDOS enhancement Λ defined

above is analogous to the Purcell factor for a cavity system; for the simulated array, the Purcell factor can be calculated by using a reference with the point-dipole source in vacuum. Since lifetime of an excited state emitter is inversely proportional to the spontaneous emission rate, the modification of the LDOS for a quantum dot in an AgNP array system should be evident in the measured fluorescence decay rate, with the ratio of the decay rate of the quantum dot in the array to the decay rate of an isolated quantum dot being proportional to the LDOS enhancement for a particular configuration of the quantum dot and AgNPs.

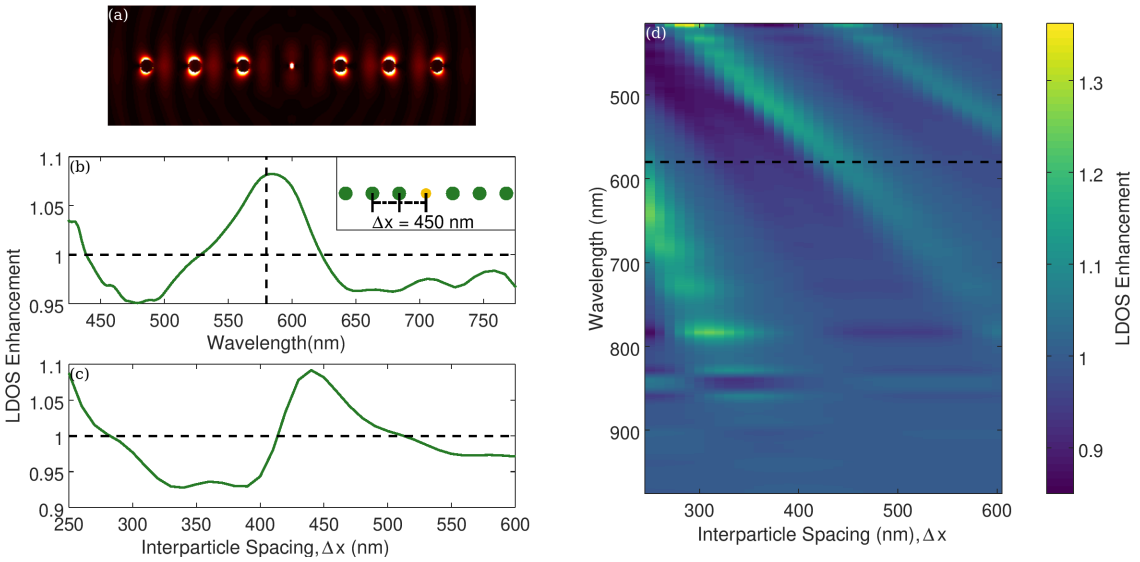

Figure 4.2: (a) Instantaneous electric field intensity at a point in time during an FDTD simulation of a point-dipole source in an array of silver nanoparticles separated by 450 nm. (b) Calculated LDOS enhancement for an FDTD simulation of a point-dipole source in an array of 100 nm diameter silver nanoparticles with an interparticle spacing of 450 nm as a function of the wavelength of the source. The horizontal dashed line represents the LDOS for a point-dipole source in the absence of an array, while the vertical dashed line highlights the wavelength of the quantum dots used for the experimental measurements. The inset shows the configuration of the particles in the array, where the darker green points are the silver nanoparticles and the source is in the center of the array. (c) Calculated LDOS enhancement for a source frequency equal to a vacuum wavelength of 580 nm from a series of simulations where the interparticle spacing is varied over the 250-600 nm range. The horizontal dashed line represents the LDOS for a source in the absence of an array. (d) Calculated LDOS enhancement over the series of simulations as a function of interparticle spacing Δx and source wavelength in vacuum λ.

4.3 Measuring Quantum Dot Fluorescence Decay in an Optical Matter System

For the experimental demonstration of the array's modification of the fluorescence decay rate, linear arrays of AgNPs are prepared by optical trapping using phase-modulated structured light, as described in reference [40]. The 100 nm diameter AgNPs self-organize at a spacing of ∼600 nm according to the wavelength of the laser used for the trapping in water. Using the dual-channel imaging system shown in Figure 4.1b, it is possible to separately track the positions of the quantum dot and the AgNPs. Once the two separate channels are spatially registered, the dots are observed to frequently sample the region between two AgNPs in the array. The concentration of quantum dots in solution is chosen so that only one is likely to be found in the region of the AgNP array. This allows the measurement of individual fluorescence photons that are time-tagged to allow correlating them with the simultaneously measured position of the emitter relative to the particles in the array.

To determine the fluorescence decay associated the positional information, the individual photon counts from the TCSPC measurement are associated with the corresponding particle configuration from the imaging video frame in which they were recorded. A full description of this process is contained in Section 2.3.3. The fluorescence decay information can then be categorized by the separation, d, between the quantum dot and the nearest AgNP, creating fluorescence decay histograms for a series of interparticle spacings. The decay rate for each of these interparticle spacings is obtained by fitting a two-exponential decay function convolved with the instrument response function for the detection system, as described in Section 2.7. Examples of these TCSPC histograms for particular values of d and the two-exponential fitting are shown in Figure 4.3. The histogram corresponding to a quantum dot well-separated from any silver nanoparticles as a control is shown in Figure 4.3a. Figures 4.3b, 4.3c show histograms, fitted decays, and images of the quantum dots (as insets) for two of the spacings chosen for the analysis.

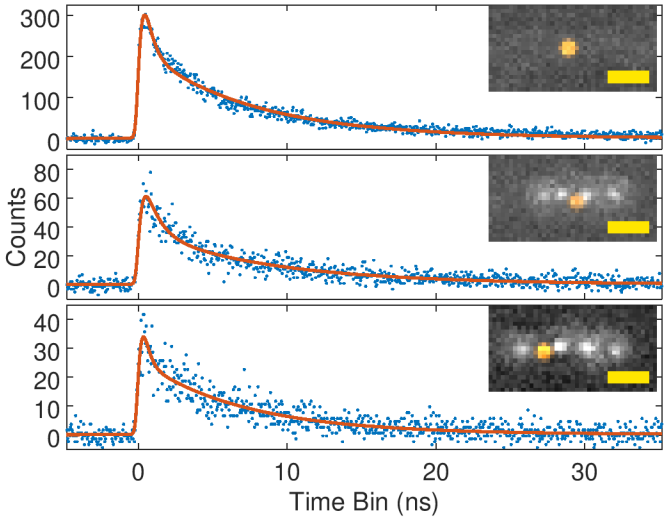

Figure 4.3: (a) Fluorescence decay histogram for photons counted (blue points) when the measured quantum dot was at a large ($d > 1000$ nm) separation from any silver nanoparticles, along with the fitted two-exponential model (orange curve). The inset shows an example grayscale dark-field image with the quantum dot fluorescence overlaid in false color that matches this condition. The scale bar is 1000 nm. (b) Fluorescence decay histogram for photons counted when the measured quantum dot inside an array was at a separation of $d = 375 - 425$ nm from the nearest silver nanoparticle. This corresponds to the simulated condition that exhibits a reduction in LDOS for the quantum dot. The inset shows an example grayscale dark-field scattering image of the AgNPs with the quantum dot fluorescence overlaid in false color, with a AgNP-quantum dot spacing d that matches this condition. The scale bar is 1000 nm. (c) Fluorescence decay histogram for photons counted when the measured quantum dot inside an array was at a separation of $d = 425 - 475$ nm from the nearest silver nanoparticle. This corresponds to the simulated condition that exhibits an increase in LDOS for the quantum dot. The inset shows an example grayscale dark-field scattering image of the AgNPs with the quantum dot fluorescence overlaid in false color, with a AgNP-quantum dot spacing d that matches this condition. The scale bar is 1000 nm.

The presence of a biexponential decay indicates that their are multiple pathways for the quantum dot excited state to decay down to its ground state. It has been reported that core/shell quantum dots including CdSe/ZnS and CdSe/CdS can exhibit a biexponential decay as a result of averaging the fluorescence decay measurements over both their bright "on" states and dimmer "gray" states, where the states can be separated into two different monoexponential decays[95]. The longer of the two components was shown to arise from the

Nearest Neighbor Spacing (nm)	τ_1 (ns)	τ_2 (ns)
225-275	0.53±0.09	7.69±0.20
275-325	0.62±0.15	7.51±0.33
325-375	0.57±0.18	7.69±0.38
375-425	0.81±0.24	8.66±0.58
425-475	0.37±0.20	7.23±0.42
475-525	0.63±0.31	8.43±0.86
525-625	0.55±0.27	8.33±1.22

Table 4.1: Lifetimes from the two-exponential fit to the TCSPC histograms for each selection of interparticle spacings d.

photons collected while the quantum dots were in their bright state and the shorter from the dim state. The high measured quantum yield from the bright state and single decay rate were attributed to a radiative-only pathway, k_r, while the shorter-lifetime dim state was attributed to a combination of radiative decay and Auger processes, $k = k_r + k_{\text{Auger}}$[95]. The presence of a radiative contribution to both components correlates well to the nearest-neighbor-spacing-dependent lifetimes reported in Table 4.1 and Figure 4.6 - both lifetimes show a similar dependence on the spacing, suggesting that both contain a radiative component affected by the LDOS modification due to the array. Following from this explanation, the rest of the analysis focuses on the longer of the two lifetimes as it should be related only to the radiative relaxation of the quantum dot excited state. Therefore we define the decay rate enhancement as the ratio $\kappa_E = k_a/k_0$ where $k_a = 1/\tau_2$ is the decay rate for the longer time component measured from a quantum dot inside the AgNP array and k_0 is the decay rate for a quantum dot isolated from AgNPs.

The means and standard devations of the lifetimes reported in Table 4.1 were obtained by treating the photon count events for each nearest neighbor spacing bin as a separate ensemble. Each of these ensembles contains information on a small distribution of nearest neighbor spacings, their corresponding nanoparticle configuration determined from the dual-channel

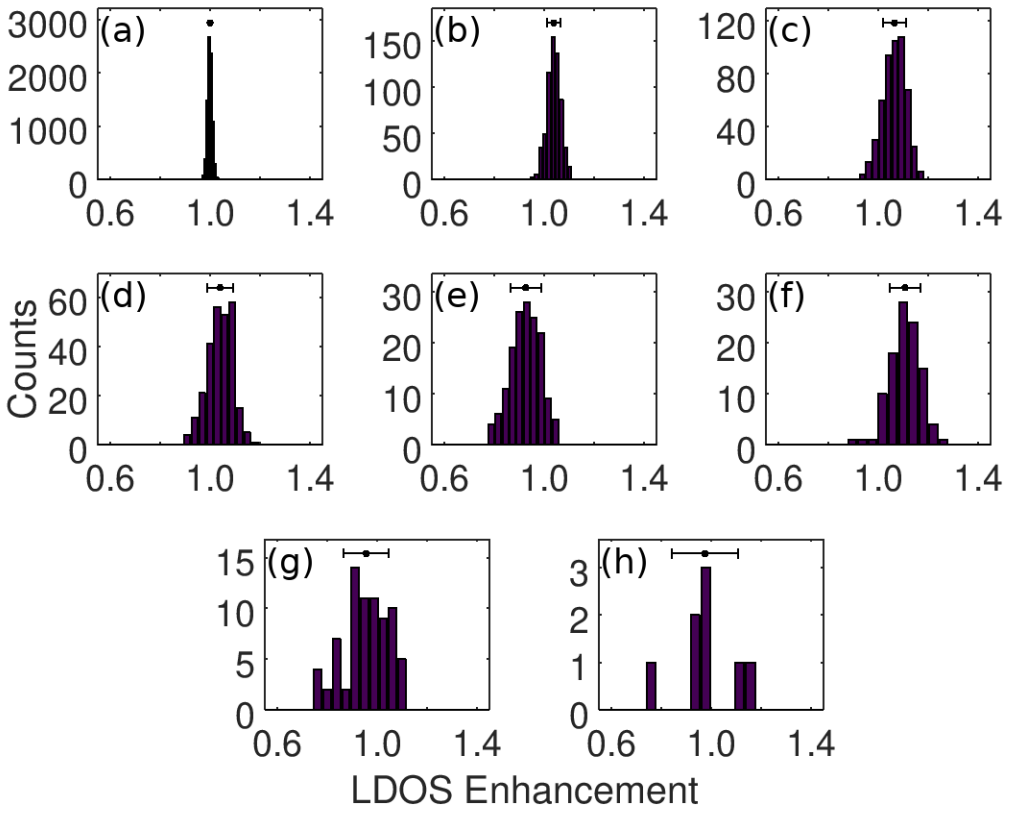

Figure 4.4: Distributions of the LDOS enhancements κ_E obtained from fitting the IRF-convolved two-exponential model to the randomized selections of photon events for (a) video frames where the quantum dot was well-isolated from any AgNPs and frames where the nearest neighbor AgNP was within (b) 225-275 nm, (c) 275-325 nm, (d) 325-375 nm, (e) 375-425 nm, (f) 425-475 nm, (g) 475-525 nm, or (h) 525-625 nm of the quantum dot. The black point and error bars above the histogram bins represent the mean and standard deviation for each histogram.

imaging videos, and the fluorescence decay rates for the environments described by those configurations. The bins were chosen by 50 nm increments in the nearest neighbor spacing with the exception of the longest-distance bin, where the last two were combined to obtain high enough signal-to-noise ratio for the two-exponential fitting. While all these environments are similar within the distance between the quantum dot and the nearest neighbor AgNP, the LDOS enhancement may differ by as much as $\sim$15% over the width (50 nm) of the bin,

as seen in Figure 4.2c. To get a measure of how much the lifetime could vary within each bin, fluorescence decay curves were created by randomly selecting half of the video frames within the bin and combining the corresponding TCSPC photon events. The lifetime for each random selection was determined by fitting to the two-exponential model as seen in Figure 4.3, and the process of random selection was repeated up to half the number of frames within each nearest neighbor bin. In this manner, a distribution describing the mean and spread of the lifetimes and therefore LDOS enhancements for each nearest neighbor bin could be obtained. The histograms of each of these distributions with respect to the LDOS enhancement is shown in Figure 4.4.

As the spacing between the AgNPs in the experimentally-measured arrays remains close to the optical binding distance $\Delta x \approx 600$ nm as opposed to the varying Δx of the simulated idealized arrays, a set of Generalized Mie Theory (GMT)[96] simulations were conducted to calculate the theoretical LDOS enhancement for the observed configurations. For each of the nearest neighbor spacings used to create the fluorescence decay histograms, a series of typical particle configurations were chosen from the corresponding video frames. The positions of the particles from these frames were used in the series of GMT simulations to calculate the LDOS enhancement for these particular configurations. Figure 4.5 shows two examples of the calculated LDOS enhancement in arrays of 100 nm AgNPs, chosen for frames with nearest neighbor spacings corresponding to both the greatest reduction in fluorescence decay rate observed and for the largest increase in observed fluorescence decay rate over the case of an isolated quantum dot. As expected from the idealized simulation, the peak LDOS enhancement occurs at a wavelength commensurate with the nearest neighbor spacing, and the spacing matching the experimental condition where the largest decay rate enhancement was measured has a peak LDOS enhancement at the emission wavelength of the quantum dot.

Figure 4.6 summarizes the results of these measurements as a function of the spacing

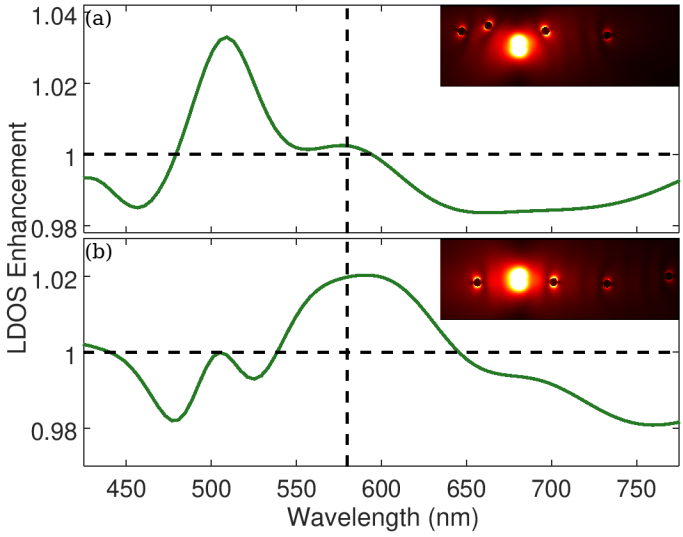

Figure 4.5: (a) Calculated LDOS enhancement for a GMT simulation of a point-dipole source in an array of 100 nm diameter AgNPs at the positions of the particle tracked from the image in the inset to Figure 4.3b as a function of the wavelength of the source. The horizontal dashed line represents the LDOS for a point-dipole source in the absence of the array, while the vertical dashed line highlights the emission wavelength of the quantum dot. The inset shows the instantaneous field intensity at a point in time during the FDTD simulation of the array. (b) Calculated LDOS enhancement for a GMT simulation of a point-dipole source in an array of 100 nm AgNPs nanoparticles at the positions of the particle tracked from the image in the inset to Figure 4.3c as a function of the wavelength of the source. The horizontal dashed line represents the LDOS for a point-dipole source in the absence of the array, while the vertical dashed line highlights the wavelength of the quantum dot. The inset shows the instantaneous field intensity at a point in time during the FDTD simulation of the array.

between the quantum dot and the nearest neighbor AgNP. The experimentally-determined LDOS enhancement matches the GMT- and FDTD-simulated LDOS enhancements for arrays with spacings around the wavelength of the fluorescence of the quantum dot in the medium ($\Delta x \sim \lambda^n$ =436 nm), exhibiting both an increased decay rate for the bin that contains the spacing exactly equal to λ^n, a decreased decay rate for the immediately shorter spacing, and trending back towards the isolated case for the immediately longer spacing. While the error bars (from the standard deviation of the distributions shown in Figure 4.4) are on the same order of magnitude of the difference between the minimum and maximum simulated LDOS

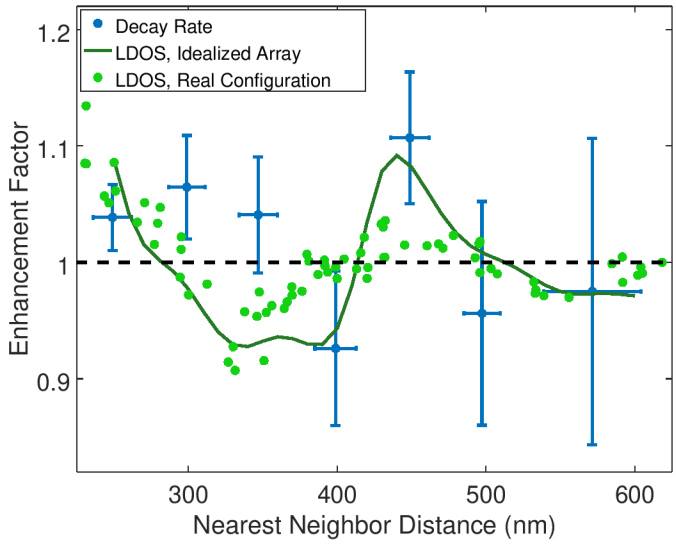

Figure 4.6: Comparison of the measured fluorescence decay rate enhancement for a quantum dot cotrapped in a silver nanoparticle array (blue points and error bars) to the simulated LDOS enhancement at a source wavelength of 580 nm of a point-dipole source in an idealized array (dark green line) and for particle configurations corresponding to measured particle positions during the experiment (light green points) as a function of silver nanoparticle-quantum dot/source spacing. The horizontal dashed line represents the decay rate enhancement for a quantum dot far from any silver nanoparticles and the LDOS enhancement for a point-dipole source in the absence of an array.

enhancement, the distribution of enhancements for each nearest neighbor bin was determined to have a statistically significant difference between their means and showing no change from the isolated case at the $p < 0.05$ level, save for the bin centered at $d \sim$575 nm. This last bin is expected to be nearly equivalent to the isolated case, as the interaction between the quantum dot and the AgNPs decays with distance.

On the smaller spacing side of the LDOS enhancement curve, the quantum dot is moving towards a near-field interaction with the nearest AgNP. As the distance between the quantum dot and the AgNP decreases, the coupling between two increases, and the near-field enhancement of decay rates of quantum dots in plasmonic systems is well known[97].

4.4 Conclusion

In summary, we have experimentally demonstrated the manipulation of the fluorescence decay rate of a single-photon emitter in an optical matter system consistent with the modification of the LDOS available to the emitter based on the configuration of the system's constituent nanoparticles. Both enhancement and de-enhancement of the radiative rate are demonstrated based on the AgNP-quantum dot separation in the regime where the spacing approaches the fluorescence wavelength in the medium ($d \sim \lambda^n$). The rearrangeable nature of optical matter systems opens up the possibility of manipulating these emissive properties based on the applied phase on the structured light used to organize the system. We expect that even greater enhancements are feasible by extending the optical matter system from a 1D linear array to a 2D lattice and by further optimising the interparticle spacings.

CHAPTER 5

SELECTIVE INDUCTION OF OPTICAL MAGNETISM

It is well known that one can create a magnetic field by passing a DC or AC electric current through a coil of a conductor (*i.e.*, a wire); a phenomenon described by the Maxwell-Faraday law of electromagnetic induction[6]. Nuclear magnetic resonance and electron spin resonance (NMR and ESR) spectroscopies involve the interaction of a spin with a magnetic field. Mathematically, these phenomena can be understood as the curl of the electric field (*i.e.*, from the current or spin) producing a (time varying) magnetic field or the inverse process. Thus, it should be possible to induce a magnetic response in materials, either through the design of the structure and/or by employing an electric field with instantaneous curl, by creating an instantaneous "circulating" current.

Magnetic resonance is conventionally associated with absorption and emission of electromagnetic radiation in systems that possess magnetic moments and (spin or orbital) angular momentum. NMR and ESR are described by an interaction of the magnetic moments of charged particles with spin angular momentum (nuclear or electron, respectively) with an external magnetic field, and typically occur at radio or microwave frequencies[24, 98, 99, 100]. Magnetic dipole transitions in atomic systems, which can occur at optical frequencies, involve changes in the total angular momentum (spin and angular). However, the magnetic dipole interactions with applied electromagnetic fields are orders of magnitude weaker than electric dipole transitions[16]; with the exception of rare earth ions such as Eu^{3+} that have naturally

occurring magnetic resonances with strengths comparable to the electric resonance[17]. Interestingly, Novotny and co-workers recently demonstrated selective excitation and enhancement of the magnetic dipole excitation of Eu^{3+} using the spatially localized magnetic field associated with focused azimuthally polarized light[101].

Nano-to-meso scale materials are known or can be designed to have magnetic dipole modes even though they do not intrinsically possess spin or orbital angular momentum. For example, Mie-type dielectric resonators with high refractive index such as Silicon[102], Mie scattering from noble metal nanoparticles (with diameter ~ 100 nm or larger) exhibit multipolar scattering involving both electric and magnetic modes at optical frequencies that stem from retardation[103], or can be induced using circularly polarized light. A simulation study with cylindrical vector beams (CVBs) indicated the potential manipulate multipolar phenomena in multiparticle dielectric resonators, and selectively excite "dark modes" in the dielectric resonators[104]. Electromagnetic meta- or "left-handed" materials, which do not occur in nature and must be constructed, have both negative permittivity (ε) and permeability (μ) in some range of frequencies[105, 106, 107]. Achieving negative ε and μ is synonymous with having strong (and relatively sharp) electric and magnetic (dipolar) resonances, respectively. Spectral overlap of the electric and magnetic resonances, which would ideally be comparable in magnitude (cross-section), would yield a meta-material that is expected to have a negative refractive index at optical frequencies[108, 109, 110, 111], exhibit unidirectional scattering[112, 113], or Fano resonance[112, 114].

In this chapter we present an approach to selectively excite and measure magnetic or electric multipolar resonances in nano-to-meso scale materials, and analyze these resonances and their magnetic or electric nature via Finite-Difference Time-Domain (FDTD) calculations. The systems we study are meso-scale structures consisting of metal (Ag) nanoparticles that are covalently attached to the surface of a dielectric (SiO_2) core. These (dielectric-metal) core-satellite structures, termed nano-clusters or "meta-atoms", are putative building

blocks of self-assembled into meta-materials and meta-fluids[115, 116, 117], because they are expected to have strong magnetic responses, with spatially isotropic properties scalable to macroscopically large samples[108, 115, 116, 117]. They rely on the plasmonic resonant feature of the metal nano-particles and their electromagnetic coupling to create a circular "displacement" current[108, 109, 110, 111].

Here, we show that (focused) azimuthally polarized light, a cylindrical vector beam (CVB)[18], that has an instantaneous curl of the electric field, can excite an oscillating cylindrical current in space that efficiently induces an AC magnetic response in metal nanoparticle based systems. In fact, the vector beam spectroscopy that we demonstrate is a direct manifestation of the Maxwell-Faraday equation[6], $\nabla \times \mathbf{E} = -\partial \mathbf{B}/\partial \mathrm{t}$. Instead of the magnetic fields being created by induction due to circulating electric currents (*i.e.*, electromagnets), here the electric field oscillates at sub-petahertz frequencies (*i.e.*, visible light). The induction arises from displacement currents created by resonant excitation of electric dipoles in the nanoparticles that are, in turn, electrodynamically coupled (from particle to particle) around the core-satellite cluster. Our FDTD calculations with multipole expansion analysis show that excitation with azimuthally polarized light selectively enhances magnetic vs. electric dipole resonances by 100-fold in experiments. Multipolar resonances (*e.g.* quadrupole and octupole) are enhanced 5-fold by focused azimuthal beams vs. linearly polarized light. Moreover, we also measure spatially orthogonal (pure) electric multipolar resonances by excitation with radially polarized light.

Unfortunately, three-dimensional nano-clusters synthesized by nano-chemistry suffer from inhomogeneities in nanoparticle size, shape, and in the arrangement and density of metal nanoparticles on the surface of a dielectric (or other) core, which cause variations in the spectral responses and hence of the permittivity and permeability of the nano-cluster meta-atoms. As is now well appreciated in single molecule science these variations and heterogeneities cannot be uniquely ascertained from ensemble spectra. Thus, in addition to selectively

exciting magnetic/electric modes in these nano-clusters, measuring the optical response of single nano-clusters is an essential aspect of material characterization. Therefore, we conduct our measurements with focused vector beams on single nano-clusters of varying size and nanoparticle surface density, characterize the same single nano-clusters by transmission electron microscopy (TEM) and conduct FDTD simulations for comparison. These correlated measurements and simulations give an appreciation for the heterogeneity of the magnetic and electric multipolar responses.

5.1 Generation and Characterization of Cylindrical Vector Beams (CVBs)

The state of polarization of scalar beams (*e.g.*, linearly, elliptically, and circularly polarized light) does not depend on the spatial location over the beam cross-section; they have spatially homogeneous states of polarization. On the other hand, CVBs are solutions of Maxwell's equations that possess spatially varying polarization with cylindrical symmetry in both amplitude and phase[18]. Such beams can have: (i) their electric field aligned in azimuthal orientations while their magnetic field is radially directed with respect to the optical axis; or (ii) their magnetic field has azimuthal orientations while the electric field is radially polarized with respect to the optical axis or other more complex forms[18, 118, 3, 119, 19]. These are respectively known as azimuthally and radially polarized CVBs. Figure S1a¡experimental chapter figure¿ depicts an azimuthal CVB showing that these cylindrical beams change their handedness over each half of the optical cycle. Therefore, azimuthal CVBs have instantaneous curl, but no net angular momentum. The CVBs with azimuthal and radial polarization can be expressed as superpositions of orthogonally polarized Hermite–Gauss HG_{01} and HG_{10} modes[3, 19] as depicted in Figure 2.8a.

Both active and passive methods have been developed to generate CVBs[19, 120, 20]. The vector beam generator that we reported in 2005[20] and others are not achromatic. For the present experiments, we use a liquid-crystal (LC) based polarization converter (from

ARCoptix) that uses twisted nematic liquid crystals sandwiched between one uniform and one circularly rubbed alignment layer to generate azimuthally and radially polarized CVBs[46]. Section 2.4 and Figure 2.8 detail the optical set-up and relevant characteristics of the azimuthal beam.

5.2 Focused Cylindrical Vector Beams and Nano-Cluster Excitation

It has been shown that focusing CVBs with a lens (objective) with a finite numerical aperture in the non-paraxial limit causes spatial separation of the electric and magnetic fields at the focus and leads to longitudinal polarization of the electric or magnetic field[3, 121]. The longitudinal (z)-component of the magnetic (electric) field dominates the transverse (ρ) component of the magnetic (electric) field in the focal region, whereas the electric (magnetic) field component is purely transverse for azimuthal (radial) polarized beams under very high-NA focusing[3, 121]. The distributions of the radial component of the electric field ($|\mathbf{E}_\rho|$), and the longitudinal component of the magnetic field ($|\mathbf{H}_z|$) are shown in Figures 5.1a and 5.1b. Whereas Novotny and co-workers utilized the longitudinal component of magnetic field, $|\mathbf{H}_z|$, of a focused azimuthally polarized beam to enhance an "inherent" magnetic dipole transition in Eu^{3+} ions embedded in a Y_2O_3 nanoparticle[101], our spectroscopic measurements emphasize the transverse component of the electric field, $|\mathbf{E}_\rho|$. The focused azimuthally polarized beam excites the dipoles in the metal nanoparticle "satellites" and drives an instantaneous curl of their collective electronic excitation; thus inducing a mesoscopic magnetic response in a core (SiO_2) – satellite (Ag) nano-cluster. This is illustrated in Figure 5.1c; the azimuthally polarized (focused) electric field creates dipolar plasmon excitations of the Ag nanoparticles and hence an instantaneous displacement current amongst the equatorially coupled nanoparticles (Figure 5.1d). The instantaneous cylindrical displacement current is expected to induce a time varying magnetic field according to $\nabla \times \mathbf{E} = -\partial \mathbf{B}/\partial \mathrm{t}$ that is directed along the poles of the nano-clusters as shown in Figure 5.1e.

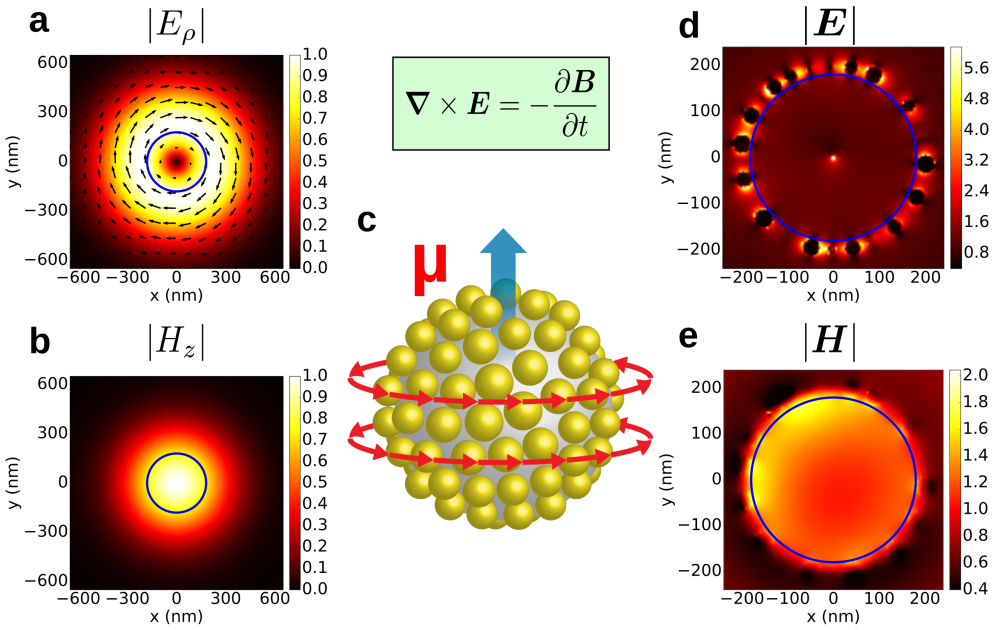

Figure 5.1: Azimuthally polarized vector beam and excitation of nano-clusters. (a) Simulation of the transverse component of the incident electric field ($|\mathbf{E}\rho|$), and (b) longitudinal component of the incident magnetic field ($|\mathbf{H}_z|$) of an azimuthal beam focused with NA = 1.4. (c) Schematic of a core (SiO_2)–satellite (Ag) nano-cluster and the manifestation of the Maxwell-Faraday equation at an instant in time with an azimuthal vector beam. The blue arrow that depicts the induced magnetic field is oriented along the z-axis, which is the beam propagation direction. (d) the electric field enhancement, $|\mathbf{E}_{\text{scat}} + \mathbf{E}_{\text{inc}}|/|\mathbf{E}_{\text{inc}}|$, and (e) the magnetic field enhancement, $|\mathbf{H}_{\text{scat}} + \mathbf{H}_{\text{inc}}|/|\mathbf{H}_{\text{inc}}|$. (d, e) are the results of FDTD simulations of the core-satellite cluster shown in (c) with an incident field at 700 nm wavelength. The blue circle represents the SiO2 core with a diameter of 360 nm. The simulated AgNPs are 43 nm in diameter. The inhomogeneities in the electric and magnetic field intensities arise due to the non-symmetric packing and size distribution of the Ag nanoparticles that are created at the "equatorial" cross-section.

5.3 Nano-Cluster Synthesis

We prepared self-assembled core (dielectric) – satellite (metal) nano-clusters by covalently attaching metal nanoparticles to the surface of a chemically functionalized dielectric core. Figure 5.2 represents a facile synthetic strategy for core (SiO_2) – satellite (AgNPs) nano-clusters. Briefly, citrate-stabilized AgNPs with different diameters were synthesized by a method modified from the literature[122]. Silica particles functionalized with thiol groups

were mixed with silver nanoparticles (AgNPs) and dispersed in a 10 mM citrate buffer (pH = 3.5). We tuned the electrostatic interactions to control the AgNPs density onto the Silica core surface - the more highly protonation citrate at low pH makes the AgNPs less repulsive to each other and allows more dense packing of AgNPs around the silica core via Ag-S dative bonding[123]. The resulting solution of nano-clusters is dispersed in deionized water for storage and further measurements. The assembled structures were characterized via TEM and UV-VIS spectroscopy. Figures 5.3a and 5.3e show TEM images of two typical nano-clusters with different core and satellite size.

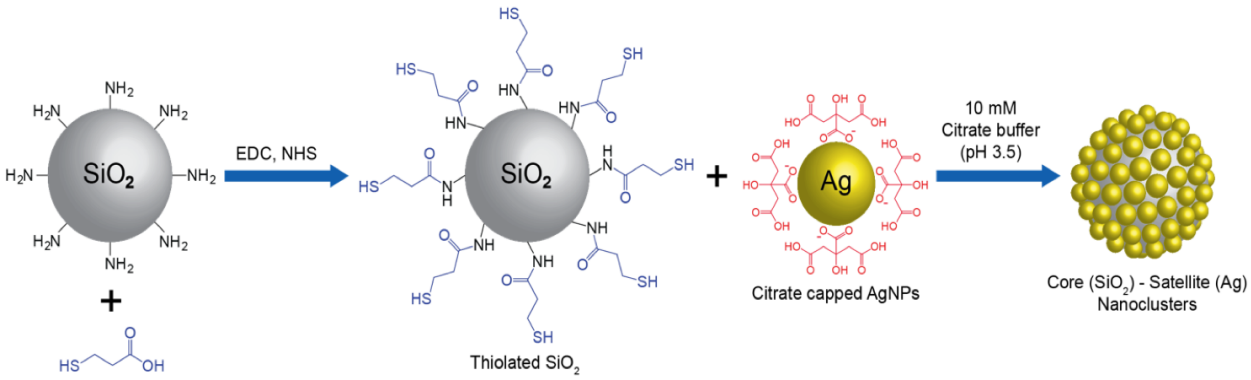

Figure 5.2: Schematic representation of the assembly of core-satellite nano-clusters. The size of SiO_2 particle core and Ag nanoparticle satellite could be adjusted.

5.4 Measurement of Single Nano-Cluster Spectra

We measured the scattering spectra of individual core (SiO_2)-satellite (Ag) nano-clusters with different core and satellite sizes being illuminated with focused linearly, azimuthally and radially polarized light using the vector beam spectroscopy set-up described in Section 2.4 and Figure 2.8b. The sample was made by drop casting the nano-cluster aqueous dispersion on a formvar coated TEM finder grid that allowed facile correlation of TEM images and optical measurement. After taking TEM images, the grid was immersed in $n = 1.52$ index matching oil and sandwiched by two glass cover slides. Thus the refractive index of the

formvar ($n = 1.50$) and glass slides ($n = 1.52$) is nearly perfectly matched so the reflection and scattering from the oil/formvar interface is very weak. This is important since a significant reflection from the interface will interfere with the back-scattered light from the nano-cluster altering its spectrum.

Figure 5.3 shows representative experimental back-scattering spectra and TEM images for nano-clusters with two different core diameters: (i) Core diameter, $d_c \sim 165$ nm; Satellite diameter, $d_s \sim 30$ nm with a standard deviation, $\sigma \sim 3$ nm; number of satellites, NoS ~ 80 (henceforth called NC_D165nm, corresponds to Figures 5.3a-d); (ii) $d_c \sim 360$ nm; $d_s \sim 43$ nm; $\sigma \sim 5$ nm; NoS ~ 180 (henceforth called NC_D360nm, corresponds to Figures 5.3e-h). Note that the TEM images shown in Figures 5.3a and 5.3e are images of the exact same nano-clusters whose scattering spectra are shown. For both NC_D165nm and NC_D360nm, the scattering spectra exhibit several well-defined peaks across the 500-1000 nm measurement range. However, the spectra differ in details and magnitude for the polarized excitations employed. Also, the peak positions and intensities are quite different for these two samples. For NC_D165nm, the spectra associated with azimuthally and radially polarized light (red and green data, respectively) are weaker (smaller amplitude scattering) than that of linearly polarized light (black points). We attribute this to the limited spatial overlap of the doughnut-shaped focused vector beams with the nanoclusters (total diameter ∼225 nm) compared to a Gaussian transverse intensity profile for the linearly polarized beam and the projections of the induced modes back to the detector. In the case of the focused azimuthal CVB, we estimate the diameter of the electric field annulus to be about 600 nm; because of the polarization and phase variation of the beam, the E-field goes to zero at the very center. There is also a notable feature at 900 nm in the linearly polarized spectra that we discuss below.

For NC_D360nm, the relative intensity of the azimuthal CVB spectrum (red) exceeds that of both the radial CVB (green) and linearly polarized (black) spectra (Figures 5.3f-h). Moreover, there is a distinct peak between 650-700 nm vs. the very broad and slightly

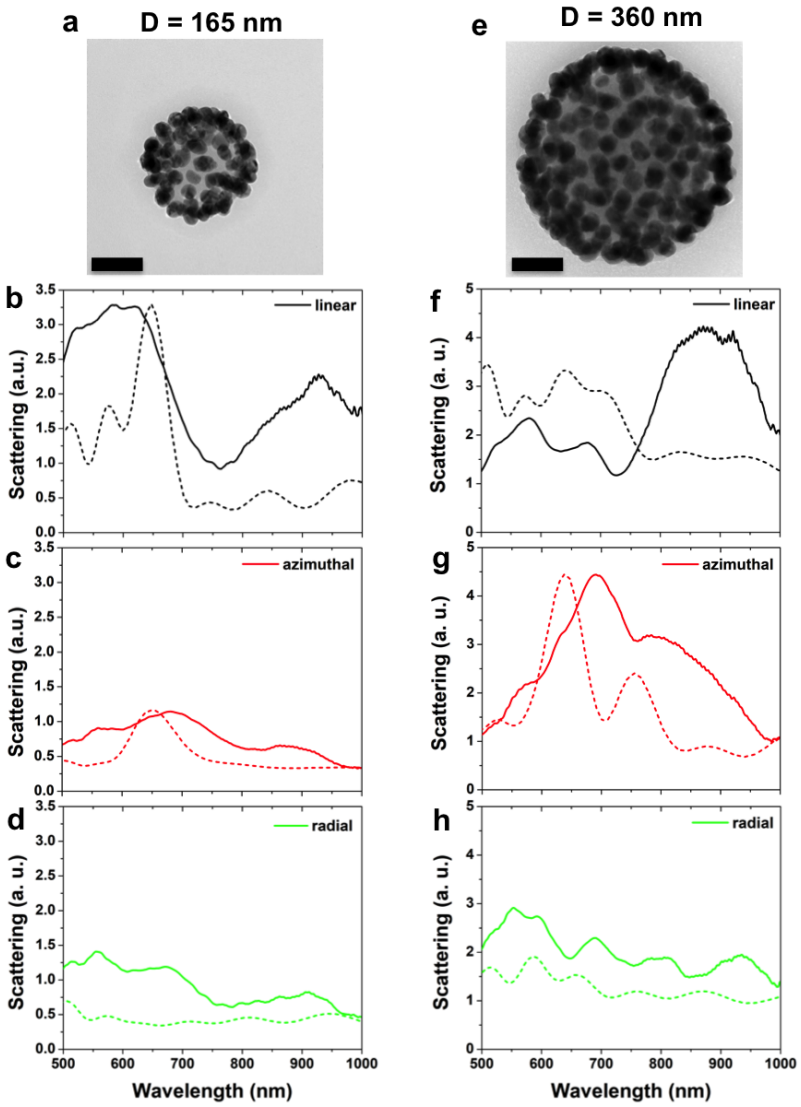

Figure 5.3: Optical back-scattering Measurements and simulations of single nano-cluster spectra excited by cylindrical CVBs and linearly polarized light. (a)-(d) TEM image, experimental and simulated scattering spectra of a particular core-satellite nano-cluster with core size of ∼165 nm and AgNPs of ∼30 nm in diameter. (e)-(h) TEM image, experimental and simulated scattering spectra of a particular core-satellite nano-cluster with core size of 360 nm and AgNPs of ∼43 nm in diameter. The scattering spectra were excited by linearly (black), azimuthally (red) and radially (green) polarized light, respectively. Scale bars in (a) and (e) are 100 nm. While the intensities of the simulated spectra are arbitrary units, all the spectra can be compared with the scales shown. Similarly, the magnitudes of experimental spectra in (b)-(d) can be directly compared and those in (f) to (h). Only the azimuthal spectra were adjusted to match experiment and simulation maximum values.

multi-peaked radial CVB spectrum, which is now more similar to the linearly polarized spectrum. We will discuss specific spectral features below using the corresponding FDTD simulations and multipolar analysis of spectra in the back-scattering direction used in the experiments.

5.5 Simulations of Nano-Cluster Scattering Spectra

We performed extensive electrodynamics simulations to complement and interpret the experimental results and report the results within our measurement spectral window (500 – 1000 nm). The simulation results shown in Figure 5.3 were performed with the same number of AgNPs (assumed spherical) and core diameters as were determined in the corresponding TEM images (Figures 5.3a and 5.3e) as described in the text above. Simulations were performed with the FDTD method[124], using a freely available software package MEEP[48]. The total field-scattered field method was employed to obtain the scattering spectra. Figure 5.3 shows that the experimental and simulated scattering spectra of the nano-clusters exhibit very similar characteristics with the appearance of several well-defined peaks across the entire visible-NIR spectrum for the different light excitation polarization conditions. Achieving this required performing FDTD simulations with the correct number and number density of AgNPs, reasonable distributions of inter-NP distances, and also matching the angular distribution of the electromagnetic scattering to what was done in the experiments. The simulated nano-clusters were built by random packing assuming a 2 nm minimal separation.

However, despite the care taken, there are still differences with the experimental results: (i) the widths of the experimental peaks are often broader; and (ii) the peak positions are somewhat shifted. We attribute these differences to inhomogeneities in size, shape and distribution of the nanoparticles with some of the Ag nanoparticles touching each other (by contrast, a separation $\geq$ 2 nm was set in simulation). Also, the azimuthal and radial states of the experimentally generated cylindrical vector beams are not as perfect as the

simulated fields with some scalar beam contamination (perhaps 5%), which can affect the spectra actually obtained. Moreover, the details of the spectra can change even just with a permutation of the AgNP arrangements even at constant AgNP number on the same core. Therefore, complete agreement is impossible to achieve for such complex structures. Nevertheless, many similarities do emerge that form the basis of a quantitative analysis.

5.6 Assignment of Electric and Magnetic Multipole Features

Understanding the spectral features excited by different types of polarized light requires that we can assign an identity to them. To do this, we perform a near to far field transformation of the total scattering amplitude and then decompose the amplitude into their electric and magnetic multipolar (dipolar, quadrupolar, octupolar) contributions (a detailed description of the procedure is described in Method¡¿). We obtain the dipolar and higher order electric and magnetic modes that give rise to the total scattering (shown in Figure 5.4) for both NC_D165nm (Figures 5.4a-c) and NC_D360nm (Figures 5.4d-f) for the 3 different polarized beams in a backscattering detection geometry for an angular range defined by the experiment. It is well known that the Ag nanoparticles exhibit pronounced Mie resonances; only the electric dipolar mode is excited for single 40 nm diameter AgNPs[83]. However, our FDTD simulations of single SiO_2-Ag core-satellite nano-clusters allow the following assignments: (i) both electric and magnetic modes are excited with linearly polarized light, (Figures 5.4a and 5.4d); hence the scattering spectra obtained are due to excitation of both the electric and magnetic modes; (ii) azimuthally polarized light exclusively excites (and scatters from) magnetic dipolar, quadrupolar and octupolar magnetic modes (Figures 5.4b and 5.4e); and (iii) radially polarized light exclusively excites (and scatters from) electric modes (Figures 3c and 3f). Also, the dominant modes for dc = 165 nm are dipolar and quadrupolar (Figures 5.4a-c), whereas the dominant modes for dc =360 nm are quadrupolar and octupolar (Figures 5.4d-f) at visible-NIR wavelengths. The relative strengths of the electric and magnetic modes

for the three different polarizations are shown in Figures S5 and S6¡¿.

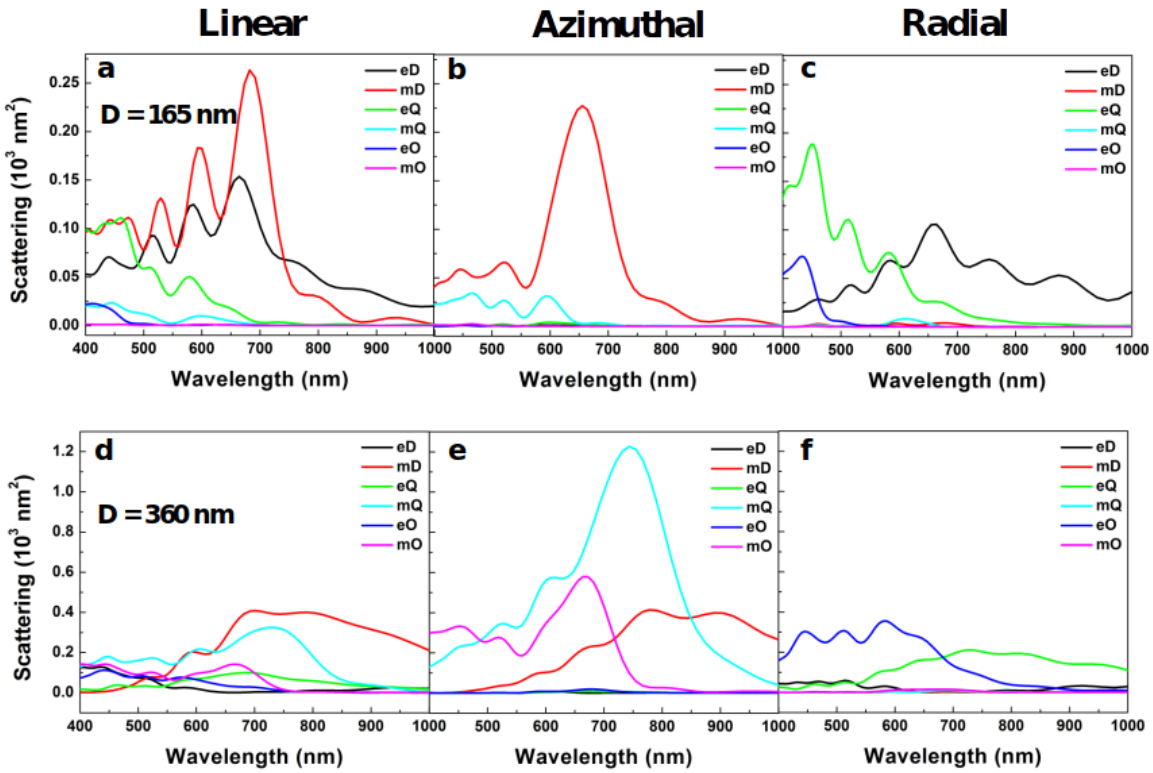

Figure 5.4: Expansion of the FDTD scattering amplitudes into electric and magnetic multipolar modes. (a)-(c) D = 165 nm, and (d)-(f) D = 360 nm. Each simulated spectrum in Figure 5.3 is decomposed into the six lowest order multipolar modes: electric dipole (eD), magnetic dipole (mD), electric quadrupole (eQ), magnetic quadrupole (mQ), electric octupole (eO), and magnetic octupole (mO), respectively. The spectra excited by the azimuthal CVB are exclusively magnetic modes, whereas the spectra excited by the radial CVB are exclusively electric modes. Excitation with focused linearly polarized light gives both.

In order to compare the experimental scattering spectra from the core-satellite nano-clusters to the FDTD simulated results, we also assign electric/magnetic modes of experimental spectra by using simulated multipolar modes as a set of 'basis functions'. Expanding the experimental spectra in terms of overlap integrals with the multipoles as a basis highlights the character of the vector beam scattering from the nano-clusters. Finally, the overlap between the experimental spectra and each of the multipole expansions was then calculated (see more details in Subsection 2.4.1 and Figure 2.9). Figure 5.5 shows the multipolar modes for each

polarization shown in Figure 5.3 for each nano-cluster. We found the analysis of experimental spectra gave the same results as simulated multipole expansion. That is, while linearly polarized beam excites both electric and magnetic modes, the azimuthally polarized beam can selectively excite magnetic multipolar modes, and radially polarized beam selectively excites electric multipolar modes.

It is also possible to determine the current density and electric displacement current excited in the core-satellite structure from simulation. The excited mode is a global oscillation of electric displacement current around the Ag NP ring. Therefore, we conclude that our experimental spectra result from selective excitations in the nano-clusters for specific polarization states of the incident beams; magnetic and electric modes for azimuthally and radially polarized CVBs, respectively, and mixtures thereof when using linearly polarized scalar beams. Specifically, the main peak with the azimuthally polarized excitation of Figure 5.3g is magnetic quadrupole, with magnetic dipole excitation on the longer wavelength size and magnetic octupole on the shorter wavelength side.

The peak at ∼900 nm observed in the linearly polarized experimental spectra is not observed in the simulations. We performed many simulations under various conditions of particle density and interparticle separation, but because the FDTD grid cell we use is 1 or 2 nm, we kept a constraint of 2 nm interparticle separation – we did not consider smaller gaps because the grid size is too large to be certain of converged results. However, the TEM images of the nano-clusters (Figure 5.3) show that short "chains" of Ag nanoparticles with sub-nanometer gaps are formed. To understand the possible spectral ramifications, we performed FDTD simulations with small grid spacing of short AgNP chains by linear excitation along the chain axis. To use finer grids, we performed the simulations with Lumerical (FDTD Solutions). We simulated chains with 2-4 AgNPs and for each chain the gaps/grid sizes were set between 1.0 nm and 0.4 nm. The resonances red-shift when the number of AgNPs was increased or the gaps between AgNPs were decreased. Generally

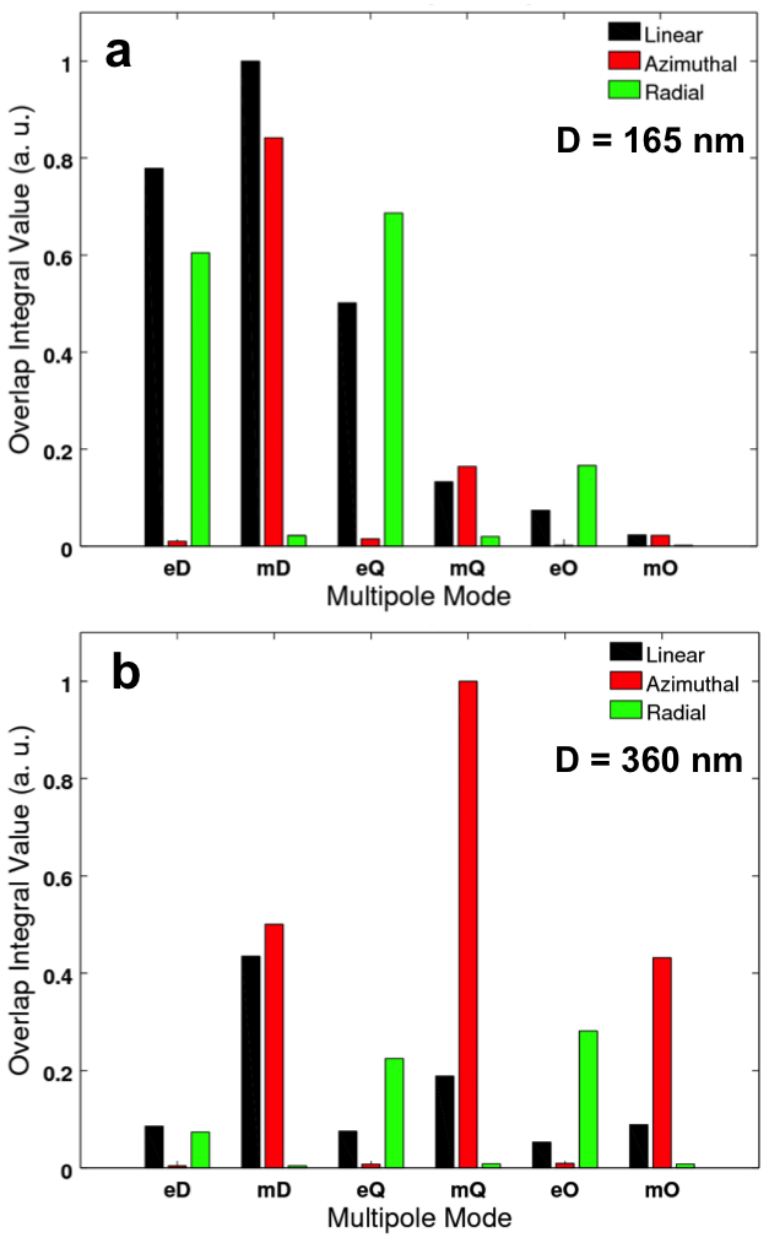

Figure 5.5: Assignment of experimental multipolar mode content. We use the multipolar expansion analysis in Figure 5.4 to determine basis functions and overlap integrals with experimental spectra. (a) D = 165 nm, and (b) = 360 nm. The modes excited by the azimuthal CVB are exclusively magnetic in nature, whereas the excitations by the radial CVB are exclusively electric modes. Excitation with focused linearly polarized light gives both. The larger nano-cluster shows much more higher order multipolar mode content than the smaller one.

the plasmonic resonances of the short chains are in the region of 700-900 nm. One can expect more red-shift (over 900 nm) if there are more AgNPs in the chain (4), or smaller gaps between AgNPs. These results suggest that the broad peak at 900 nm region is due to short chains of AgNPs. This interpretation is further supported by considering the effect of particle density on the experimental spectra. Clusters with lower AgNP density compared to those shown in Figure 5.3 that exhibit virtually no peak at ∼900 nm. Moreover, strong long wavelength (∼900-1200 nm) peaks have been observed in experiment and from other simulations for touching metal nanoparticles[125, 126]. Most interestingly, the ∼900 nm peak is not present in the spectra obtained with CVBs since the modes these create are either perpendicularly polarized to the inter-particle direction (radial CVB) or involve a collective excitation circumscribing (a large portion of) the circumference of the entire core-satellite cluster to create a magnetic excitation (azimuthal CVB). Therefore, we ascribe the 900 nm peak to short chains of AgNPs of somewhat non-spherical shape.

Position dependent nano-cluster spectra shifted away from the azimuthal beam axis and focal plane. Breaking the cylindrical symmetry of the vector beam/nano-cluster system (interaction) should result in changes in the measured spectra. For example, if the sample only interacts with an arc of the focused azimuthal beam, one can envision that the excitation becomes more like that obtained with linearly polarized light; one loses the efficient excitation of the full curl of the CVB. Therefore, we measured the scattering spectra of the same nano-cluster (NC_D360nm) as shown in Figure 5.3e using azimuthally polarized light but with small shifts of the nano-cluster along the y- or z-directions with respect to the beam axis. The results are shown in Figures 5.6a and 5.6b, respectively. Figure 5a shows that as the nano-cluster is moved transversely (along the y-direction), the main peak (at ∼700 nm) decreases (colored spectra), and finally becomes very similar to the spectrum obtained with linearly polarized light excitation (black). As discussed in Figure 5.4, the spectrum excited by azimuthally polarized light is the superposition of magnetic multipolar modes (dipole,

quadrupole, and octupole). The change of the spectra with increasing y-axis shift corresponds to a decrease of the magnetic mode content and an increase of the electric mode content. Also, the feature at ∼900 nm also becomes more intense. Therefore, the collective excitations (*i.e.* longitudinal loops) around the core-satellite clusters are required for magnetic mode excitation.

Figure 5.6b shows a decrease in the magnitude and some changes in the spectral shape of the scattering spectra when moving the beam away from the focal plane (along the axial or z-direction). The decreasing scattering with shift from the focus can be understood as a decrease of spatial overlap of the expanding beam with the nano-cluster. However, the changing spectral shape suggests that more is occurring. Indeed as shown in the inset to Figure 5.6b, the magnetic character of the focused azimuthal CVB, which has a maximal longitudinal amplitude and is most concentrated at the focus, diminishes with increasing shift from the focal plane[3, 121]. There is a progressive diminishment of this spatial segregation and its longitudinal polarization as one moves away from the focal plane so that the electric and magnetic field distributions of the beam are the same in the far field. Moreover, this focused magnetic field will interfere with the magnetic field that arises from the electronic displacement current and the concomitant induction of the magnetic mode. The longitudinally polarized magnetic field of the focused azimuthal CVB can therefore enhance or diminish the degree of excitation of the magnetic mode in the nano-cluster by its relative phase and amplitude. This amplitude diminishes rapidly away from the focal plane[3].

5.7 Conclusion

Electromagnetic responses that are studied at optical frequencies are almost always electric dipolar (or quadrupolar) since magnetic-dipole transitions at optical frequencies have approximately 105 times smaller absorption cross-sections than electric dipole transitions[16] with the exception of the rare earth elements[17, 101] and engineered metamaterials[105, 106, 107,

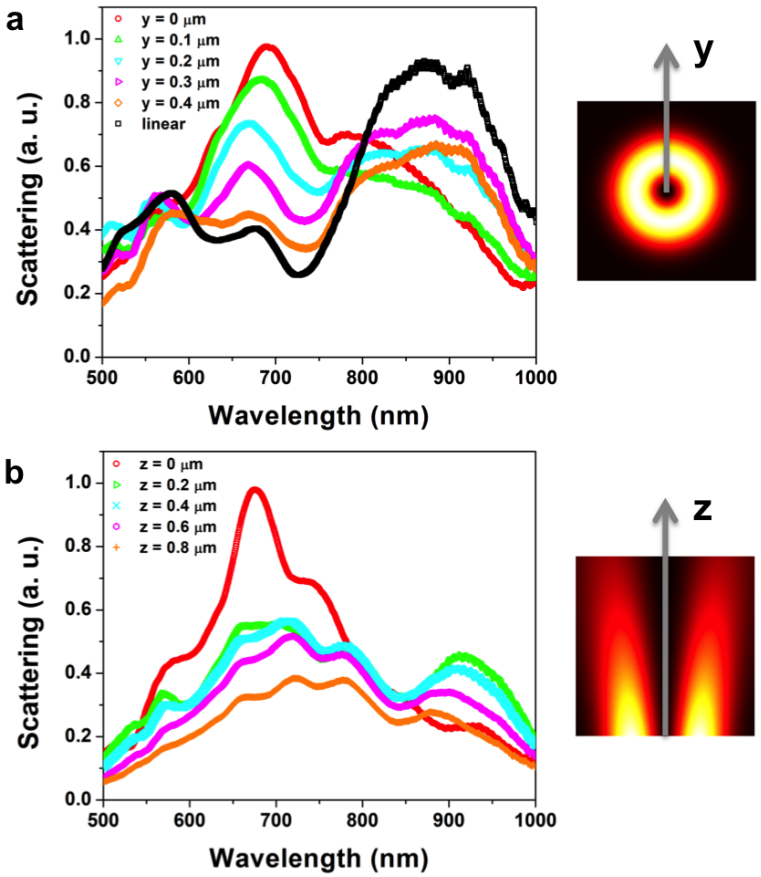

Figure 5.6: Nano-cluster spectra at different y- and z-positions with respect to the beam axis and focal plane. Scattering spectra (colors) for azimuthal polarization while moving the nano-cluster in the y- (a) and z- (b) directions. The black spectrum in (a) is the spectrum obtained for linearly polarized light for the same nano-cluster. The right panels schematically indicate the directions of the spatial shifts along the y- and z-directions superimposed on appropriate cross sections of E^2.

108, 111, 117, 127]. Here, we have demonstrated that optical vector beams can be used to selectively drive magnetic multipole excitations in metal-based nanostructures and that these excitations can be stronger than the electric multipolar modes of the identical structures. The magnetic modes can be understood as a collective excitation of electrodynamically coupled metal nanoparticles excited by a time varying azimuthally polarized electric field with instantaneous curl. The displacement currents produced in association with the azimuthal polarization induce a magnetic field analogous to that created by induction due to circulating

electric currents in electromagnets.

The magnetic modes excited by azimuthally polarized CVBs and with linearly polarized light are different in both the near- and far-fields. In the far-field the modes are in perpendicular orientations; with azimuthal CVBs the magnetic modes are always oriented along the beam propagation direction (*e.g.* z-axis polarized). More importantly, the mechanism by which each beam excites the magnetic modes is different. A z-oriented magnetic dipole mode is created by exciting an effective displacement current in the xy-plane due to the unique nature of the azimuthally polarized beam's polarization state and the coupled particle dipoles. A linearly x-polarized beam excites a y-oriented magnetic dipole mode by exciting an effective displacement current in the xy-plane. A current density in the z-direction is made possible by retardation of the beam along the z-axis, while a current density in the x-direction occurs due to the polarization of the beam. Combined, these effects yield an effective current in the xz-plane.

Conventional induction of magnetic (dipole) modes in nano-to-meso scale metamaterials relies upon the design of the structure. In contrast, our work shows that one can control the nature of the excitation with the optical field as well. Since we obtain the curl (or instantaneous angular momentum) from a focused azimuthal CVB, one should be able to drive a magnetic response in metal nanoparticle based materials that do not have morphology with cylindrical symmetry. In other words, a "beam engineering"[103] approach should allow inducing optical magnetism in "arbitrary" metal nanoparticle based structures that can the creation of displacement currents on the scale of the focused CVB (*e.g.* monolayer films of nanoparticles).

APPENDIX A

OPTICAL NONLINEARITIES AND ABLATION IN SILVER NANOWIRES

While the majority of the experiments presented in this dissertation focus on localized surface plasmon resonances in colloidal nanopartiles, Chapter 5 discusses the ability of silver nanoparticles in near-field proximity to support a resonance akin to a circulating current or a propagating surface plasmon. The plasmonic properties of silver nanowires (AgNWs) follow from extending the near-field limit of 1D lattices of AgNPs to the point of touching - multiple scattering peaks are observed dependent on the polarization of the incident beam[] and light coupled into the longitudinal resonances matching the long axis of the wire can be coupled into a propagating plasmon mode from one end of the wire to be radiated at the other end of the wire[128, 129]. Plasmonic nanowires in active research are often used as waveguides for their ability to confine light into subwavelength modes.

Previous work in the research group focused on the properties of the waveguide modes in AgNWs as precursors to a form of 'circuitry' to control the flow of light in nanostructures[130]. In the simplest case, pairs of crossed nanowires were studied as an nanoscale analogue to a Mach-Zehnder inteferometer. Separately exciting a propagating surface plasmon polariton in each of the wires at one end created emission at both of the distal ends of the wires with both intensity and phase modulations based on the lengths of the wires, the location of the crossing along the length of the wires, and the angle between them.

Further FDTD simulations of AgNWs examined how the frequency-dependent phase of an incident laser pulse affected the propagation of light through single nanowires. The calculated distributions of the electric fields in the AgNW were observed to have a standing wave-like pattern and the scattering spectra exhibited peak frequencies where the length L of the nanowire was approximately a half-integral multiple of the wavelength of the resonance

mode,

$$\lambda_{\mathrm{SP}}(\omega) = \frac{2L}{m},\ m = 1, 2, 3... \tag{A.1}$$

where $\lambda_{\mathrm{SP}}(\omega)$ is the dispersion relation of the AgNW[129]. In addition, the set of modes excited in the AgNW by a particular broad-band laser pulse was dependent on the frequency-dependent phase lag, or chirp of the pulse. Represented by a broad-band point-dipole source located near one end of the wire in the simulation domain with an additional time-dependent phase term, a pulse that began with a higher effective frequency that decreased over time (negative chirp) produced a set of propagating plasmon modes with greater confinement along the longitudinal axis of the wire than those beginning at a lower frequency that increased over the duration of the pulse (positive chirp). It was hypothesized that a phase-optimized pulse could produce a 'focusing' of the plasmon modes at the end of the wire distal to the excitation, increasing the efficiency of using the wire as a waveguide.

With this result in mind, an optical setup was designed to create a phase-controlled pulsed excitation source. The output of a home-built cavity-dumped Ti:Sapphire oscillator, pumped by a Spectra-Physics Millennia Xs laser set to 4.0 W power, operating at a repetition rate of 1.4 MHz and output power of 38 mW, was directed onto a diffraction grating such that the first-order diffraction was aligned into a collimating lens and a 1D rectangular spatial light modulator (SLM, CRi SLM-128). A schematic of the Ti:Sapphire laser is shown in Figure 2.2. The groove density of the grating was chosen such that the full bandwidth of the laser was spread across the pixel area of the SLM, allowing for the frequency-dependent phase lag of the pulse to be set by the independent voltage on each pixel of the SLM. The light is then focused by another lens identical to the first onto a second diffraction grating, slightly offset from the focal point of the second lens along the direction of the beam propagation in order to pre-compensate for the group velocity dispersion (GVD) of the beam introduced by the optics leading up to and inside the microscope. Another pair of lenses acted as a beam telescope to expand the beam to fill up the back focal plane of the microscope objective such

that the focal spot created by the objective was diffraction-limited in size. Next, the beam was focused onto a beta-barium borate (BBO) crystal to frequency-double the pulse and then re-collimated by another lens. A pair of mirrors in a periscope arrangement raised the beam height to and aligned the beam into the rear port of the microscope (Olympus IX-71). The beam was directed into the objective by a dichroic beamsplitter (Chroma T470lpxr) reflective at the wavelength of the frequency-doubled laser ($\lambda \approx 400 - 430$ nm) while allowing longer wavelengths to pass. The spectrum of the pulses before frequency doubling can be seen in Figure 2.3a, and their duration ($\sim$30 fs) can be measured from the second-harmonic generation autocorrelation shown in Figure 2.3b.

Samples of AgNWs were created by drop-casting 7.1 μL of a 10:1 diluted solution of NWs (Sigma-Alridch) onto a 1.5 mm glass coverslip (Fisher Scientific No. 1.5 12-541B) that was etched with a cross pattern by a tungsten-tipped scribing pen in order to locate regions of the sample for multiple experiments. The sample cell was closed according to the first procedure described in Section 2.5 and left to sit for 30 minutes with the etched coverslip on the bottom before inverting and mounting on the microscope sample holder.

The AgNW samples were illuminated for imaging by a dark-field condenser and the scattering was collected by the same objective used to focus the excitation beam onto the sample. The scattered light was directed onto a sCMOS array detector (Andor Neo) at the position of the microscope eyepiece. Each wire observed under pulsed light illumination was first imaged in white light dark-field with the pulsed source blocked. The pulsed source was then unblocked, and either a video was taken on the array detector or the collected light was coupled out the side port of the microscope into a collimator for a 50 μm multimode optical fiber leading to a spectrometer (Ocean Optics USB2000). Once the measurement of the wire under pulsed laser illumination was complete, the pulsed source is blocked again and a second dark-field image was taken.

When AgNWs with their long axis arranged along the direction of the polarization of the

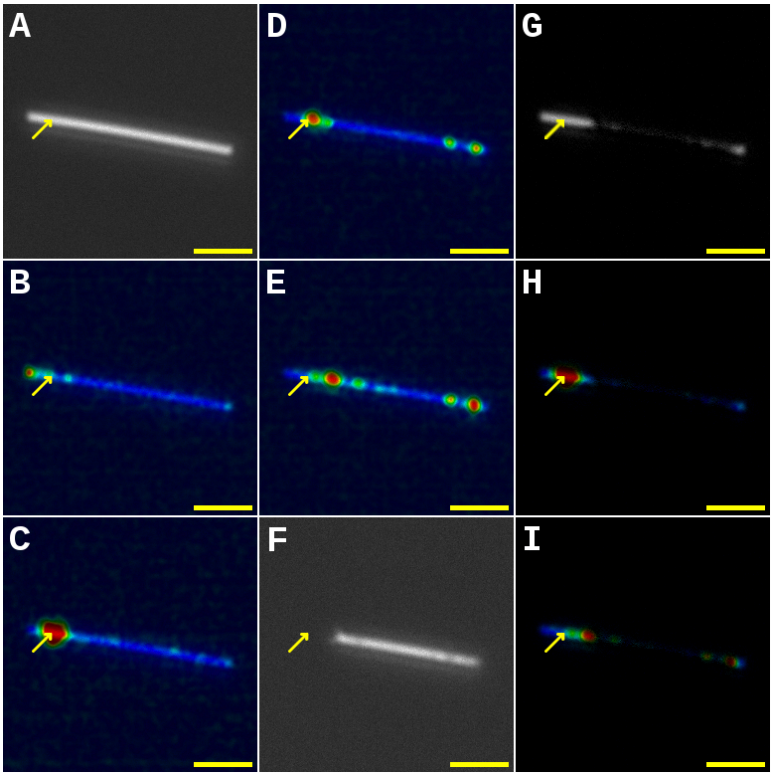

Figure A.1: Summary of a AgNW pulsed laser excitation experiment. (a) Dark-field scattering image of an ∼7 μm AgNW before excitation by the pulsed laser. The yellow arrow points to the location where the excitation beam was focused during the excitation measurement. The scale bar in this panel and all the following is 2 μm. (b)-(e) False-color overlay on top of the scattering image in (a) of frames from a video taken during excitation with the pulsed laser with the dark-field illumination off at (b) 0.63 s, (c) 1.78 s, (d) 4.62 s, and (e) 5.85 s. (f) Dark-field scattering image of the wire after the excitation. (g) Difference between the before and after images, $I = I_{\text{before}} - I_{\text{after}}$, highlighting the locations of material removed from the wire. (h) Overlay of the emission from panel (c) on top of the difference image. (i) Overlay of of the emission from panel (e) on top of the difference image.

pulsed light were illuminated with the excitation beam focused on one end of the wire, the dark-field scattering at a few points along the wire was observed to dim and often a piece of the wire would break off at one of these points and diffuse off into solution. Videos taken with the white light dark-field illumination turned off revealed that the AgNWs would emit light at locations along their length similar to dimming seen with the illumination left on. Figure A.1 shows the summary of a video taken for an ∼7 μm AgNW with the dark-field

illumination turned off. The locations where portions of the wire were removed and other spots dimmed due to the pulsed laser excitation are seen to correlate to the locations of emission events during the video.

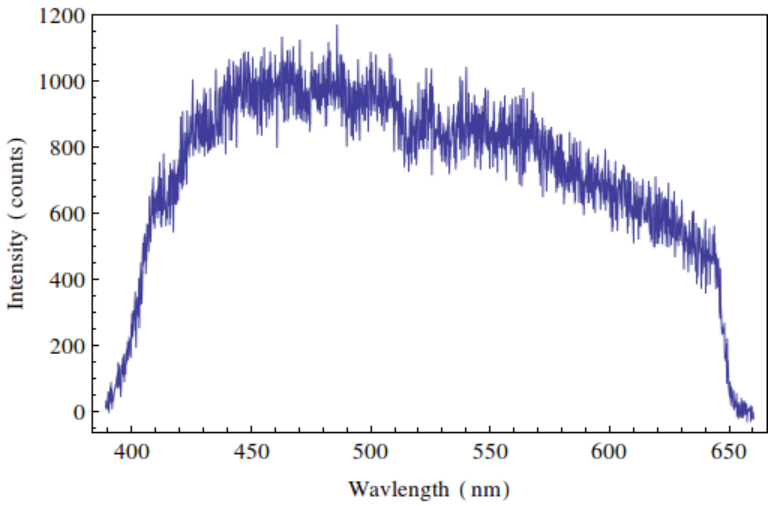

Figure A.2: Emission spectrum obtained from a AgNW during excitation by the pulsed laser source. The hard cut-offs at 410 nm and 650 nm are due to the filtering used in and frequency response of the detection system.

Furthermore, as the excitation beam is blocked from the array detector, the collected emission from the wires were the result of a nonlinear process. The spectral measurements of the emission reveal a broad-band white light continuum as seen in Figure A.2. Following the simulation results by Cao *et al.*[129], the locations of the nonlinear emission spots were believed to be a result of the electric field enhancement due to the excitation of standing-wave like plasmon resonances. However, attempts to fit the positions of the nonlinear emission along the length of the wire to a mode of the standing wave model eq. (A.1) failed as the positions were irregular and could only be fit by multiple high-order values of m not seen in the simulation results for similar lengths of AgNWs.

The next hypothesis to explain the observation of continuum generation was that defects in the AgNW structure created hotspots of electric field enhancement, and in order to test

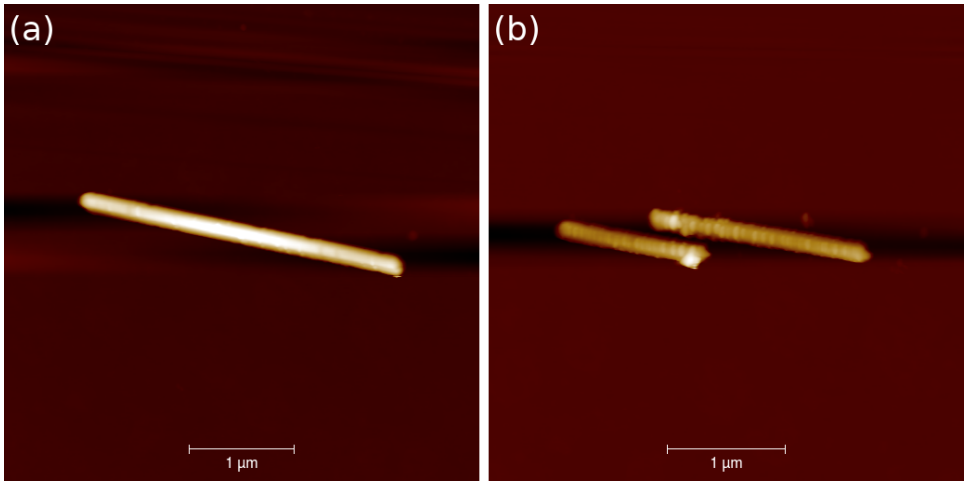

Figure A.3: (a) AFM image of a AgNW before excitation with the pulsed laser. The scale bar is 1 μm. (b) AFM image of the same AgNW after excitation with the pulsed laser.

this atomic force microscopy (AFM) images were taken both before and after pulsed laser excitation of the wires. Figure A.3 shows an example of the before and after AFM images for a single nanowire - no surface characteristics were observed in the before image that predicted the breaking of the nanowire near its center observed in the after image. In general, no major structural defects were observed that would explain the locations of the emission seen in the pulsed illumination experiments. A more satisfactory explanation was reported by Davies *et al.*[131] - chemical aging of the nanowire produces regions of silver oxide in the polymer layer protecting the AgNWs in solution, producing surface defects that can couple out the energy from a propagating surface plasmon excited by the incident beam.

APPENDIX B

DETECTING SCATTERING AND FLUORESCENCE PERPENDICULAR TO THE PRIMARY OPTICAL AXIS

The simulations in Chapter 3 show that the scattering of light from the collective plasmon resonance of a 1D AgNP lattice with interparticle spacings on the order of the wavelength of visible light has a strong directional dependence, with the strongest intensity being directed along the axis of the array. Furthermore, it was also shown that the emission from a quantum dot embedded in a lattice, such as those in Chapters 3 and 4, should have maximum interaction with the collective resonance when the transition dipole moment for the radiative relaxation is oriented perpendicular to the lattice, *i.e.* when the radiated field from the dipole is oriented along the axis of the lattice. Thus, the measured signal due to these interactions should be improved when the scattering and fluorescence from the lattice is collected in the plane of the sample, perpendicular to the primary optical axis of the microscope.

Methods such as light sheet microscopy [132] and creating mirrored nanostructures [133, 134, 135] were designed to enable a perpendicular detection geometry. However, neither is well-suited to the 1D lattice structures presented in this dissertation. Light sheet microscopy for samples deposited on a surface is limited to angles in the hemisphere above the plane of the sample, offering little to no improvement over a high numerical aperture objective lens used in dark-field microscopy measurements. The mirrored nanostructures overcome this limitation by reflecting light propagating along the surface of a sample cell toward the microscope objective, but the proximity necessary between the mirror and the lattice would interfere with the trapping beam used to order the lattices. Therefore two new methods were devised in order to collect the scattering and fluorescence from the 1D lattice structures measured in this dissertation perpendicular to the primary optical axis.

The first of the methods involved the fabrication of a new sample stage that raised

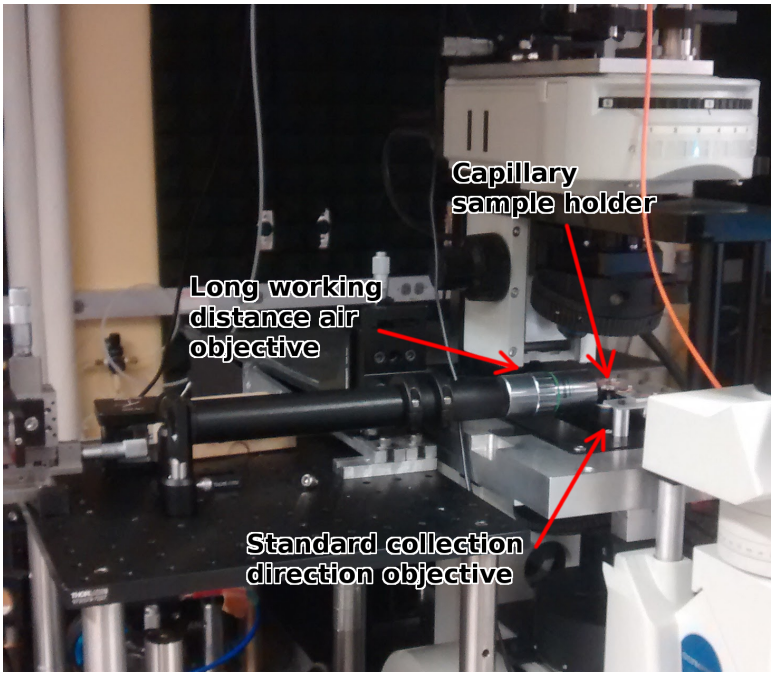

Figure B.1: Image of the optical setup used to measure scattering and fluorescence with a second objective lens perpendicular to the standard geometry.

the sample holder ∼2 cm above the surface of the microscope's piezo stage, visible on the right side of Figure B.1. The extra vertical offset allows for a second long working distance objective (Mitutoyo Plan Apo SL 20x) to be aligned in free space such that its focal plane overlaps the focal volume of the microscope's objective. The second objective was mounted by a thread adapter to a lens tube (Thorlabs) containing a lens (f=125 mm) that acted as a tube lens for the objective to form the magnified image at the far end of the tube. The threading at the far end of the tube could accept a USB camera (Thorlabs DCC1645C) for imaging or a mount for a 50 μm multimode optical fiber attached to an avalanche photodiode (Perkin-Elmer SPCM-AQR-15-FC) for TCSPC fluorescence measurements. As the sample cells described in Chapter 2 are designed only for detection from a single objective, the light from the sample would be scattered and attenuated too much by the spacer between the coverslips to be useful for this geometry. Therefore, samples were prepared in rectangular capillary tubes (VitroCom 8320-050) by drawing 2-3 μL of 200:1 diluted AgNP solutions into

the tube and letting dry for 6 hours under vacuum before re-filling with water. However, scattering from the water-glass and glass-air interfaces as well as from the corners of the capillary tube inhibited registration of the two imaging planes against each other and reduced the signal-to-noise ratio for TCSPC fluorescence measurements to the point where no decay rates could be resolved.

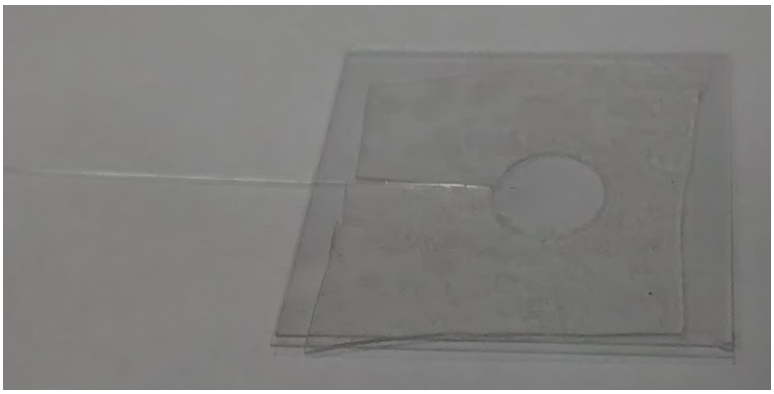

Figure B.2: Image of a sample cell with an embedded optical fiber containing 1D AgNP/quantum dot lattices.

The second method attempted was focused on collecting the fluorescence from a deposited 1D lattice with embedded quantum dot as described in Chapter 3. In order to increase the fluorescence signal from the perpendicular detection geometry, the same method for depositing the arrays of AgNPs around drop-cast quantum dots was used, with the exception of etching a cross-shaped marking in the coverslip with a tungsten scribing pen to make a reference point visible across multiple measurements. Once the structures were deposited, the sample cell was disassembled and the coverslip containing the structures was dried under vacuum to prevent oxidation. A length of fiber was cut from a spool of 105 μm core diameter multimode optical fiber (Thorlabs FG105LGA), an $\sim$0.5 cm section of the protective jacket was stripped from one end, and the other end was terminated with a FC connector to allow it to be attached to the avalanche photodiode. The bare end of the fiber was placed on the coverslip containing the fiber such that the deposited array structures were within the

collection angle of the fiber. A spacer was prepared with a slit in one side to accommodate the fiber, the spacer was placed on the coverslip around the fiber, and a bead of silicone rubber was added at the point the fiber and the spacer met on the interior of the sample chamber in order to ensure the water added to the chamber would not leak out. Sufficient water to fill the interior of the chamber was added to the sample cell and a second coverslip was placed over top to complete the cell. Figure B.2 shows a completed sample cell with the embedded optical fiber. Measurements in this configuration again proved unreliable due to low TCSPC signal compared to the noise level and the difficulty of ensuring alignment between the position of the 1D lattice structures and the end of the bare optical fiber.

REFERENCES

[1] M. Parker Givens. Optical properties of metals. In Frederick Seitz and David Turnbull, editors, *Solid State Physics*, chapter 6, pages 313–352. Academic Press Inc., New York, NY, 1958.

[2] David J. Griffiths. *Introduction to Electrodynamics*. Prentice Hall, Upper Saddle River, NJ, 1999.

[3] Lukas Novotny and Bert Hecht. *Principles of Nano-Optics*. Cambridge University Press, Cambridge, UK, 2006.

[4] Heinz Raether. *Surface Plasmons on Smooth and Rough Surfaces and on Gratings*. Springer-Verlag, New York, NY, 1988.

[5] Stefan A. Maier. *Plasmonics: Fundamentals and Applications*. Springer, New York, NY, 2007.

[6] J. Clerk Maxwell. VIII. A dynamical theory of the electromagnetic field. *Philosophical Transactions of the Royal Society of London*, 155:459–512, 1865.

[7] Craig F. Bohren and Donald R. Huffman. *Absorption and Scattering of Light by Small Particles*. Wiley-Interscience, New York, NY, 1983.

[8] Gustav Mie. Beiträge zur optik trüber medien, speziell kolloidaler metallösungen. *Annalen der Physik*, 25(3):377–445, 1908.

[9] Richard Gans. Über die form ultramikroskopischer goldteilchen. *Annalen der Physik*, 37(5):881–900, 1912.

[10] Andrew T. Young. Rayleigh scattering. *Applied Optics*, 20(4):533–535, 1981.

[11] Shengli Zou and George C. Schatz. Narrow plasmonic/photonic extinction and scattering line shapes for one and two dimensional silver nanoparticle arrays. *Journal of Chemical Physics*, 121(24):12606–12612, 2004.

[12] Erin M. Hicks, Shengli Zou, George C. Schatz, Kenneth G. Spears, and Richard P. Van Duyne. Controlling plasmon line shapes through diffractive coupling in linear arrays of cylindrical nanoparticles fabricated by electron beam lithography. *Nano Letters*, 5(6):1065–1070, 2005.

[13] Bernhard Lamprecht, Gerburg Schider, R. T. Lechner, Harald Ditlbacher, Joachim R. Krenn, and Alfred Leitner. Metal nanoparticle gratings: Influence of dipolar particle interaction on the plasmon resonance. *Physical Review Letters*, 84(10):4721–4724, 2000.

[14] Keith T. Carron, W. Fluhr, M. Meier, A. Wokaun, and H. W. Lehmann. Resonances of two-dimensional particle gratings in surface-enhanced raman scattering. *Journal of the Optical Society of America B*, 3(3):430–440, 1986.

[15] M. Meier, A. Wokaun, and Paul F. Liao. Enhanced fields on rough surfaces: dipolar interactions among particles of sizes exceeding the rayleigh limit. *Journal of the Optical Society of America B*, 2(6):931–949, 1985.

[16] Robert D. Cowan. *The Theory of Atomic Structure and Spectra*. University of California Press, Berkeley, CA, 1981.

[17] Tim H. Taminiau, Sinan Karaveli, Niek F. van Hulst, and Rashid Zia. Quantifying the magnetic nature of light emission. *Nature Communications*, 3:979, 2012.

[18] Dennis G. Hall. Vector-beam solutions of maxwell's wave equation. *Optics Letters*, 21(1):9–11, 1996.

[19] Qiwen Zhan. Cylindrical vector beams: from mathematical concepts to applications. *Advances in Optics and Photonics*, 1(1):1–57, 2009.

[20] Kimani C. Toussaint, Sungnam Park, Justing E. Jureller, and Norbert F. Scherer. Generation of optical vector beams with a diffractive optical element interferometer. *Optics Letters*, 30(21):2846–2848, 2005.

[21] V. Weisskopf and E. Wigner. Berechnung der natürlichen linienbreite auf grund der diraschen lichttheorie. *Zeitschirft für Physik*, 63(1-2):54–73, 1930.

[22] Matthew Pelton. Modified spontaneous emission in nanophotonic structures. *Nature Photonics*, 9:427–435, 2015.

[23] Jun John Sakurai. *Modern Quantum Mechanics, Revised Edition*. Addison-Wesley, San Francisco, CA, 1994.

[24] Edward M. Purcell, Henry C. Torrey, and Robert V. Pound. Resonance absorption by nuclear magnetic moments in a solid. *Physical Review*, 69(37), 1946.

[25] John D. Joannopoulos, Robert D. Meade, and Joshua N. Winn. *Photonic Crystals: Molding the Flow of Light*. Princeton University Press, Princeton, NJ, 1995.

[26] Peter Lodahl, A. Floris van Driel, Ivan S. Nikolaev, Arie Irman, Karin Overgaag, Daniel Vanmaekelbergh, and Willem L. Vos. Controlling the dynamics of spontaneous emission from quantum dots by photonic crystals. *Nature*, 430:654–657, 2004.

[27] Susumu Noda, Masayuki Fujita, and Takashi Asano. Spontaneous-emission control by photonic crystals and nanocavities. *Nature Photonics*, 1:449–458, 2007.

[28] Eli Yablonovitch. Inhibited spontaneous emission in solid-state physics and electronics. *Physical Review Letters*, 58(50):2059–2062, 1987.

[29] J. M. Gérard, B. Sermage, B. Gayral, B. Legrand, E. Costard, and V. Thierry-Mieg. Enhanced spontaneous emission by quantum boxes in a monolithic optical microcavity. *Physical Review Letters*, 5(1998):1110–1113, 81.

[30] Thang B. Hoang, Gleb M. Akselrod, Christos Argyropoulos, Jiani Huang, David R. Smith, and Maiken H. Mikkelsen. Ultrafast spontaneous emission source using plasmonic nanoantennas. *Nature Communications*, 6:7788, 2015.

[31] Raman A. Shah, Norbert F. Scherer, Matthew Pelton, and Stephen K. Gray. Ultrafast reversal of a fano resonance in a plasmon-exciton system. *Physical Review B*, 88(7):075411, 2013.

[32] Stefan A. Maier, Pieter G. Kik, and Harry A. Atwater. Observation of coupled plasmon-polariton modes in au nanoparticle chain waveguides of different lengths: estimation of waveguide loss. *Applied Physics Letters*, 81(9):1714–1716, 2002.

[33] Encai Hao and George C. Schatz. Electromagnetic fields around silver nanoparticles and dimers. *Journal of Chemical Physics*, 120:357–366, 2004.

[34] Arthur Ashkin. Acceleration and trapping of particles by radiation pressure. *Physical Review Letters*, 24(4):156–159, 1970.

[35] David G. Grier. Nature. *A revoultion in optical manipulations*, 424:810–816, 2003.

[36] Karel Svoboda and Steven M. Block. Optical trapping of metallic rayleigh particles. *Optics Letters*, 19(13):930–932, 1994.

[37] Anni Lehmuskero, Peter Johansson, Halina Rubinsztein-Dunlop, Lianming Tong, and Mikael äll. Laser trapping of colloidal metal nanoparticles. *ACS Nano*, 9(4):3453–3469, 2015.

[38] Michael M. Burns, Jean-Marc Fournier, and Jene A. Golovchenko. Optical binding. *Physical Review Letters*, 63(12):1233–1236, 1989.

[39] Michael M. Burns, Jean-Marc Fournier, and Jene A. Golovchenko. Optical matter: crystallization and binding in intense optical fields. *Science*, 249(4970):749–754, 1990.

[40] Zijie Yan, Uttam Manna, Wei Qin, Art Camire, Philippe Guyot-Sionnest, and Norbert F. Scherer. Hierarchical photonic synthesis of hybrid nanoparticle assemblies. *Journal of Physical Chemistry Letters*, 4(16):2630–2636, 2013.

[41] Mason J. Guffey, Ryan L. Miller, Stephen K. Gray, and Norbert F. Scherer. Plasmon-driven selective deposition of au bipyramidal nanoparticles. *Nano Letters*, 11(10):4058–4066, 2011.

[42] Ying Bao, Zijie Yan, and Norbert F. Scherer. Optical printing of electrodynamically coupled metallic nanoparticle arrays. *Journal of Physical Chemistry C*, 118(33):19315–19321, 2014.

[43] D. E. Spence, P. N. Kean, and W. Sibbett. 60-fsec pulse generation from a self-mode-locked ti:sapphire laser. *Optics Letters*, 16(1):42–44, 1991.

[44] Yish-Hann Liau, Andreas N. Unterreiner, David C. Arnett, and Norbert F. Scherer. Femtosecond-pulse cavity-dumped solid-state oscillator design and application to ultrafast microscopy. *Applied Optics*, 38(36):7386–7392, 1999.

[45] I. F. Sbalzarini and P. Koumoutsakos. Feature point tracking and trajectory analysis for video imaging in cell biology. *Journal of Structural Biology*, 151:182–195, 2005.

[46] M. Stalder and M. Schadt. Linearly polarized light with axial symmetry generated by liquid-crystal polarization converters. *Optics Letters*, 21(23):1948–1950, 1996.

[47] Margaret A. Hines and Philippe Guyot-Sionnest. Synthesis and characterization of strongly luminescing zns-capped cdse nanocrystals. *Journal of Physical Chemistry*, 100(2):468–471, 1996.

[48] Ardavan F. Oskooi, David Roundy, Mihai Ibanescu, Peter Bermel, John D. Joannopoulos, and Steven G. Johnson. Meep: A flexible free-software package for electromagnetic simulations by the fdtd method. *Computer Physics Communications*, 181(3):687–702, 2010.

[49] Peter B. Johnson and R. W. Christy. Optical constants of the noble metals. *Physical Review B*, 6(12):4370, 1972.

[50] Yu lin Xu. Electromagnetic scattering by an aggregate of spheres. *Applied Optics*, 34(21):4573–4588, 1995.

[51] Jack Ng, Z. F. Lin, C. T. Chan, and Ping Sheng. Photonic clusters formed by dielectric microspheres: Numerical simulations. *Physical Review B*, 72(8):085130, 2005.

[52] Allen Taflove, Ardavan Oskooi, and Steven G. Johnson. *Advances in FDTD computational electrodynamics: photonics and nanotechnology.* Artech house, Norwood, MA, 2013.

[53] Jon A. Schuller, Edward S. Barnard, Wenshan Cai, Young Chul Jun, Justin S. White, and Mark L. Brongersma. Plasmonics for extreme light concentration and manipulation. *Nature Materials*, 9:193–204, 2010.

[54] Andrew N. Shipway, Eugenii Katz, and Itamar Willner. Nanoparticle arrays on surfaces for electronic, optical, and sensor applications. *ChemPhysChem*, 1(1):18–52, 2000.

[55] Ekmel Ozbay. Plasmonics: Merging photonics and electronics at nanoscale dimensions. *Science*, 311(5758):189–193, 2006.

[56] Jeffrey N. Anker, W. Paige Hall, Olga Lyandres, Nilam C. Shah, Jing Zhao, and Richard P. Van Duyne. Biosensing with plasmonic nanosensors. *Nature Materials*, 7:442–453, 2008.

[57] Amanda J. Haes, Shengli Zou, Jing Zhao, George C. Schatz, and Richard P. Van Duyne. Localized surface plasmon resonance spectroscopy near molecular resonances. *Journal of the American Chemical Society*, 128(33):10905–10914, 2006.

[58] Surbhi Lal, Susan E. Clare, and Naomi J. Halas. Nanoshell-enabled photothermal cancer therapy: Impending clinical impact. *Accounts of Chemical Research*, 41(12):1842–1851, 2008.

[59] Mustafa S. Yavuz, Yiyun Cheng, Jingyi Chen, Clair M. Cobley, Qiang Zhang, Matthew Rycenga, Jinwei Xie, Chulhong Kim, Kwang H. Song, Andrea G. Schwartz, Lihong V. Wang, and Younan Xia. Gold nanocages covered by smart polymers for controlled release with near-infrared light. *Nature Materials*, 8:935–939, 2009.

[60] Stefan A. Maier, Pieter G. Kik, Harry A. Atwater, Sheffer Meltzer, Elad Harel, Bruce E. Koel, and Ari A. G. Requicha. Local detection of electromagnetic energy transport below the diffraction limit in metal nanoparticle plasmon waveguides. *Nature Materials*, 2:229–232, 2003.

[61] Liane S. Slaughter, Lin-Yung Wang, Britain A. Willingham, Jana M. Olson, Pattanawit Swanglap, Sergio Dominguez-Medina, and Stephan Link. Plasmonic polymers unraveled through single particle spectroscopy. *Nanoscale*, 6(19):11451–11461, 2014.

[62] Hazel Kitching, Matthew J. Shiers, Anthony J. Kenyon, and Ivan P. Parkin. Self-assembly of metallic nanoparticles into one dimensional arrays. *Journal of Materials Chemistry A*, 1(24):6985–6999, 2013.

[63] C. P. Collier, T. Vossmeyer, and J. R. Heath. Nanocrystal superlattices. *Annual Review of Physical Chemistry*, 49:371–404, 1998.

[64] M. P. Pileni. Nanocrystal self-assemblies: Fabrication and collective properties. *Journal of Physical Chemistry B*, 105(17):3358–3371, 2001.

[65] T. ár, L. C. Dávila, Kishan Dholakia, and D. L. Andrews. Multiple optical trapping and binding: New routes to self-assembly. *Journal of Physics B: Atomic, Molecular and Optical Physics*, 43(10):102001, 2010.

[66] David G. Grier. A revolution in optical manipulation. *Nature*, 424:810–816, 2003.

[67] Miles Padgett and Richard Bowman. Tweezers with a twist. *Nature Photonics*, 5:343–348, 2011.

[68] Allen H. Yang, Sean D. Moore, Bradley S. Schmidt, Matthew Klug, Michal Lipson, and David Erickson. Optical manipulation of nanoparticles and biomolecules in sub-wavelength slot waveguides. *Nature*, 457:71–75, 2009.

[69] Mason J. Guffey, Ryan L. Miller, Stephen K. Gray, and Norbert F. Scherer. Plasmon-driven selective deposition of au bipyramidal nanoparticles. *Nano Letters*, 11(10):4058–4066, 2011.

[70] Mathieu L. Juan, Maurizio Righini, and Romain Quidant. Plasmon nano-optical tweezers. *Nature Photonics*, 5:349–356, 2011.

[71] Michael M. Burns, Jean-Marc Fournier, and Jene A. Golovchenko. Optical binding. *Physical Review Letters*, 63(12):1233–1236, 1989.

[72] Kishan Dholakia and Pavel Zemánek. Colloquium: Gripped by light: Optical binding. *Reviews of Modern Physics*, 82(2):1767–1791, 2010.

[73] Zijie Yan, Raman A. Shah, Garrett Chado, Stephen K. Gray, Matthew Pelton, and Norbert F. Scherer. Guiding spatial arrangements of silver nanoparticles by optical binding interactions in shaped light fields. *ACS Nano*, 7(2):1790–1802, 2013.

[74] Vassili Demergis and Ernst-Ludwig Florin. Ultrastrong optical binding of metallic nanoparticles. *Nano Letters*, 12(11):5756–5760, 2012.

[75] Zijie Yan, Ying Bao, Uttam Manna, Raman A. Shah, and Norbert F. Scherer. Enhancing nanoparticle electrodynamics with gold nanoplate mirrors. *Nano Letters*, 14(5):2436–2442, 2014.

[76] Ying Bao, Zijie Yan, and Norbert F. Scherer. Optical printing of electrodynamically coupled metallic nanoparticle arrays. *Journal of Physical Chemistry C*, 118(33):19315–19321, 2014.

[77] Andreas Hohenau, Alfred Leitner, and Franz R. Aussenegg. Near-field and far-field properties of nanoparticle arrays. *Springer Series in Optical Sciences*, 131:11–25, 2007.

[78] Oliver Benson. Assembly of hybrid photonic architectures from nanophotonic constituents. *Nature*, 480:193–199, 2011.

[79] Olga Kulakovich, Natalya Strekal, Alexandr Yaroshevich, Sergey Maskevich, Sergey Gaponenko, Igor Nabiev, Ulrike Woggon, and Mikhail Artemyev. Enhanced luminescence of cdse quantum dots on gold colloids. *Nano Letters*, 2(12):1449–1452, 2002.

[80] Jian Zhang, Yi Fu, Mustafa H. Chowdhury, and Joseph R. Lakowicz. Plasmon-coupled fluorescence probes: effect of emission wavelength on fluorophore-labeled silver partices. *Journal of Physical Chemistry C*, 112(25):9172–9180, 2008.

[81] Keiko Munechika, Yeechi Chen, Andreas F. Tillack, Abhishek P. Kulkarni, Ilan Jen-La Plante, Andrea M. Munro, and David S. Ginger. Spectral control of plasmonic emission enhancement from quantum dots near single silver nanoprisms. *Nano Letters*, 10(7):2598–2603, 2010.

[82] Mason J. Guffey and Norbert F. Scherer. All-optical patterning of au nanoparticles on surfaces using optical traps. *Nano Letters*, 10(11):4302–4308, 2010.

[83] Hiroharu Tamaru, Hitoshi Kuwata, Hideki T. Miyazaki, and Kenjiro Miyano. Resonant light scattering from individual ag nanoparticles and particle pairs. *Applied Physics Letters*, 80(10):1826–1828, 2002.

[84] Juris Prikulis, Fredrik Svedberg, and Mikael Käll. Optical spectroscopy of single trapped metal nanoparticles in solution. *Nano Letters*, 4(1):115–118, 2004.

[85] Alexander Ohlinger, Spas Nedev, Andrey A. Lutich, and Jochen Feldmann. Optothermal escape of plasmonically coupled silver nanoparticles from a three-dimensional optical trap. *Nano Letters*, 11(4):1770–1774, 2011.

[86] M. Quinten, Alfred Leitner, Joachim R Krenn, and Franz R. Aussenegg. Electromagnetic energy transport via linear chains of silver nanoparticles. *Optics Letters*, 23(17):1331–1333, 1998.

[87] Stefan A. Maier, Mark L. Brongersma, Pieter G. Kik, and Harry A. Atwater. Observation of near-field coupling in metal nanoparticle chains using far-field polarization spectroscopy. *Physical Review B*, 65(19):193408–4, 2002.

[88] Anatoliy O. Pinchuk and George C. Schatz. Nanoparticle optical properties: Far- and near-field electrodynamic coupling in a chain of silver spherical nanoparticles. *Materials Science and Engineering B*, 149(3):251–258, 2008.

[89] Sebastian van der Linden, J. Kuhl, and H. Giessen. Controlling the interaction between light and gold nanoparticles: Selective suppression of extinction. *Physical Review Letters*, 86:4688, 2001.

[90] Christian Dahmen, Benjamin Schmidt, and Gero von Plessen. Radiation damping in metal nanoparticle pairs. *Nano Letters*, 7(2):318–322, 2007.

[91] Xiaogang Peng, Liberato Manna, Weidong Yang, Juanita Wickham, Erik Scher, Andreas Kadavanich, and A. Paul Alivisatos. Shape control of cdse nanocrystals. *Nature*, 404:59–61, 2000.

[92] Patrick Figliozzi, Nishant Sule, Zijie Yan, Ying Bao, Stanislav Burov, Stephen K. Gray, Stuart A. Rice, Suriyanarayanan Vaikuntanathan, and Norbert F. Scherer. Driven optical matter: electrodynamically coupled nanoparticles in an optical ring vortex. *Physical Review E*, 95(2):022604, 2017.

[93] Dirk Englund, Andrei Faraon, Ilya Fushman, Nick Stoltz, Pierre Petroff, and Jelena Vuć. Controlling cavity reflectivity with a single quantum dot. *Nature*, 450:857–861, 2007.

[94] Haixu Leng, Brian Szychowski, Marie-Christine Daniel, and Matthew Pelton. Strong coupling and induced transparency at room temperature with single quantum dots and gap plasmons. *Nature Communications*, 9:4012, 2018.

[95] Piernicola Spinicelli, Stephanie Buil, Xavier Quelin, Benoit Mahler, B. Dubertret, and J-P Hemier. Bright and grey states in cdse-cds nanocrystals exhibiting strongly reduced blinking. *Physical Review Letters*, 102(13):136801, 2009.

[96] Gerard Gouesbet and Gerard Gréhan. Generalized lorenz-mie theory for assemblies of spheres and aggregates. *Journal of Optics A Pure and Applied Optics*, 1(6):706–712, 1999.

[97] Eyal Cohen-Hoshen, Garnett W. Bryant, Iddo Pinkas, Joseph Sperling, and Israel Bar-Joseph. Exciton-plasmon interactions in quantum dot-gold nanoparticle structures. *Nano Letters*, 12(8):4260–4264, 2012.

[98] F. Bloch, W. W. Hansen, and Martin Packard. Nuclear induction. *Physical Review*, 69(3):127, 1946.

[99] Charles P. Slichter. *Principles of Magnetic Resonance*. Springer, Berlin, 1990.

[100] Evgenii K. Zavoisky. Paramagnetic relaxation of liquid solutions for perpendicular fields. *Journal of Physics USSR*, 9(3):211–216, 1945.

[101] Mark Kasperczyk, Steven Person, Duarte Ananias, Luis D. Carlos, and Lukas Novotny. Excitation of magnetic dipole transitions at optical frequencies. *Physical Review Letters*, 114(16):163903, 2015.

[102] Andrey E. Miroshnichenko, Wei Liu, Dragomir Neshev, Yuri S. Kivshar, Arseniy I. Kuznetsov, Yuan Hsing Fu, and Boris Luk'yanchuk. Magnetic light: optical magnetism of dielectric nanoparticles. *Optics and Photonics News*, 23(12):35, 2012.

[103] Tanya Das, Prasad P. Iyer, Ryan A. DeCrescent, and Jon A. Schuller. Beam engineering for selective and enhanced coupling to multipolar resonances. *Physical Review B*, 92(24):241110, 2015.

[104] Tanya Das and Jon A. Schuller. Dark modes and field enhancements in dielectric dimers illuminated by cylindricla vector beams. *Physical Review B*, 95(20):201111, 2017.

[105] J. B. Pendry, A. J. Holden, D. J. Robbins, and W. J. Stuart. Magnetism from conductors and enhanced nonlinear phenomena. *IEEE Transactions on Microwave Theory and Techniques*, 47(11):2075–2084, 1999.

[106] R. A. Shelby, D. R. Smith, and S. Schultz. Experimental verification of a negative index of refraction. *Science*, 292(5514):77–79, 2001.

[107] Viktor G. Veselago. The electrodynamics of substances with simultaneously negative values of ε and μ. *Soviet Physics USPEKHI-USSR*, 10:509–514, 1968.

[108] A. Alù, A. Salandrino, and Nader Engheta. Negative effective permeability and left-handed materials at optical frequencies. *Optics Express*, 14(4):1557–1567, 2006.

[109] M. Fruhnert, S. Mülig, F. Lederer, and C. Rockstuhl. Towards negative index self-assembled metamaterials. *Physical Review B*, 89(7):075408, 2014.

[110] Jingjing Li and Nader Engheta. Subwavelength plasmonic cavity resonator on a nanowire wirth periodic permittivity variation. *Physical Review B*, 74(11):115125, 2006.

[111] C. R. Simovski and S. A. Tretyakov. Model of isotropic resonant magnetism in the visible range based on core-shell clusters. *Physical Review B*, 79(4):045111, 2009.

[112] R. Jiang, B. Li, C. Fang, and J. Wang. Metal/semiconductor hybrid nanostructures for plasmon-enhanced applications. *Advanced Materials*, 26(31):5274–5309, 2014.

[113] Wei Liu, Andrey E. Miroshnichenko, Dragomir N. Neshev, and Yuri S. Kivshar. Broadband unidirectional scattering by magneto-electric core-shell nanoparticles. *ACS Nano*, 6(6):5489–5497, 2012.

[114] Huanjun Chen, Lei Chao, Yat Cho Man, Chunmei Zhao, Jianfang Wang, and Baocheng Yang. Fano resonance in (gold core)-(dielectric shell) nanostructures without symmetry breaking. *Small*, 8(10):1503–1509, 2012.

[115] Boyi Gong, Xiaopeng Zhao, Zhenzhen Pan, Sa Li, Xiaonong Wang, Yan Zhao, and Chunrong Luo. A visible metamaterial fabricated by self-assembly method. *Scientific Reports*, 4:4713, 2014.

[116] Zhaoxia Qian, Simon P. Hastings, Chen Li, Brian Edward, Christine K. McGinn, Nader Engheta, Zahra Fakhraai, and So-Jung Park. Raspberry-like metamolecules exhibiting strong magnetic resonances. *ACS Nano*, 9(2):1263–1270, 2015.

[117] Sassan N. Sheikholeslami, Hadiseh Alaeian, Ai Leen Koh, and Jennifer A. Dionne. A metafluid exhibiting strong optical magnetism. *Nano Letters*, 13(9):4137–4141, 2013.

[118] Pamela L. Greene and Dennis G. Hall. Properties and diffraction of vector bessel-gauss beams. *Journal of the Optical Society of America A*, 13(5):962–966, 1996.

[119] Kathleen S. Youngworth and Thomas G. Brown. Inhomogenous polarization in scanning optical microscopy. *Proceedings of SPIE*, 3919:75–81, 2000.

[120] R. Dorn, S. Quabis, and G. Leuchs. Sharper focus for a radially polarized light beam. *Physical Review Letters*, 91(23):233901, 2003.

[121] Kathleen S. Youngworth and Thomas G. Brown. Focusing of high numerical aperture cylindrical-vector beams. *Optics Express*, 7(2):77–87, 2000.

[122] Neus G. Bastús, Florind Merko, Jordi Piella, and Victor Puntes. Synthesis of highly monodisperse citrate-stabilized silver nanoparticles of up to 200 nm: kinetic control and catalytic properties. *Chemistry of Materials*, 26(9):2836–2846, 2014.

[123] J. Christopher Love, Lara A. Estroff, Jennah K. Kriebel, Ralph G. Nuzzo, and George M. Whitesides. Self-assembled monolayers of thiolates on metals as a form of nanotechnology. *Chemical Reviews*, 105(4):1103–1170, 2005.

[124] Allen Taflove and Susan C. Hagness. *Computational Electrodynamics: The Finite-Difference Time-Domain Method*. Artech House, 2004.

[125] Lars O. Herrmann, Ventsislav K. Valev, Christos Tserkezis, Jonathan S. Barnard, Setu Kasera, Oren A. Scherman, Javier Aizpurua, and Jeremy J. Baumberg. Threading plasmonic nanoparticle strings with light. *Nature Communications*, 5(6):4568, 2014.

[126] Isabel Romero, Javier Aizpurua, Garnett W. Bryant, and F. Javier Garía de Abajo. Plasmons in nearly touching metallic nanoparticles: singular response in the limit of touching dimers. *Optics Express*, 14(21):9988–9999, 2006.

[127] M. Burresi, D. van Oosten, T. Kampfrath, H. Schoenmaker, R. Heideman, A. Leinse, and L. Kuipers. Probing the magnetic field of light at optical frequencies. *Science*, 326(5952):550–553, 2009.

[128] Harald Ditlbacher, Andreas Hohenau, Dieter Wagner, Uwe Kreibig, Michael Rogers, Ferdinand Hofer, Franz R. Aussenegg, and Joachim R. Krenn. Silver nanowires as surface plasmon resonators. *Physical Review Letters*, 95(25):257403, 2005.

[129] Lina Cao, Rene A. Nome, Jason M. Montgomery, Stephan K. Gray, and Norbert F. Scherer. Controlling plasmonic wave packets in silver nanowires. *Nano Letters*, 10:3389–3394, 2010.

[130] Thomas G. Spears. *Thermal and Spatial Control of Surface Plasmons*. PhD thesis, Chicago, IL, 2012.

[131] Melari Davies, Angela Wochnik, Florian Feil, Christophe Jung, Cristoph Brächle, Christina Scheu, and Jens Michaelis. Synchronous emission from nanometric silver particles through plasmonic coupling on silver nanowires. *ACS Nano*, 6(7):6049–6057, 2012.

[132] Omar E. Olarte, Jordi Andilla, Emilio J. Gualda, and Pablo Loza-Alvarez. Light-sheet microscopy: a tutorial. *Advances in Optics and Photonics*, 10(1):111–179, 2018.

[133] K. T. Seale, R. S. Reiserer, D. A. Markov, I. A. Ges, C. Wright, C. Janetopoulos, and J. P. Wikswo. Mirrored pyramidal wells for simultaneous multiple vantage point microscopy. 232(1), 2008.

[134] Remi Galland, Gianluca Grenci, Ajay Aravind, Virgile Viasnoff, Vincent Studer, and Jean-Baptiste Sibarita. 3d high- and super-resolution imaging using single-objective spim. *Nature Methods*, 12:641–644, 2015.

[135] Pierre Mangeol and Erwin J. G. Peterman. High-resolution real-time dual-view imaging with multiple point of view microscopy. *Biomedical Optics Express*, 7(9):3631, 2016.